

GPO PRICE \$ _____

CFSTI PRICE(S) \$ _____

Hard copy (HC) 3.00

Microfiche (MF) .65

ff 653 July 65

Research Laboratories for the Engineering Sciences

University of Virginia

Charlottesville

Report No. AST-4038-103-67U

June 1967

N67-31331
(ACCESSION NUMBER)

125
(PAGES)

CR-8582X
(NASA CR OR TMX OR AD NUMBER)

(THRU)

1
(CODE)

14
(CATEGORY)

FACILITY FORM NO. 1

DESIGN AND PERFORMANCE OF AN
AERODYNAMIC MOLECULAR BEAM
AND BEAM DETECTION SYSTEM

By

O. F. Hagen
J. E. Scott, Jr.
A. K. Varma

Technical Report

National Aeronautics and Space Administration

Grant No. NGR 47-005-046

Division of Aeronautical Engineering and Engineering Physics
RESEARCH LABORATORIES FOR THE ENGINEERING SCIENCES
SCHOOL OF ENGINEERING AND APPLIED SCIENCE
UNIVERSITY OF VIRGINIA
CHARLOTTESVILLE, VIRGINIA

Report No. AST-4038-103-67U

June 1967

Copy No. 4

FOREWARD

This report reflects the continuing research in molecular beams and molecular collision phenomena being carried out in the Department of Aerospace Engineering and Engineering Physics at the University of Virginia. This investigation has been supported by the National Aeronautics and Space Administration under NASA Grant NGR 47-005-046. The apparatus was constructed by funds made available to the University through its NASA Multidisciplinary Research Grant NsG-682.

The scope of this report has been restricted to that portion of the research involving characterization of the high intensity molecular beam (and associated molecular collision phenomena) which is used for the detailed gas-surface interaction studies being carried out under this research program. These interaction studies will be discussed in subsequent reports.

ABSTRACT

The performance of an aerodynamic molecular beam system is presented. Design criteria for the various components of the system and for a time-of-flight detection system are discussed, and the performance of the detector and the beam modulation system is compared with theoretical predictions. The experimental results confirm the phenomenon of freezing of translational temperature in freely expanding jets, demonstrate the limitation of speed ratio and intensity of nozzle beams due to partial condensation of the beam gas, and describe the effect of skimmer interaction on the profile of the molecular beam. The high sensitivity of the detector enabled off-axis measurements of the beam speed distribution with good angular resolution in regions where the intensity was less than 1% of the centerline intensity. The speed ratio is found to be constant over a larger part of the beam profile than is the beam particle density. The speed ratio decreases to nearly half its centerline value in the outer sections of the beam.

ACKNOWLEDGMENTS

This report is based in large part on a thesis submitted by A. K. Varma for the Master's degree in aerospace engineering at the University of Virginia. Helpful criticism in the course of the research was provided by Mr. J. A. Phipps. Editorial assistance was given by Professor S. S. Fisher. Special acknowledgment is due to Mrs. Elizabeth Kirby for her careful preparation of the manuscript.

TABLE OF CONTENTS

	<u>Page</u>
ABSTRACT	iii
ACKNOWLEDGEMENTS	iv
LIST OF FIGURES	vii
LIST OF TABLES.	ix
LIST OF SYMBOLS.	x
SECTION I INTRODUCTION	1
1.1 GENERAL BACKGROUND	1
1.2 THE RESEARCH PROGRAM	2
SECTION II GENERAL DESCRIPTION OF THE VACUUM SYSTEM	3
2.1 INTRODUCTION	3
2.2 DESIGN OF THE BEAM DEFINING ELEMENTS	3
Nozzle	3
Skimmer.	7
Collimator	12
2.3 DESCRIPTION OF THE VACUUM CHAMBERS	13
The Nozzle Discharge Chamber C_1	13
Gas Supply System	13
Collimation Chamber C_2	14
Detection Chamber C_3	15
2.4 CONTROL CIRCUITS AND SAFETY FEATURES OF THE SYSTEM	17
2.5 VACUUM SYSTEM PERFORMANCE	19
SECTION III MOLECULAR BEAM DETECTION SYSTEM.	21
3.1 INTRODUCTION.	21
3.2 DESIGN OF THE TIME-OF-FLIGHT DETECTOR	22
The Molecular Beam	22
The Ionizing Electron Beam	23
Ion Detection and Collection System	25
3.3 DESCRIPTION OF THE TIME-OF-FLIGHT DETECTOR	25
3.4 PERFORMANCE OF THE TIME-OF-FLIGHT DETECTOR	30
Electron Beam	31
The Ion Current.	31

	<u>Page</u>
3.5 SIGNAL ANALYSIS	36
3.6 DETERMINATION OF THE VELOCITY DISTRIBUTIONS BY THE TIME-OF-FLIGHT METHOD	38
3.7 EFFECTS OF FINITE SHUTTER FUNCTION	40
SECTION IV DESIGN AND DESCRIPTION OF THE BEAM MODULATING SYSTEM	42
4.1 SHUTTER FUNCTION	42
4.2 DESIGN OF A TIME-OF-FLIGHT EXPERIMENT	43
Molecular Beam	43
Chopper Disc	45
Chopper - Detector Distance L	46
4.3 DESCRIPTION OF THE SYSTEM	49
4.4 SYSTEM PERFORMANCE	50
SECTION V EXPERIMENTAL RESULTS	56
5.1 GEOMETRY OF THE BEAM SYSTEM	56
5.2 TOTAL PARTICLE DENSITY MEASUREMENTS	58
Beam Profile Measurements	67
5.3 SPEED DISTRIBUTION MEASUREMENTS	73
Influence of Source Pressure	73
Variation of Speed Ratio with Nozzle-Skimmer Separation Distance	73
Off-Axis Speed Distribution Measurements	78
5.4 ASYMMETRY OF THE BEAM (DENSITY) PROFILE	84
SECTION VI CONCLUSIONS	86
BIBLIOGRAPHY	88
APPENDIX A DESIGN OF THE BEAM DEFINING ELEMENTS	92
APPENDIX B DESIGN CALCULATIONS FOR THE TIME-OF-FLIGHT DETECTOR	98
APPENDIX C THEORETICAL CONSIDERATIONS REGARDING A PULSED NOZZLE BEAM: EFFECT OF FINITE SHUTTER FUNCTION	101
APPENDIX D DESIGN CALCULATIONS FOR THE BEAM MODULATION SYSTEM	107
APPENDIX E RECOMMENDED OPERATING PROCEDURES	111

LIST OF FIGURES

	<u>Page</u>
FIG. 2. 1. 1. Molecular Beam System	4
FIG. 2. 1. 2 Molecular Beam Apparatus Vacuum System	5
FIG. 2. 2. 1 Nozzle Assembly	8
FIG. 2. 2. 2 Nozzle Discharge Chamber C_1 and Collimation Chamber C_2	9
FIG. 2. 2. 3 Details of Skimmer and Collimator	11
FIG. 2. 4. 1 Schematic Diagram of Pump Control Panel	18
FIG. 3. 2. 1 Time-of-Flight Detector Geometry	24
FIG. 3. 3. 1 Schematic Diagram of the Time-of-Flight Detector	26
FIG. 3. 3. 2 Time-of-Flight Detection System Block Diagram	29
FIG. 3. 4. 1 Variation of Ion Current with Emission Current Showing Effect of Electron Energy	33
FIG. 3. 4. 2 Variation of Ion Current with Ion Extraction Voltage	35
FIG. 4. 1. 1 Shutter Functions	44
FIG. 4. 3. 1 Chopper Discs	51
FIG. 4. 4. 1 Variation of Δt , Δt_{pp} and S with Chopping Period.	52
FIG. 4. 4. 2 Relative Change in Half-width vs Resolution	54
FIG. 5. 1. 1 Basic Geometry of the Molecular Beam	57
FIG. 5. 2. 1 Argon Total Centerline Intensity at Optimum Nozzle-Skimmer Separation.	59
FIG. 5. 2. 2 Argon Total Centerline Density at Optimum Nozzle-Skimmer Separation.	60
FIG. 5. 2. 3 Nitrogen Total Centerline Intensity at Optimum Nozzle-Skimmer Separation.	63
FIG. 5. 2. 4 Nitrogen Total Centerline Density at Optimum Nozzle-Skimmer Separation.	64
FIG. 5. 2. 5 Centerline Particle Density vs Nozzle-Skimmer Separation	66
FIG. 5. 2. 6 Typical Beam Profile	68
FIG. 5. 2. 7 Beam Density Profiles vs Source Pressure	69

	<u>Page</u>
FIG. 5.2.8 Definition of Beam Core and Half-Shadow Regions . .	70
FIG. 5.2.9 Beam Density Profiles vs Nozzle-Skimmer Separation	72
FIG. 5.3.1 Argon Speed Distribution vs Source Pressure P_o at Optimum Nozzle-Skimmer Separation	74
FIG. 5.3.2 Nitrogen Speed Distribution vs Source Pressure P_o at Optimum Nozzle-Skimmer Separation	75
FIG. 5.3.3 Variation in Argon Speed Ratio with Nozzle Skimmer Separation on Axis at Different Source Pressure.	76
FIG. 5.3.4 Variation in Nitrogen Speed Ratio with Nozzle Skimmer Separation on Axis at Different Source Pressure.	77
FIG. 5.3.5 Variation in Speed Ratio with Off-Axis Displacement $X_s < X_{s \text{ opt.}}$	79
FIG. 5.3.6 Variation in Speed Ratio with Off-Axis Displacement $X_s > X_{s \text{ opt.}}$	80
FIG. 5.3.7 Variation of Speed Ratio and Particle Density with Nozzle-Skimmer Separation at $Y = +42.5 \text{ mm}$. .	83
FIG. D.1 Effect of Circular Beam Cross-Section on Shutter Function	108

LIST OF TABLES

	<u>Page</u>
TABLE 5.1 Beam Geometries	56
TABLE 5.2 Geometry A	56
TABLE 5.3 Core and Half-Shadow for Beam Geometry A	67

LIST OF SYMBOLS

a	Ratio of time of flight to maximum, t_m , to time of flight to half maximum, t_1 or t_2
A	Detector entrance area
A, A', A''	Constants in the distribution function
B	Defined as βL^2
c	Peripheral speed of the chopper disc
CTC	Characteristic time constant for Waveform Eductor
d	Nozzle pull-out distance
D	Diameter
E	Electric field strength
$f(\vec{v})$	Velocity distribution function for the density
$f(v)$	Speed distribution function for the density
$g(a)$	Function of a, defined in Section 3.6
$g(v)$	Speed distribution function for the flux = $\frac{dI(v)}{dv}$
$g(t)$	Shutter function
G	Mass flow
$h(a)$	Function of a, defined in Section 3.6
H	Strength of the magnetic field
i	Current
i^-	Electron current
i^+	Ion current
I	Beam flux (particles/cm ² sec or particles/sterad sec)
I(t)	Transmitted fraction of beam flux
I_0	Uninterrupted molecular beam flux
k	Boltzmann constant
l	Electron path length in TOF detector
l_t	Beam dimension in tangential direction
l_r	Beam dimension in radial direction
L	Length of flight path; i. e., distance from chopper disc to active zone of the detector

m	Molecular mass
\dot{m}	Mass flow rate
n	Particle density
N	Noise
P_o	Nozzle source pressure
P_1, P_a	Pressure in nozzle discharge chamber C_1
P_2	Pressure in collimation chamber C_2
P_3	Pressure in detection chamber C_3
P_{32}	Fore-pressure for diffusion pump S_3
P_{21}	Fore-pressure for diffusion pump S_2
P_{10}	Fore-pressure for diffusion pump S_1
P_o/P_1	Expansion ratio
q	Unit charge
Q	Beam cross-section = $l_t \times l_r$
r	Radius
r_s^*	Radius of characteristic skimmer = $\frac{2X_s}{S_s}$
R	Resolution = $\frac{\Delta t}{T}$
R_L	Input resistor of preamplifier
s_t	Slit dimension in tangential direction
s_r	Slit dimension in radial direction
$S_o(t)$	Detector signal for infinitely narrow shutter functions
$S(t), S$	Actual detector signal
S/N	Signal-to-noise ratio
S	Speed ratio = $v_o / \sqrt{\frac{2kT_e}{m}}$
t	Time
t_m	Time of flight to maximum detector signal
t_1, t_2	Time of flight to half-maximum of detector signal
t_o	$\frac{L}{v_o}$
t_s	Sweep time of Waveform Eductor

T_e	Flow temperature of the gas
T_c	Chopping period
T	Shutter function half-width
U	Voltages
v	Velocity
v_o	Streaming velocity
X	Distances downstream of the nozzle
X_M	Distance of Mach disc from nozzle
Y	Distances normal to the beam axis
Y_{HS}	Distance normal to the beam axis corresponding to half-shadow points
β	$\frac{m}{2 k T_e}$
δL	Extent of active zone of the detector
Δt_o	Half-width corresponding to $S_o(t)$
Δt	Half-width of detector signal $S(t)$
Δt_{pp}	Half-width of the photo-pulse
Δf	Bandwidth of the amplifier
σ	Ionization cross-section
$d\Omega$	Solid angle

SUBSCRIPTS

a	Detector entrance aperture
co	Collimator orifice
ch	Chopper disc
d	Detector plane
s	Skimmer orifice
s_o	Skimmer orifice with zero nozzle pull-out distance
n	Nozzle
em	Emission parameter

rep	Repeller parameter
ion	Ion parameter
eff	Effective values
bkg	Background

SECTION I

INTRODUCTION

1.1 GENERAL BACKGROUND

Molecular beam experiments have for many years been recognized as a powerful method for obtaining fundamental information about atomic and molecular collision phenomena. A molecular beam apparatus can be considered to be the low energy analog of a high-energy accelerator and provides a direct method of observation of the interaction of neutral molecules with solid surfaces and with other molecules. The classical method of molecular beam production using an effusive ("oven") source suffers from two major disadvantages; viz., low beam intensity and large velocity spread in the beam. The use of a supersonic nozzle as a molecular beam source was suggested by Kantrowitz and Grey in 1951 ^{(1)*}, and a large number of molecular beam systems of this type have been built, both in the United States and abroad. However, beam performance has been found to be substantially below the theoretical predictions. Consequently, considerable attention has been directed towards obtaining a clearer understanding of the various beam formation processes. At the present time, sufficient understanding of the factors influencing nozzle beam performance is available such that the complete design of a molecular beam system of given performance characteristics can be achieved. The aerodynamic molecular beam facility at the University of Virginia, to be described in this report, represents one such system.

*Numbers in parentheses refer to bibliography at the end.

1.2 THE RESEARCH PROGRAM

The general research program at the University of Virginia in the field of atomic and molecular collision phenomena is concerned with three interrelated problem areas; viz., gas-surface interactions, elastic scattering problems in fluid mechanics, and inelastic gas scattering. The molecular beam system described herein was designed for initial use in the first and second areas. However, before beam scattering experiments can be performed, it is necessary to obtain detailed information on the characteristics of the incident beam. One of the major objectives of the present study was to verify the satisfactory performance of the molecular beam system, and to provide information on direct beam properties; e.g., center-line intensity, beam profile, and beam speed distribution, which are necessary for the interpretation of results obtained from surface scattering experiments. In addition, an investigation of skimmer interaction, by measuring the distribution of particle speeds in the low intensity portions ("tails") of the beam profile has been completed.

Finally, the design and performance of the various components of the molecular beam system and the design criteria for a time-of-flight detection system are presented and discussed; and the observed performance of the beam modulation system is compared with theoretical predictions.

SECTION II

GENERAL DESCRIPTION OF THE VACUUM SYSTEM

2.1 INTRODUCTION

In this section a brief description of the vacuum system and important features of the new molecular beam system are presented.

The molecular beam system consists of three important parts; viz.,

1. The nozzle discharge chamber C_1 .
2. The collimation chamber C_2 .
3. The detection chamber C_3 .

The basic design and functional requirements of these three components, which is directly related to the basic design of the beam defining elements, will be considered separately in the following sections. The beam defining elements are discussed prior to a general description of the vacuum system. A three dimensional view of the important parts of the system is presented in Figure (2.1.1). A schematic diagram of the entire system is presented in Figure (2.1.2).

2.2 DESIGN OF THE BEAM DEFINING ELEMENTS

Numerical calculations regarding the design of the beam system will be found in Appendix A. The general considerations regarding the design are discussed below.

Nozzle. A simple conical, converging nozzle is used to produce the aerodynamic molecular beam. An important factor in the success of the free jet expansion process for molecular beam production and other related experiments is the existence of large flow-field gradients, resulting

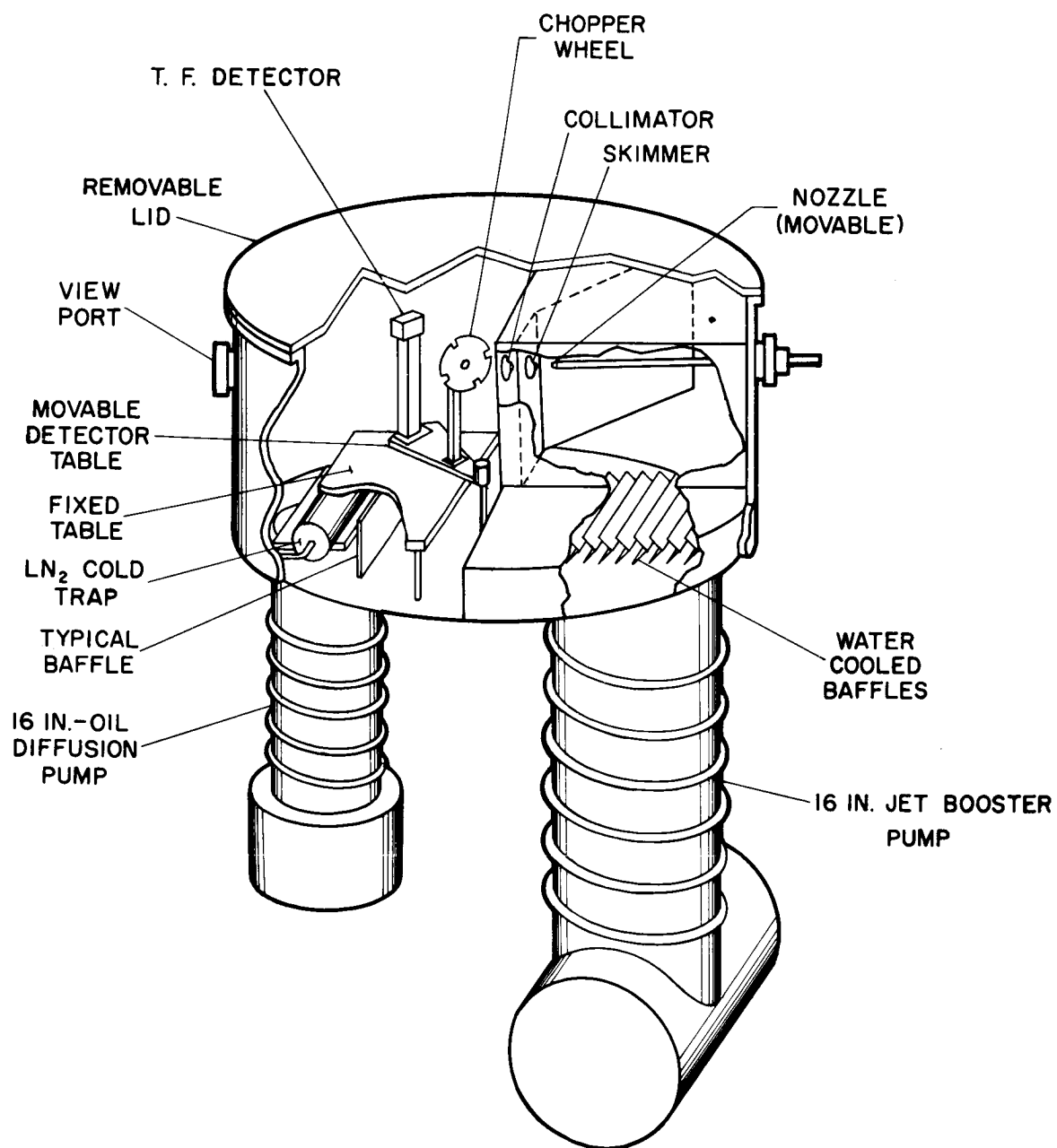


FIG. 2.1.1 MOLECULAR BEAM SYSTEM

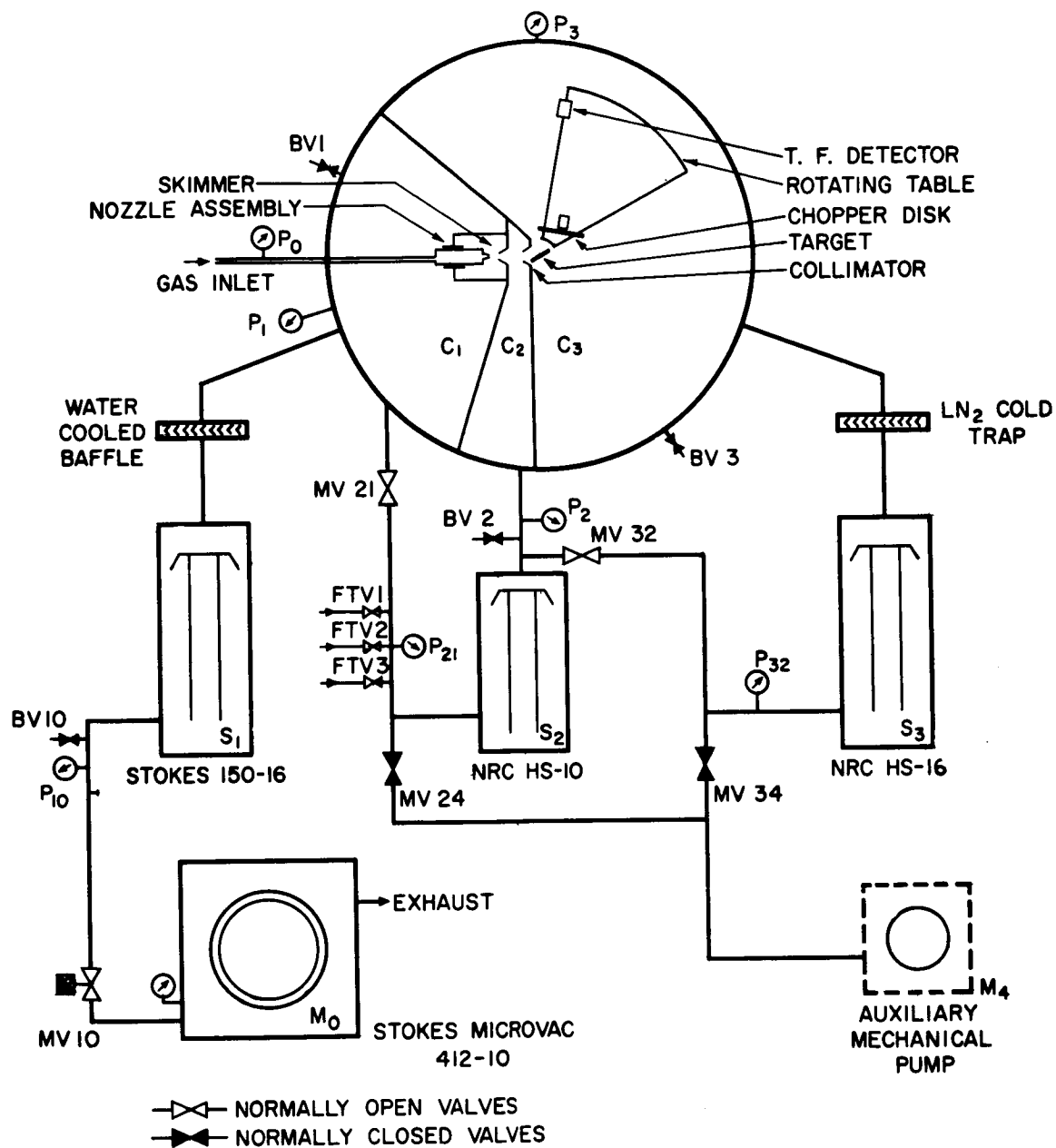


FIGURE 2.1.2 MOLECULAR BEAM APPARATUS VACUUM SYSTEM

in substantial departures from local thermodynamic equilibrium, which allow the use of higher source pressures before the limiting effects of condensation appear in the flow. A higher molecular beam intensity may be obtained by the use of contoured or slit-type nozzles. However, such arrangements result in a reduction of all flow field gradients; and, consequently, condensation will occur at larger source Knudsen numbers (based on source density and nozzle throat width). Furthermore, the use of a contoured nozzle introduces viscous effects in the flow which further reduce attainable beam intensity. These effects are discussed in the paper by Hagen and Morton⁽²⁾. For a given mass flow through the nozzle, the source Knudsen number is proportional to D_n , the nozzle diameter. Therefore, decreasing the nozzle diameter will be expected to yield an increase in speed ratio and total intensity of the molecular beam. This decrease in D_n is limited, however, by the onset of condensation in the beam gas, and the optimum nozzle size depends on the nature of the beam gas. According to previous results of Schüller⁽³⁾ and Bier and Hagen⁽⁴⁾ the optimum nozzle size for nitrogen was found to be 0.05 mm diameter; whereas for argon the nozzle size should lie between 0.05 and 0.15 mm diameter. For CO_2 the nozzle of diameter = 0.15 mm resulted in the maximum beam intensity and speed ratio. The advantages of using a small nozzle diameter have also been discussed in an earlier article by Scott and Drewry⁽⁵⁾. On the basis of these considerations a nozzle diameter of 0.05 to 0.10 mm was selected. (The actual nozzle obtained from the machine shop had a diameter of 0.06 mm.) The converging part of the nozzle has a conical shape with an included angle of 70° .

For high source temperature experiments an even smaller nozzle will be desirable.

The maximum source pressure that can be used depends on the nozzle discharge chamber pump characteristics and/or on the onset of condensation. On the basis of the results presented in reference (4), condensation is not expected to be important for a nozzle diameter of 0.06 mm. provided that the source pressure does not exceed the following values for the corresponding beam gas: carbon dioxide 1000 torr, argon 1400 torr, and nitrogen 8000 torr.

Figures (2.2.1) and (2.2.2) show the details of the nozzle assembly. The nozzle-skimmer separation distance X_s is an important parameter in molecular beam experiments, and can be easily varied from approximately 4 mm. to 50 mm. from outside the vacuum system by sliding the nozzle assembly in the cage assembly. The separation can be measured by means of vernier callipers outside the chamber.

The experimental results to be presented have been obtained with the nozzle source at room temperature. However, future experiments are to be performed at higher source temperatures, and the nozzle assembly has been designed for this purpose. All of the components are of stainless steel construction.

Skimmer. The skimmer is probably the most important element for the successful performance of a nozzle beam system. The skimmer design in common use in molecular beam systems is that of a conical element with a sufficiently small external angle and a sharp edge. Skimmer design criteria have been discussed by Zapata⁽⁶⁾ and by Bier and Hagen⁽⁴⁾.

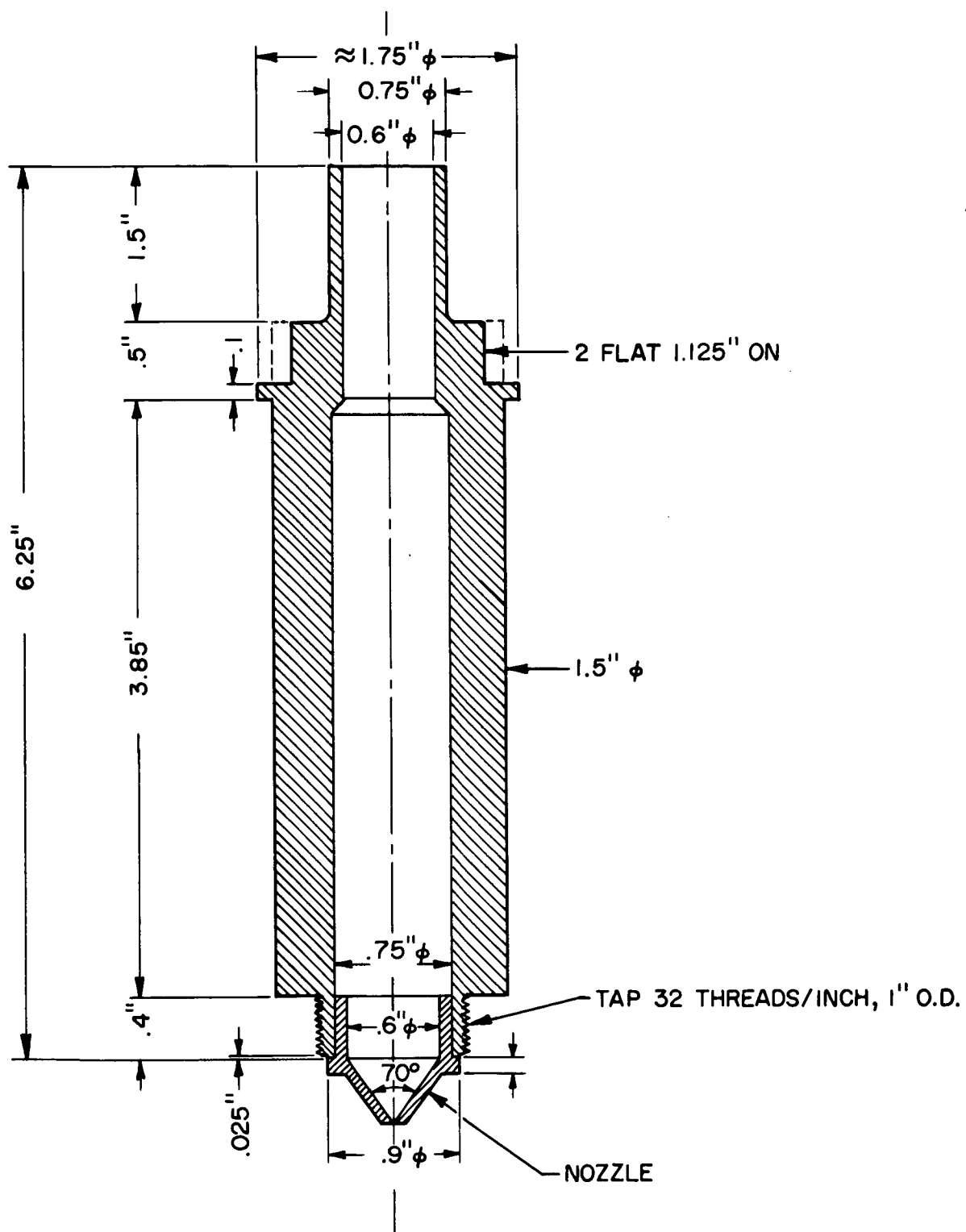


FIG. 2.2.1 NOZZLE ASSEMBLY

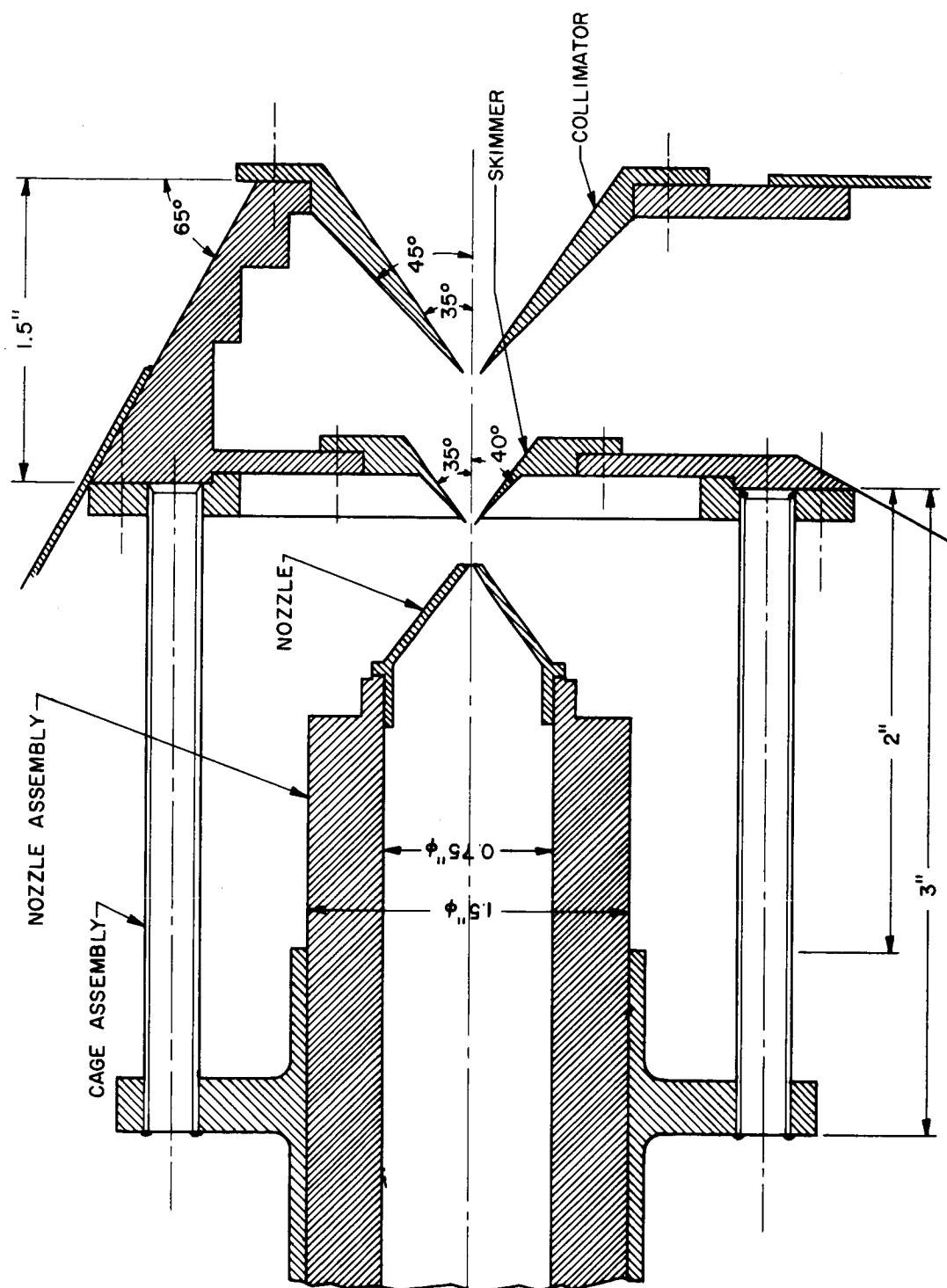


FIG. 2.2.2 NOZZLE DISCHARGE CHAMBER C₁ AND COLLIMATION CHAMBER C₂.

The object of proper skimmer design is: (i) to avoid the formation of a detached shock in front of the skimmer. This criterion restricts the maximum external angle of the skimmer cone. Also, it is desirable to keep the external angle small in order to decrease the number of molecules reflected from the outer wall which can interact with the nozzle flow. (ii) to minimize skimmer interaction with the flow upstream and downstream of the skimmer entrance, which adversely affects both the intensity and the speed ratio of the final beam. The internal cone angle of the skimmer must be designed to minimize collisions of beam molecules with the inner wall of the skimmer. Hence, a large internal cone angle is required. The final design is a compromise between these two conflicting requirements.

Manufacturing requirements dictate the thickness of the skimmer walls. Figure (2.2.3) shows a schematic diagram of a typical skimmer. A wedge angle of 5° with internal and external included cone angles of 70° and 80° , respectively, was chosen on the basis of previous experimental results. It is desirable to keep the length of the skimmer as small as possible in order to (i) limit the skimmer interaction by decreasing the probability of repeated reflections of molecules from the inner walls of the skimmer and (ii) to improve the conductance of the collimation chamber (for small skimmer-collimator distance).

The effect of skimmer size on the beam intensity has been discussed in Reference (2). For optimum centerline intensity, the skimmer radius r_s should at least be equal to the characteristic skimmer radius, r_s^* , where $r_s^* \equiv 2 X_s / S_s$. Here, X_s is the nozzle-skimmer distance and S_s is the isentropic speed ratio at X_s . The assumption that S_s has the

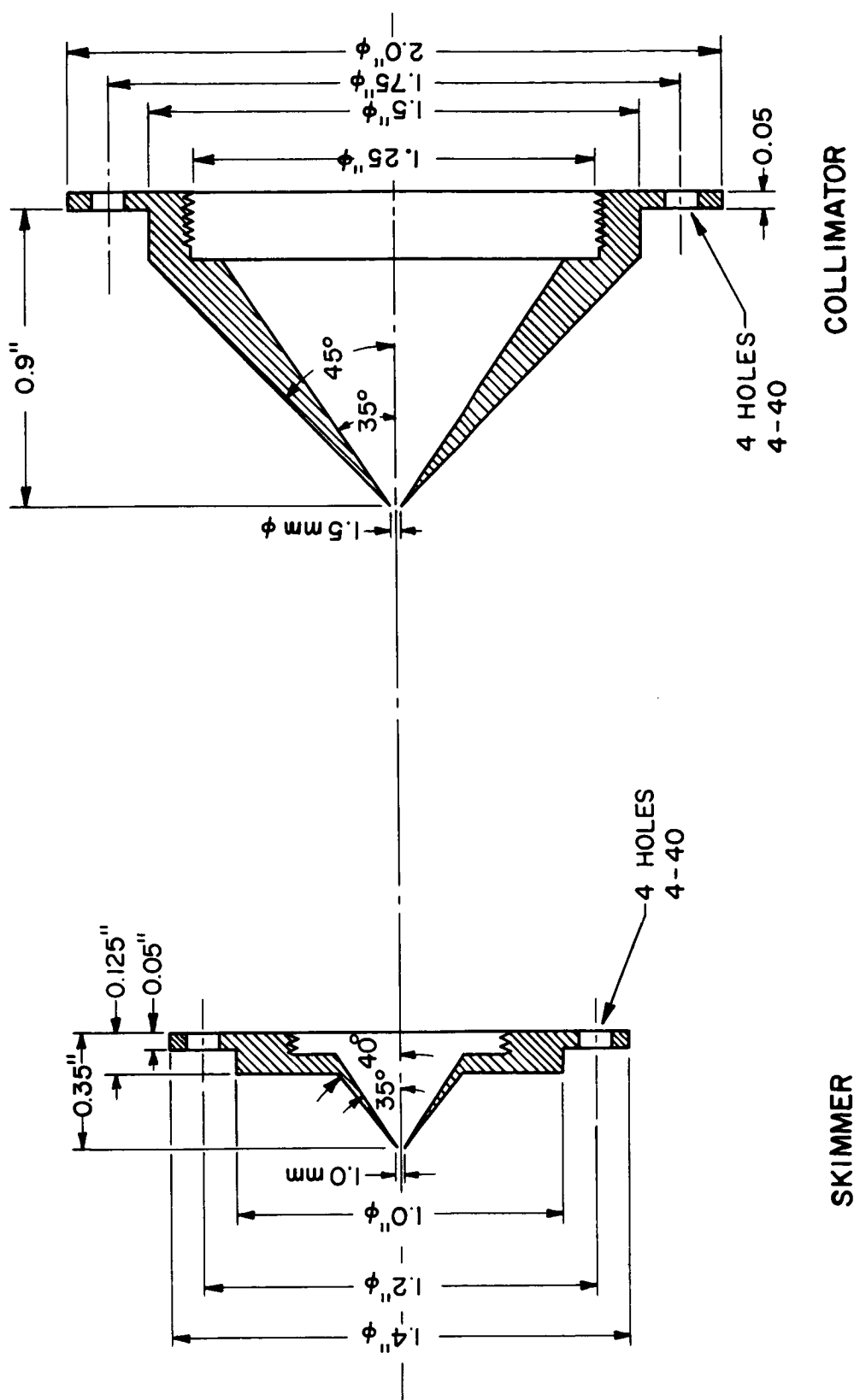


FIG. 2.2.3 DETAILS OF SKIMMER AND COLLIMATOR

isentropic value is reasonable since the perpendicular temperature in the flux field (which affects the speed ratio used in the definition of r_s^*), continues to decrease as in an isentropic flow well beyond the point where the parallel temperature is becoming constant. Using the isentropic variation of S_s with X_s , one gets for a monatomic gas⁽²⁾:

$$r_s^* / D_n \approx 0.67 \cdot (X_s / D_n)^{1/3}$$

For $X_s = 6.5$ mm. and $D_n = 0.06$ mm., this yields $r_s^* \approx 0.2$ mm. The skimmer most commonly in use during these experiments had a diameter of 1 mm. Four skimmers of the same basic design, made of aluminum, with diameters of 0.7, 1.0, 1.3 and 2.0 mm., each of nearly 8 mm. length are available.

Collimator. The collimator is the second beam-defining orifice and its design is very similar to that of the skimmer. (See Figure 2.2.3). The requirements of suitable inner and outer cone angles and a sharp leading edge are less critical for the collimator since the flow in this region is nearly free-molecular, and continuum-like discontinuities will not occur.

The size of the collimator is dictated mainly by the desired beam cross-section at the target. For the experiments described herein, the collimator had a diameter of 1.5 mm. and was the beam core defining orifice. Two other collimators, 1.35 and 2.5 mm. in diameter, with the same basic

design, are available for further experiments. The collimators are also made of aluminum.

2.3 DESCRIPTION OF THE VACUUM CHAMBERS

The Nozzle Discharge Chamber C_1 . Figure (2.2.2) shows a general view of the nozzle discharge chamber. The three basic components of the beam producing system which may be considered to be connected with this chamber are (i) the gas supply system, (ii) the nozzle and (iii) the skimmer.

Gas Supply System. Facilities are provided for quick changeover from one gas to another. At present, experiments are being performed with argon, nitrogen and carbon dioxide. The gases are obtained in high pressure bottles from commercial sources. The high pressure bottle is connected to the nozzle inlet by a length of flexible tubing. The source pressure in the nozzle is controlled with a regulator valve and can be read to within 25 torr with a Wallace and Tiernan gage with a range of 0 to 5000 torr. The gas supply line can either be exhausted to the atmosphere (when at high source pressures) or evacuated by connecting it to the bleed valve, BV_1 . (See Figure 2.1.2)

The nozzle discharge chamber collects the fraction of the nozzle flow which does not pass through the skimmer. A Stokes Model 150 Series 16" Ring Jet Booster Pump with a maximum pumping speed of 4500 lit/sec is used to evacuate the nozzle discharge chamber. Under normal operating conditions the pressure P_1 in the chamber ranges from 10^{-4} to 10^{-3} torr, depending on the nozzle source pressure P_0 , and the Mach-disc distance ⁽⁴⁾ of $X_M \approx 60$ mm. is much greater than the usual skimmer

distance of 5 - 10 mm. The small background density in the nozzle discharge chamber reduces the beam attenuation, if any, due to interaction of the nozzle flow with the background gas between the nozzle exit and skimmer entrance.

The nozzle discharge chamber pressure P_1 is monitored by an Alphatron gage.

Collimation Chamber C_2 . The general view of the collimation chamber is presented in Figure (2.2.2). The chamber is a pie-shaped section constructed with the specific objective of reducing the skimmer-collimator path length while maintaining a reasonably large flow conductance and a pressure at least an order of magnitude lower than the pressure in the nozzle discharge chamber. The pumping requirements in the collimation chamber are very severe - the objective being to maintain the density of the background gas at a sufficiently low value such that collisions between beam molecules and background gas do not result in appreciable beam attenuation. Consequently, the mean free path of the background gas should be considerably greater than the path length for the beam molecules. The chamber C_2 was constructed with the unusual shape in order to achieve this objective. Attempts to decrease the path length further will defeat the purpose since the corresponding decrease in flow conductance will result in a rise in the background pressure for a given pumping speed. Prevention of beam and background gas collisions is especially important in the collimation chamber since, for a well-collimated beam, even small angle scattering events will result in removal of beam molecules. The gas load in the collimation chamber is relatively high, since the pumps must remove nearly all of the mass flow passing through the skimmer. The col-

limation chamber pump is an NRC Model HS-10-4200 10" diffusion pump with a nominal pumping speed of 4200 lit/sec. The collimation chamber pressure varies from 10^{-6} to 10^{-4} torr depending on the nozzle source pressure and the nozzle-skimmer separation.

Detection Chamber C₃. The general geometry of the detection chamber is shown in Figure (2.1.2). The detection chamber contains the beam modulation and detection systems. The primary objective of this molecular beam system is to carry out surface scattering experiments. Consequently, the detection chamber was designed to meet this objective. The targets for the scattering experiments are fixed in a target holder connected to a rotary shaft whose position in three rectangular coordinates can be adjusted from outside. The angular position of the target is indicated by a scale attached to the rotary shaft. The target can be used also as a shutter for direct beam experiments.

The detector and beam modulation system are mounted on a table which rotates about the axis of the chamber (coincident with the axis of rotation of the target). The detector can be moved over an angular range of 200° . The beam modulation system consists of the chopper disc, the drive motor, and the light source and sensing system which is used to establish a reference point (zero time) for the time-of-flight measurements. The angular resolution of the detection system can readily be changed by changing the radial position of the detector up to a distance from the center of about 50 cm. Also, apertures of various size and shape can be put in front of the detector. For most of the experiments, the detector was 30.4 cm away from the center and its effective entrance aperture was 5 mm. in diameter. To minimize the effect of motor

vibrations on the detector, the detector and the chopper components are mounted on vibration dampers.

The detection chamber pressure is designed to vary from 10^{-8} to 10^{-7} torr, depending on beam intensity. The background pressure P_3 in the detection chamber is measured with a G. E. ionization gage. The chamber is evacuated by an NRC Model HS-16-10,000 diffusion pump with a maximum pumping speed of 10,000 lit/sec. A liquid nitrogen cooled cold trap is located at the entrance to this pump (see Figure 2.1.1). It is shielded in order to decrease the radiant heat input from the surrounding higher temperature surfaces. Under optimum operating conditions, a liquid nitrogen loss rate of 1 lit/hour was measured. A simple semi-automatic system is used to refill the cold trap. It consists of a timer which operates at regular set intervals, for a given time, a solenoid valve in a high pressure air line to transfer liquid nitrogen from the supply dewar to the cold trap.

The entire molecular beam system has been designed to allow future modifications and/or improvements with ease. A number of extra flanges have been provided for installation of additional equipment as may be needed. For example, a low energy electron diffraction system may be used to monitor the target surface structure, etc. Extra electrical feed-throughs have been installed with the same object in view. The system is now going to be used for scattering experiments with heated targets and experiments with heated nozzle sources are contemplated in the near future.

2.4 CONTROL CIRCUITS AND SAFETY FEATURES OF THE SYSTEM

In order to produce the low pressures and the steady state conditions required for experiments, it is necessary to pump continuously on the beam system. Consequently, the pumping system must be left unattended for long periods of time; and various safety features have been built into the system to provide for fail-safe operation. A schematic diagram of the pump control circuits is shown in Figure (2.4.1). A bi-metallic, temperature-sensitive switch is attached to the cooling water outlet line of each pump. It causes an immediate shutdown of the pump if it overheats due to lack of cooling water. The mechanical pump M_o can be started whenever its temperature switch is in the closed position. The diffusion pumps, however, cannot be started until the pressure P_{10} drops below a given (adjustable) value and a pressure-sensitive relay switch closes. While the automatic pressure and temperature control can be bypassed by manually operating the respective override switches, the diffusion pumps do not start without the mechanical pump being switched on. Faulty operation of the mechanical pump (for example, due to an electrical overload or a broken drive belt) will result in the shutdown of all diffusion pumps, due to the increase in P_{10} , in order to prevent their operation with high forepressures. The system is designed so that it will restart automatically after a temporary interruption of electric power. The detector filament is protected by connecting the filament power supply through a relay that opens if P_3 exceeds a preset value. This relay must be reset manually.

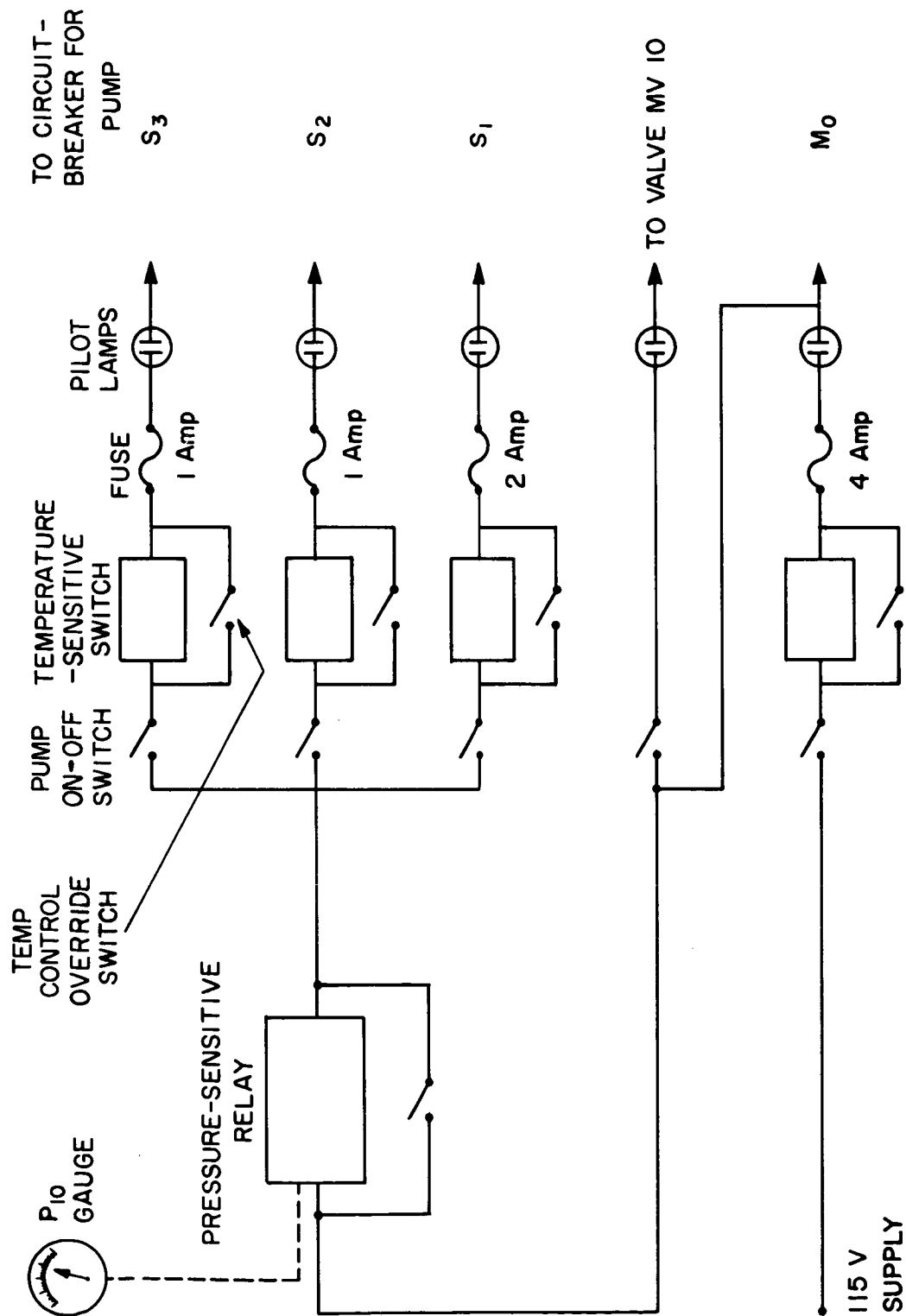


FIG. 2.4.1 SCHEMATIC DIAGRAM OF PUMP CONTROL PANEL

These protection systems have proved to be very reliable, and the system can and has been left unattended for extended periods of time (several days).

2.5 VACUUM SYSTEM PERFORMANCE

Normal operating pressure in the detection chamber C_3 during an experiment ranges from 1×10^{-7} torr to 5×10^{-7} torr. The lowest pressure observed (with the cold trap in operation) was 1×10^{-8} torr.

Other representative pressures in various parts of the system are:

Nozzle and source chamber (measured by Alphatron)

$$P_1 \equiv P_a = 1 \times 10^{-4} \text{ torr}$$

Collimation chamber pressure (measured by G. E. Ionization Gage)

$$P_2 = 5 \times 10^{-6} \text{ torr}$$

Detection chamber pressure (measured by G. E. Ionization Gage)

$$P_3 = 2 \times 10^{-8} \text{ torr}$$

Pump forepressures (measured by thermocouple gages)

$$P_{32} < 1.0 \text{ micron}$$

$$P_{21} < 10 \text{ microns}$$

$$P_{10} < 10 \text{ microns}$$

The relatively fast pump-down capability enables the apparatus to be used for a number of different experiments (which may require opening the system and making necessary changes) to be performed without difficulty or inconvenience. Furthermore, the design and arrangement of the system permits complete operation by one person. A simple device enables the heavy cover plate of the chamber to be jacked up and moved

on rollers to one side in order to enable convenient access to all of the internal parts. An operating procedure for the various subsystems of the molecular beam system has been included in Appendix E for reference purposes.

SECTION III

MOLECULAR BEAM DETECTION SYSTEM

3.1 INTRODUCTION

One of the fundamental problems associated with molecular beam experiments is the quantitative detection of beam molecules. Many different kinds of detectors have been designed and used; e. g., surface ionization detectors, electron-bombardment ionizers, Pirani gage detectors, and detectors for radioactive materials. The earlier molecular beam system at the University of Virginia used a flux-sensitive differential ionization gage system⁽⁵⁾.

The time-of-flight detector (TFD), sometimes called "universal detector", "Density detector", or "through-flow detector" was developed together with the so-called time-of-flight technique. The TFD operates as follows: As the molecular beam passes straight through the detector, a fraction of the beam is ionized by electron impact. The resulting ions are collected, the ion current being proportional to the density at the detector.

As with stagnation-type flux-sensitive detectors (Pirani detector, ionization gage), a bridge arrangement of two TFDs can be used to measure the density of a steady beam. However, the primary use of the TFD is in conjunction with time-of-flight experiments which require the measurement of a short pulse of beam particles. With suitably designed amplifiers the final signal of a TFD is a true response of the original beam pulse.

3.2 DESIGN OF THE TIME-OF-FLIGHT DETECTOR

The design requirements of a time-of-flight detector involve the consideration of three criteria; viz., the problems related to the molecular beam, the ionizing electron beam, and ion detection and collection. Since a strong coupling exists between these criteria, the requirements for each are often contradictory. Consequently, a suitable detector design results from a compromise between conflicting requirements.

The Molecular Beam. The cross-section of the molecular beam at the detector is usually defined by the entrance aperture of the TFD. The dimensions of this aperture influence the angular resolution in; e. g., scattering experiments as well as the speed resolution in time-of-flight measurements. Uniform angular resolution requires a circular or, at least a squared cross-section, whereas speed distribution measurements ask for a rectangular shape: an increase of the length of the rectangle in the radial direction of the rotating disc increases the available beam cross-section and, therefore, the possible signal without decreasing the velocity resolution.

The Ionizing Electron Beam. If the molecular beam coincides with the z-axis of a rectangular coordinate system (see Figure 3.2.1), the ionizing electron beam lies usually in a plane $z = \text{constant}$ with the cathode being; e. g., parallel to the y-axis and the electrons moving in the x-direction. To prevent a spreading of the electrons in the z-direction, due to the space-charge of the beam, the electron beam is usually focused by a magnetic field H_x of some hundred gauss. The resulting thin electron

layer is necessary for high resolution in time-of-flight measurements. The y - dimension of the electron beam should be matched to the y - dimension of the molecular beam. A narrower electron beam does not use the whole molecular beam, while a broader beam increases the background-ion current without increasing the signal current. For absolute density measurements it is necessary that a very high or at least known percentage of the emission current of the cathode passes through the molecular beam to be collected by the electron collector electrode. This imposes strict requirements on the alignment of the cathode with respect to the slits in the accelerating electrodes, on the width of these slits and on the magnitude of the focusing magnetic field H_x .

Ion Collection System. The ion collection system should have the following properties: (i) 100% collection efficiency for as high electron currents as possible, (ii) minimum distortion of the electron beam, (iii) no structural parts in the path of the molecular beam, and (iv) a small capacity of the ion collector to neighboring grounded parts. The actual design has to compromise between these properties: High electric fields to extract the ions against the space charge forces of the electron beam influence the electron beam itself. The electrical capacity of the collector to other structural parts decreases with increasing the distance, but then higher voltages are necessary to maintain the desired electric field strength. (This capacity together with the required high-frequency response of the detecting circuit determines the value of the maximum input resistor R_L ; the smaller C, the larger R_L and the better the signal-to-noise ratio.)

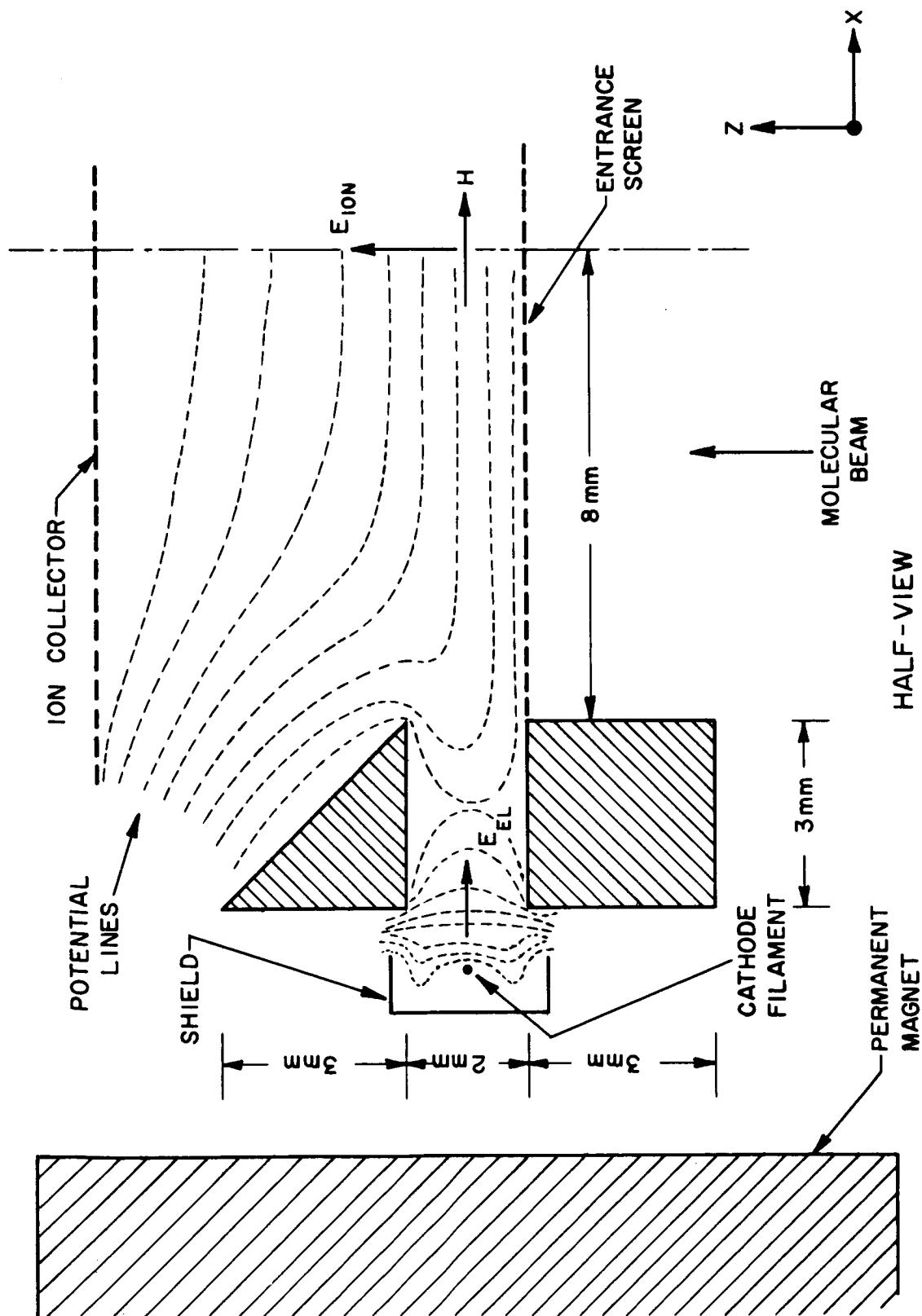


FIG. 3.2.1 TIME-OF-FLIGHT DETECTOR GEOMETRY

Up to now most of the TFDs extract the ions in the z-direction. For broad molecular beams this is more efficient than the extraction in the y-direction.

3.3 DESCRIPTION OF THE TIME-OF-FLIGHT DETECTOR

The distinguishing features of the time-of-flight detector used in these experiments are the larger ionizing region (or "active volume") and the use of much higher electron currents.

The four major components of the detector, shown schematically in Figure (3.3.1) are:

1) The ionization chamber with the electron and molecular beam apertures; 2) the cathode assembly; 3) the anode assembly identical to the cathode assembly, and 4) the ion collector.

The ionization chamber is fastened to the center of the magnet yoke which, in turn, is clamped to a supporting structure inside the detection chamber. The permanent magnet, with 41 mm diameter poles produces a magnetic field of about 350 gauss at the center of the gap of 38 mm. The other electrodes; i. e., the cathode, anode and the ion collector are mounted directly on the ionization chamber, with glass and teflon being used as insulating materials. The chamber has a molecular beam opening of 20 x 16 mm and is only 8 mm high. This helps to minimize multiple reflections of the small fraction of beam molecules scattered from the ion collector back into the ionization region. (This part of the contribution to the ion current is proportional to the beam flux rather than to the beam density.) The electron beam slits are 2 mm wide;

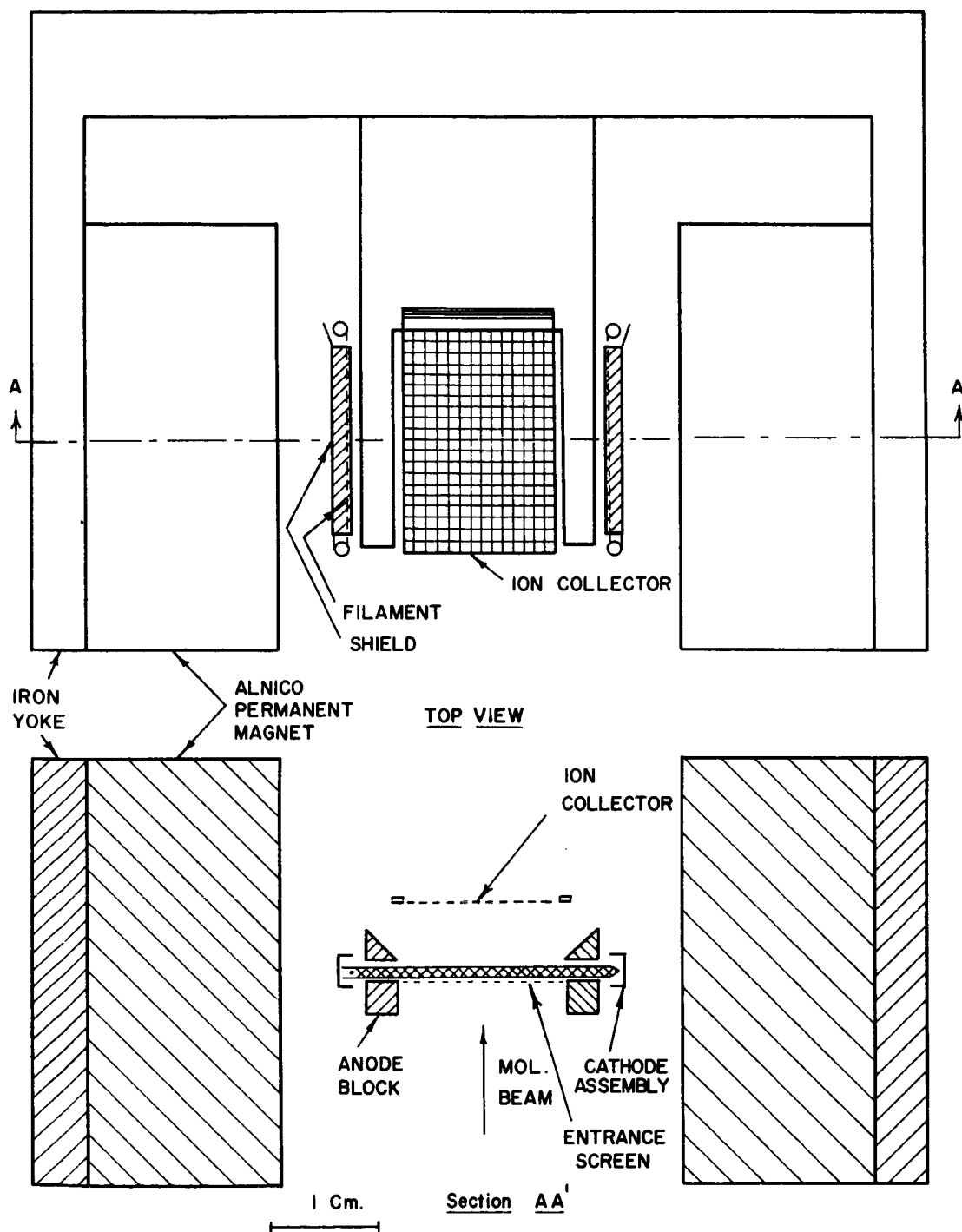


FIG. 3.3.1

SCHMATIC DIAGRAM OF THE
TIME-OF- FLIGHT DETECTOR

the electron beam is at least that narrow. The slits are 3 mm deep, minimizing the penetration of the acceleration field into the active volume (which would cause some ions to be accelerated towards the cathode). A 95% transparent tungsten mesh screen is used across the molecular beam entrance aperture in order to establish a uniform potential there, opposite the ion collector. For a given ion collector voltage this increases the collecting field in the active zone of the detector; i. e., where the electron beam crosses the molecular beam, and provides a more uniform collecting field.

To evaluate the exact path of an average electron travelling through the active volume requires an exact knowledge of the three-dimensional electrical and magnetic fields acting on the electron. Appendix B contains calculations of this type relating to the time-of-flight detector. The calculations show that for a properly aligned cathode operating under typical operating conditions, nearly all of the electrons will pass through the slits. The gyration of the electrons due to the focusing magnetic field will increase the path length by approximately 10% only.

The cathode assembly consists of a 0.2 mm diameter tungsten filament and a small U - shaped shield behind it. This shield is connected to either the positive or negative end of the filament. The emitting length of the filament is estimated to be 18 mm.

The anode assembly is identical to the cathode assembly. In case of a filament burnout, the anode and cathode are exchanged by

external switching, thus allowing further detector operation.

The ion collector is a frame of stainless steel covered with 95% transparent tungsten mesh screen which provides the ion collecting surface. The stainless steel frame is mounted directly on the ionization chamber, teflon being used as the insulating material.

Figure (3.3.2) shows a block diagram of the time-of-flight detector along with the associated electronic equipment. This equipment includes:

a) a regulated power supply for biasing the cathode at -100 to -350 V

b) an emission control circuit for providing the filament current and keeping the cathode emission current at a constant value. The filament requires about 4.5 A at 2 V, D. C. The control circuit is a modified version of that described by R. J. Kerr ⁽⁷⁾.

c) a regulated power supply (not shown in the Figure) for maintaining a voltage of about + 50 V on the anode to suppress emission of secondary electrons by the anode and to aid in focusing the electron beam through the slits.

d) ammeters (not shown) to measure the emission current i_{em} and the anode current i_{rep} .

e) batteries to bias the ion collector at - 90 V to - 300 V.

f) an electrometer (not shown) to measure the d - c component of the ion current.

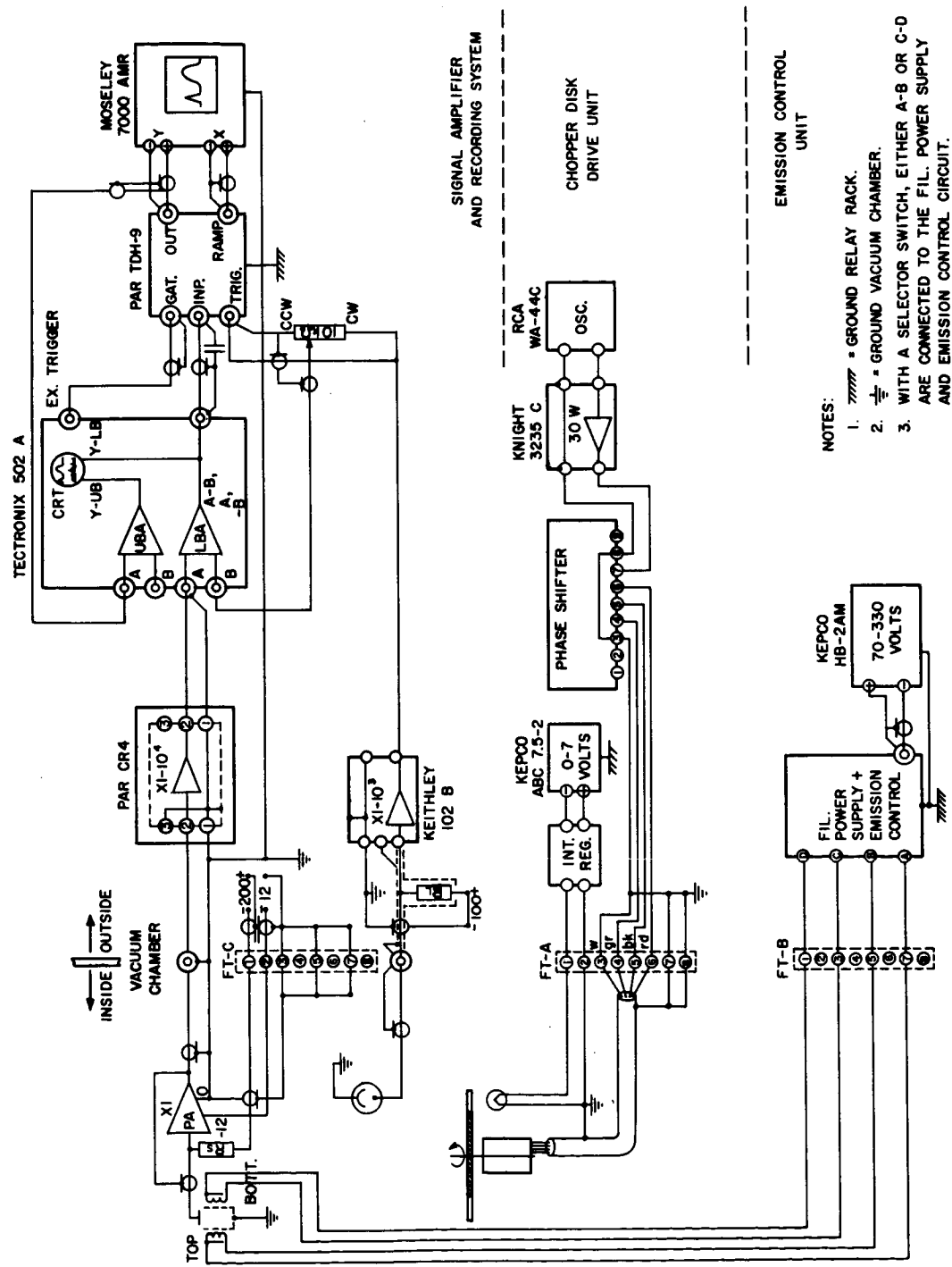


FIGURE 3.3.2 TIME-OF-FLIGHT DETECTION SYSTEM BLOCK DIAGRAM

The ion-collector current causes a voltage drop across the resistor R_L . This signal is fed into a solid state unity-gain preamplifier. The preamplifier is mounted on the detector support itself and is powered by a 12 V battery. The output of the preamplifier is conveyed through a coaxial cable to the other electronics outside the vacuum chamber. These electronics are described in detail later on in this section.

3.4 PERFORMANCE OF THE TIME-OF-FLIGHT DETECTOR

Initial tests on the detector were made by installing it in a small vacuum chamber with a base pressure of 10^{-6} torr. The results of these tests suggested minor improvements which were carried out. Thereafter, the detector has been tested in the molecular beam vacuum system itself.

Electron Beam. The interaction of the various detector parameters with the focusing of the electron beam was evaluated by simultaneously measuring the emission and repeller (anode) currents; i. e., i_{em} and i_{rep} , respectively. The ratio i_{rep} / i_{em} is a measure of the proper operation of the electron beam and, for an ideally designed detector, has a value of unity. If this ratio is, however, influenced by changing the direction of the filament current, this may be due to the change in the magnetic field of the filament current and/or the change in the relative potential of the U - shaped shield behind the filament which is connected to one end of the filament. The magnitude of this effect is also influenced by the accuracy of the cathode alignment. In one of

the earlier detectors, reversing the direction of the filament current caused a 50% drop in repeller current for constant i_{em} . For the detector currently in use the $i_{rep} / i_{em} \approx 0.9$ and is independent of the direction of the filament current.

The Ion Current i^+ . The ion current, i^+ , obtained from the detector may be calculated as

$$i^+ = i_{eff}^- \cdot l_{eff} \cdot \sigma_{eff} \cdot n$$

where i_{eff}^- is the effective electron current,

l_{eff} is the effective electron path length,

σ_{eff} is the effective cross-section for interaction between electrons and the gas molecules to produce ions, and

n is the local particle density at the detector.

The effective electron current is the electron current that crosses the active zone of the detector; i. e., the total emission current minus the electron losses at the walls of the entrance slit and at the entrance screen. The repeller current, i_{rep} , is less than i_{eff}^- since some of the electrons are unable to pass through the second slit. Thus, i_{eff}^- lies between i_{em} and i_{rep} and will generally be closer to the i_{rep} . The effective electron path length, l_{eff} , is given essentially by the length of the region from which all the ions produced are collected by the ion collector, plus the elongation of the electron path length due to the gyration of the electrons. The effective cross-section, σ_{eff} , depends on the nature of the gas and on the average electron energy

in the active zone of the detector. In the normal range of operation, this cross-section decreases with increasing electron energy. The particle density, n , at the detector is the quantity to be measured and depends on the molecular beam operating conditions.

The dependence of the ion current on the detector parameters can be explained qualitatively by the way these parameters influence i_{eff}^- , l_{eff} , and σ_{eff} , respectively. In general, the interactions of these parameters are quite complex; e. g., an increase in U_{e1} will probably decrease i_{eff}^- due to greater electron loss at the first slit and also decrease σ_{eff} due to the higher electron energy. A net loss of signal should result. This is shown to be true in Figure (3.4.1). The curves in Figure (3.4.1) demonstrate the excellent ion collection efficiency by the linear relationship between i^+ and i_{em} over a wide range of emission currents. (The cathode assembly and its power supply should allow emission currents of up to 50 mA. Care must be taken that the background pressure is sufficiently low; e. g., below 10^{-6} torr, before operating the detector at these high emission currents.) Figure (3.4.2) shows the effect of U_{ion} on the ion current i^+ . The sharp increase of i_{ion} for small values of U_{ion} results primarily from the growth, with increasing strength of the ion-collector field, of the zone from which ions are retrieved, and therefore, of $i_{\text{eff}}^- \cdot l_{\text{eff}}$. Superimposed on this effect is the increase in σ_{eff} due to the mean electron energy being smaller for a high U_{ion} . The slight decrease in i_{ion} at the highest value of U_{ion} can be explained by the increased electron losses, as shown by the decrease in $i_{\text{rep}} / i_{\text{em}}$ from 97% at $U_{\text{ion}} = -22.5$ V

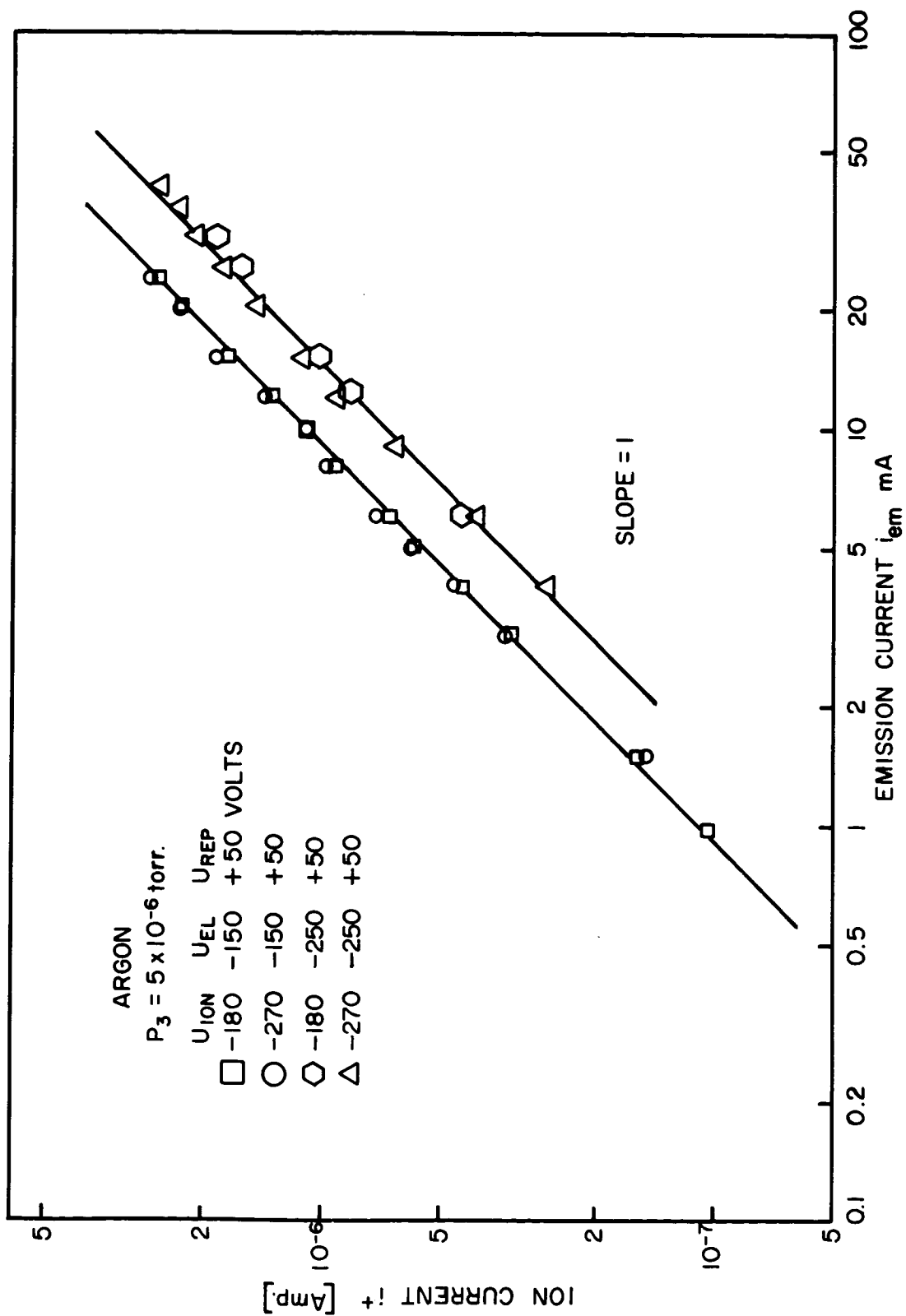


FIG. 3.4.1 VARIATION OF ION CURRENT WITH EMISSION CURRENT SHOWING EFFECT OF ELECTRON ENERGY.

to 70% at - 360 V.

While Figure (3.4.2) suggests a complete collection of all ions by the ion collector, more quantitative results can be obtained by comparing the measured ion current with the theoretical value of i^+ . Assuming

$$n = 1.62 \times 10^{+11} \text{ atoms/cm}^3 (\equiv 5 \times 10^{-6} \text{ torr at } T_o = 298^\circ\text{K})$$

$$\sigma_{\text{eff}} = 3 \times 10^{-16} \text{ cm}^2 (\equiv \sigma_{\text{argon}} \text{ at } 100 \text{ eV})$$

$$l_{\text{eff}} = 1.6 \text{ cm} (\equiv \text{maximum length of active zone})$$

$$i_{\text{eff}} = 10 \text{ mA}$$

an ion current of

$$(i^+)_{\text{theory}} = 7.8 \cdot 10^{-7} \text{ A}$$

is obtained. The experimental value from Figure (3.4.1) is, for $i_{\text{em}} = 10 \text{ mA}$ and $U_{\text{el}} = 150 \text{ V}$,

$$(i^+)_{\text{exp.}} = 1.1 \cdot 10^{-6} \text{ A}$$

which is higher than the theoretical i^+ by 30%. This discrepancy can be explained by:

(a) the neglect here of that contribution to i^+ consisting of secondary electrons emitted when the ions strike the ion collector. This effect is equivalent to an increase of i^+ by about 10%

(b) neglect of the elongation of the electron path length due to the magnetic field. This effect may increase l_{eff} by not more than 10%

(c) collection of ions formed in the entrance and exit-slit for the electron beam. This may increase l_{eff} by another 10%.

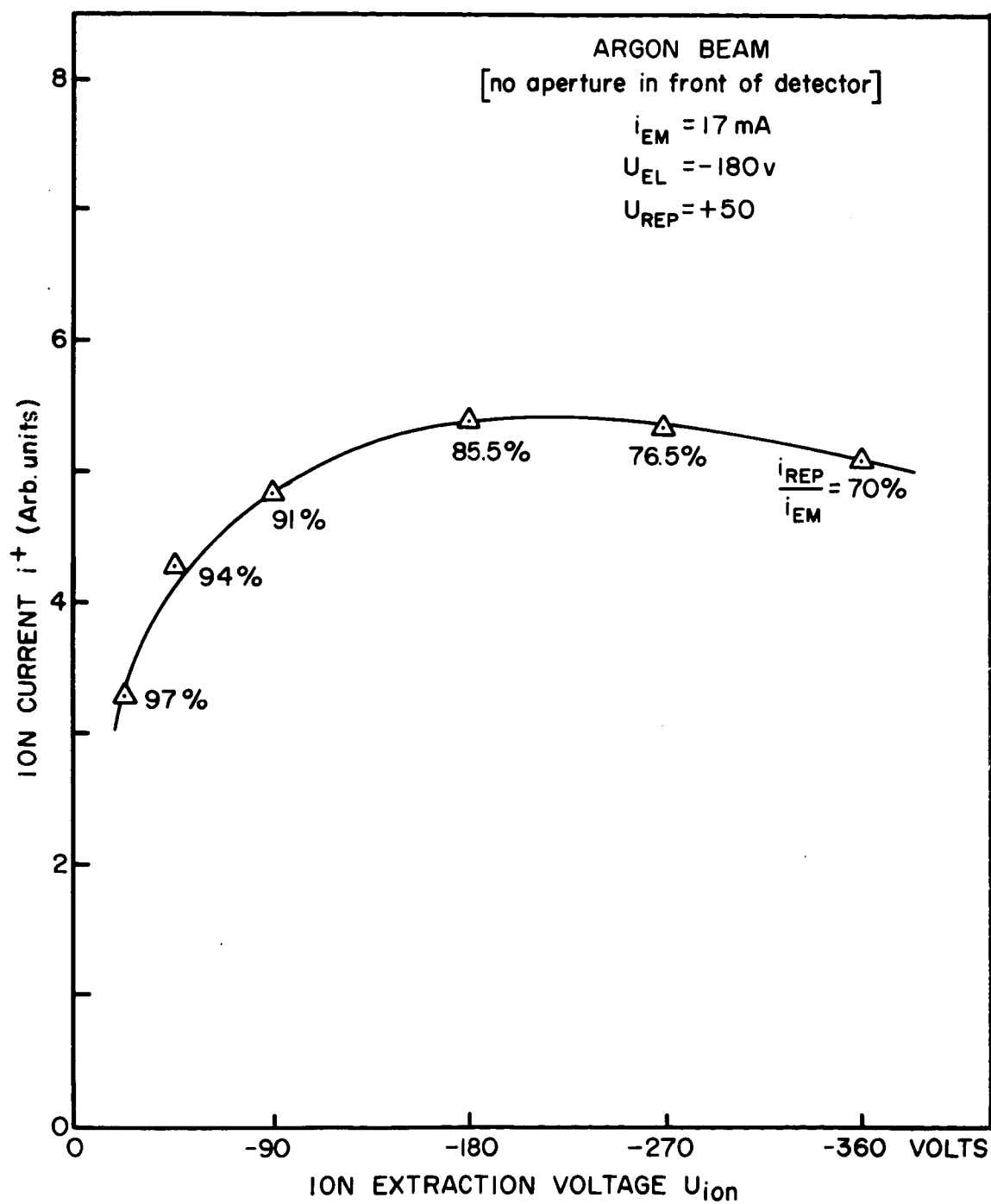


FIG. 3.4.2 VARIATION OF ION CURRENT WITH ION EXTRACTION VOLTAGE.

Perhaps more important is the uncertainty in the value for n , obtained from the pressure-reading of an uncalibrated ion-gage. In view of all of these facts the performance of the detector as expressed in Figures (3.4.1) and (3.4.2) is in good agreement with theoretical predictions.

3.5 SIGNAL ANALYSIS

The signal from the time-of-flight detector has to be amplified before it can be analyzed. The signal is first fed into a unity gain pre-amplifier which has an output impedance of the order of $1K\Omega$ (see Figure 3.3.2). The preamplifier was installed inside the vacuum chamber, close to the detector, to avoid the microphonic pick-up by the connecting signal cable. The cable shield is driven by the preamplifier output to minimize the input capacitance.

The detector signal is further amplified by the low noise wide-band amplifier, PAR Model CR-4. The output of this amplifier is fed into the dual-beam oscilloscope, where it is displayed together with the reference light signal. The output of the oscilloscope amplifier LBA is fed into a signal averaging and integrating device. Use of the oscilloscope amplifier adds to the flexibility of the gain settings and aids in the full use of the dynamic range of the signal averaging and integrating device. The signal averaging and integrating device is a PAR Model TDH-9 Waveform Eductor. A brief description of its principle of operation follows.

The average value of any single point of a signal which consists of a repetitive waveform plus random noise is simply the point value of the repetitive waveform itself, since the average value of the non-synchronous signals and random noise is zero. Thus, the instrument can extract the point-by-point value of the waveform itself by averaging the repetitive signal over a long period of time. The TDH-9 consecutively samples the input signal over 100 equal intervals each time it occurs. It separately integrates the signal over each interval by charging a capacitor. With each repetition of the waveform, the charge on each capacitor asymptotically approaches the average voltage of the waveform itself during that interval. Simultaneously with this sampling-averaging process, which is triggered each time the event under study occurs, the contents of the memory are available at the output of the Educator and can be displayed on the oscilloscope.

The Educator increases the signal-to-noise ratio by a factor equal to $(2 \times \text{CTC}/t_s)^{1/2}$ where CTC is the characteristic time constant (usually 5 sec) and t_s is the sweep time usually ranging from 300 μsec to 1 m sec. Consequently, the signal-to-noise ratio is increased by a factor of about 100. The instrument provides for slow readout of the stored information so that the averaged signal can be displayed on a recording instrument. (A Moseley X-Y Recorder is used for this purpose.).

3.6 DETERMINATION OF THE VELOCITY DISTRIBUTIONS BY THE TIME-OF-FLIGHT METHOD

The time-of-flight detector provides a signal representing the instantaneous particle density at the detector as a function of the time of flight. The detector signal may be converted directly to a speed distribution as described by Hagena and Henkes⁽⁸⁾ and by Anderson and Fenn.⁽⁹⁾ The velocity distribution function $f(\vec{v})$ in the free expansion defined as the number of particles per unit volume of physical space and per unit volume of velocity space, is usually assumed to be an isotropic Boltzmann distribution, corresponding to the kinetic temperature T_e at the skimmer entrance, which is superimposed on the streaming velocity v_o at the skimmer entrance. It is well known, however, that departures from equilibrium can and do occur in the nozzle expansion process; and, as a result, the velocity distribution function is not an isotropic Boltzmann distribution. Neglecting the effects of nonequilibrium, the jet velocity distribution function is given by

$$f(\vec{v}) = A \cdot \exp \left[-\beta (\vec{v} - \vec{v}_o)^2 \right]$$

For particles on the molecular beam axis, where \vec{v} is parallel to \vec{v}_o , this yields a speed distribution of

$$f(v) = A' \cdot v^2 \cdot \exp \left[-\beta (v - v_o)^2 \right]$$

and a differential intensity of

$$dI(v)/dv \equiv g(v) = v \cdot f(v) = A' v^3 \exp \left[-\beta (v - v_o)^2 \right]$$

where v_o is the streaming, or flow velocity, A , A' are constants and

$$\beta = \frac{m}{2 k T_e}$$

m = mass of gas molecule (all of which are assumed to be identical)

k = Boltzmann constant

T_e = flow temperature of the gas

In the ideal case of an infinitely short open time of the shutter, the signal $S_o(t)$ of a density-sensitive detector, positioned at a distance L downstream from the shutter, can be correlated to the differential intensity $g(v)$ as shown in Reference (10).

$$S_o(t) \propto (L/t) \cdot g(L/t) = A' \cdot (L/t)^4 \cdot \exp \left[-\beta \left(\frac{L}{t} - v_o \right)^2 \right]$$

or

$$S_o(t) \propto t^{-4} \cdot \exp \left[-B \left(\frac{1}{t} - \frac{1}{t_o} \right)^2 \right]$$

where $v_o = L/t_o$, $B = \beta L^2$.

For these experiments, the skimmer radius is considerably larger than the critical value, r_s^* . Accounting for this actual divergence of the flow field at the skimmer results in a modification of the speed distribution (reference 2) causing the final form of the time variation of the detector signal to be given by

$$S_o(t) \propto t^{-3} \exp \left[-B \left(\frac{1}{t} - \frac{1}{t_o} \right)^2 \right]$$

For analysis of a given molecular beam signal, with the detector on the beam centerline, v_o and T_e can be related to the time t_1 , t_m , and t_2 , $t_1 < t_m < t_2$, at which the density $n(t)$ has reached its half-maximum, maximum, and half-maximum values, respectively. As shown in (8), one obtains

$$v_o = (L/t_m) \cdot h(a)$$

$$T_e = (mL^2 / 2k) \cdot t_m^{-2} \cdot g(a)$$

where

$$a = \frac{t_m}{t_1} \quad \text{or} \quad \frac{t_m}{t_2}$$

$$h(a) = 1 - (3/2)g(a)$$

$$g(a) = \frac{(a-1)^2}{\ln 2 + 3(\ln a - a + 1)}$$

Thus, the flow velocity and temperature can be determined by observing the flight times corresponding to half-maximum and maximum detector signal. Since the two half maximum signal times t_1 and t_2 are interchangeable in the above expressions, each observation gives two results for T_e and v_o . Hence, a check on the accuracy of the data evaluation method is available.

3.7 EFFECT OF FINITE SHUTTER FUNCTION

The above analysis is based on three major assumptions; namely, (i) Maxwell-Boltzmann velocity distribution functions can be used for describing an aerodynamic molecular beam in spite of the lack of equilibrium caused by the existence of spatial gradients during the expansion process; (ii) the shutter open time is negligible compared to the half-width time interval of the measured TOF signal, and (iii) no limitation of resolving power exists due to the finite ratio of the length of the ionization zone in the beam direction to the length of flight path.

The first assumption has been made by several authors, (2), (8) and (9). For the present, consider this assumption to represent a first approximation to the true state of affairs. The third assumption is connected with the design aspects of the detector and has been discussed previously (Section 3.2) in this connection. For the detector described here, the ratio of the ionization zone length to the flight path length is of the order of 4×10^{-3} .

Hence, the effects of ionization zone length are insignificant. The effect of the finite shutter function (second assumption) has been studied in detail. The expected detector signal for various speed ratios and shutter function half-widths has been computed by the use of the convolution integral technique. The details of the calculation are presented in Appendix C, while the results are discussed in the next Section.

SECTION IV

DESIGN AND DESCRIPTION OF THE BEAM MODULATING SYSTEM

The detector signal $S_o(t)$ for an infinitely narrow shutter function half-width has been shown to be (see Section 3.6)

$$S_o(t) = \frac{A''}{t^3} e \left[-B \left(\frac{1}{t} - \frac{1}{t_o} \right)^2 \right]$$

In order to provide for maximum beam signal, the shutter function half-width time should be as large as possible, consistent with the desired speed resolution. The design of an optimum beam modulating system requires the consideration of the influence of this time-width of the shutter function on the measured detector signal.

4.1 SHUTTER FUNCTION

Let I_o be the molecular beam flux (particles/sec) reaching the detector without beam modulation. If $I(t)$ is the instantaneous fraction of I_o passing through the beam modulator (chopper disc), then the shutter function $g(t)$ is defined as

$$g(t) = \frac{I(t)}{I_o}$$

Assume that the flux density is constant over the effective beam cross-section Q at the chopper disc and that the detector sensitivity is constant over the detector cross section. For convenience, let $Q = l_t \times l_r$ where l_r and l_t are the lengths measured in the radial and tangential directions respectively with respect to the chopper disc. Further, let the slit have the dimensions $s_r \times s_t$ with $s_r > l_r$. The thickness of the slit is assumed

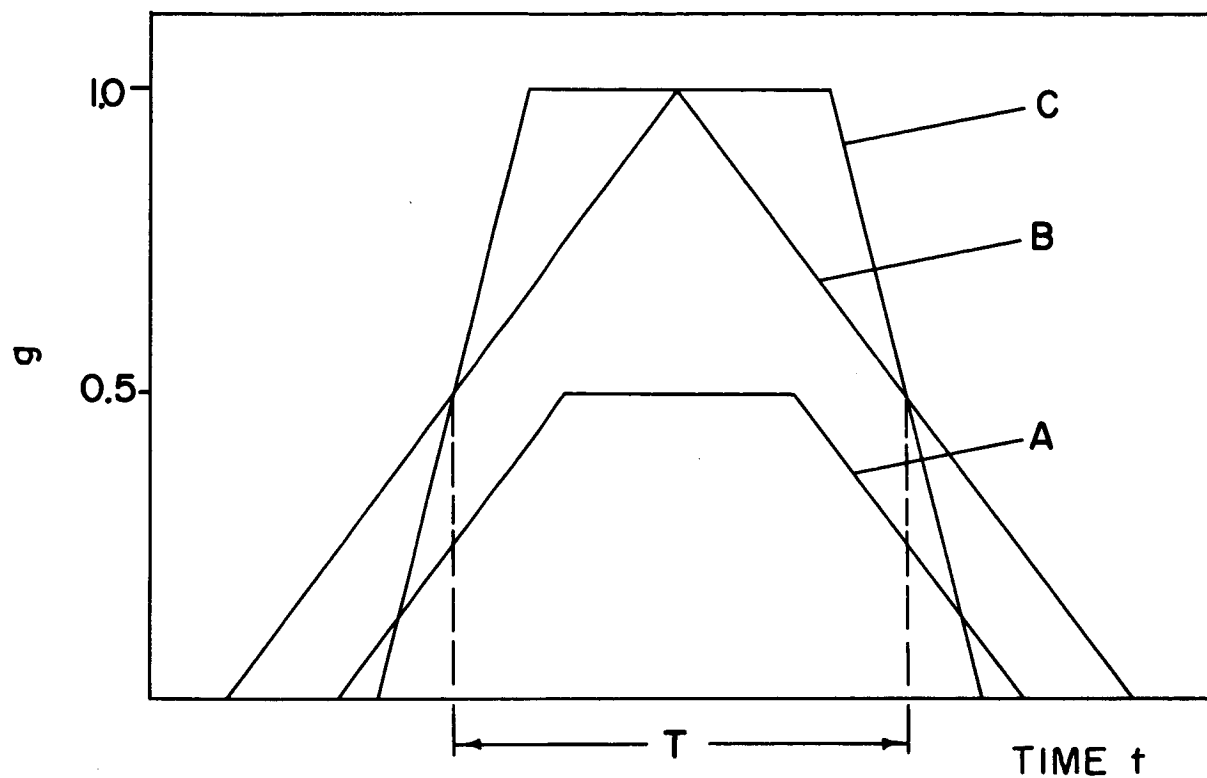
to be negligible compared to s_t and s_r . With these simplifying assumptions, $g(t)$ depends only on l_t , s_t and on the peripheral speed c of the disc. Figure (4.1.1) is a schematic representation of typical shutter functions with the same half-width T . The "best" shutter function; i. e., the one which provides minimum signal distortion for a given T is the rectangular function. However, for $s_r < l_t$ this advantage is offset by the smaller number of transmitted particles, given by the area under $g(t)$. For $s_t > l_t$, on the other hand, the motor speed must be substantially higher (of the order of $\frac{s_t}{T}$), than for the case where $s_t < l_t$. In many cases, the maximum motor speed is a limiting factor, and the best compromise between intensity and resolution is to choose $s_t = l_t$, which results in a triangular shutter function.

Appendix C gives the solution for the detector signal $S(t)$ for a nozzle-type molecular beam with the given speed distribution, as a function of the half-width T of the (triangular) shutter function. The results of these calculations will be used to arrive at a general criterion for the speed resolution of a given time-of-flight experiment. The numerical calculations were performed on a Burroughs B-5500 digital computer, and the results are discussed in Section 4.4.

4.2 DESIGN OF A TIME-OF-FLIGHT EXPERIMENT

While each experiment will have its own design problems, depending in part on the objective of the experiment, several design criteria are applicable to all time-of-flight experiments.

Molecular Beam. In these experiments, where the detector is usually much larger than the beam source, the effective beam cross section Q is



Shutter Function	Slit Width S_t	Beam Width l_t	Motor Speed C
A	0.5	1	l_t/T
B	1	1	l_t/T
C	3	1	S_t/T

FIG. 4.1.1. SHUTTER FUNCTIONS

determined by the size of the detector entrance aperture. In reflected beam studies, on the other hand, the beam width at the chopper is determined primarily by the effective target area.

Chopper Disc. For a fixed beam width l_t , the slit width and peripheral speed of the chopper are determined by the requirement, $s_t = l_t$, and by the required half-width of the shutter function $\frac{s_t}{c}$, for a particular experiment. The independent variables are the angular speed and diameter of the chopper disc.

For low signal levels, where signal averaging processes are necessary to extract the detector signal $S(t)$ from the noise, a high sampling rate; i. e., a small chopping period T_c , is of advantage. However, T_c must be long enough to avoid any appreciable overlap of successive signals. For an oven beam signal with $T_c = 3\beta L$, then $S(t + T_c)$ is always less than 2% of the maximum signal. A more general criterion is $T_c > 5 \Delta t$, where Δt is the half-width of the signal, which will result in a sufficiently small overlap for most types of beam speed distributions.

For a resolution $\frac{\Delta t}{T}$ of 5, the condition $\frac{T_c}{\Delta t} > 5$ requires that $\frac{T_c}{T} > 25$. Furthermore, for a chopper disc with n slits and radius r_c

$$\frac{T_c}{T} = \frac{2 \pi r}{n s_t}$$

For a typical value of s_t of 0.5 cm,

$$\begin{aligned} \frac{r}{n} &= \frac{s_t}{2 \pi} \cdot \frac{T_c}{T} \\ &\approx \frac{0.5}{2 \pi} \cdot 25 \text{ cm} \\ &\approx 2 \text{ cm} \end{aligned}$$

The selection of chopper disc radius and angular speed, to provide the required peripheral speed, is determined by practical considerations of apparatus size, drive system characteristics, and bearing lifetime.

Chopper - Detector Distance L. The optimum chopper-detector distance L depends on the effect of L on the time scale of the experiment, on the required angular and speed resolution and on the signal-to-noise ratio. For a given resolution $\frac{\Delta t}{T}$, the peripheral speed required is directly proportional to $\frac{1}{L}$. This criterion imposes a lower limit on the flight path length L, since the peripheral speed of the disc cannot exceed a maximum value which is fixed by the strength of the disc material. (For effusive beams of argon at room temperature with $s_t = 0.5$ cm and resolution $R = 5$, the minimum value of L is 3.4 cm based on a maximum peripheral speed of the chopper disc of 4×10^4 cm/sec.)

Good axial speed resolution sets another lower limit for the flight path length L. If the "active zone" of the detector extends over a distance

δL , the time required to pass through this zone must be small compared to the half-width of the shutter function T. Otherwise the detector signal will be influenced in a manner similar to that caused by the finite shutter function discussed previously. Under the arbitrary, but reasonable, condition that this time should be less than $0.2 T$, the following relationship between $\delta L/L$ and the resolution R is obtained; viz.,

$$\frac{\delta L}{L} = 0.2 \cdot \frac{T}{t_m} = \frac{0.2}{R} \cdot \frac{\Delta t}{t_m}$$

Hence, for an effusive beam (where $\frac{\Delta t}{t_m}$ is of the order unity), with $\delta L = 1$ mm and $R = 5$, L should be > 2.5 cm. For a nozzle beam, on the

other hand, where $\frac{\Delta t}{t_m} = 0.1$ (corresponding to a speed ratio of about 15), L should be > 25 cm.

The variation of signal-to-noise ratio with L depends on the type of detection system. For simplicity assume that the beam density at the detector is inversely proportional to L^2 and that the detector ion current due to the beam and background gas is proportional to the detector entrance area A . The latter assumption is necessary to evaluate the effects of variation of the detector size. The former assumption is valid if the nozzle-chopper distance is small compared to L and if the chopper parameters are changed, together with L , so as to maintain a constant resolution R . Finally, assume that the noise N is dominated either by the noise component N_{bg} of the background ion current or by the Johnson noise N_{R_L} of the input resistor R_L of the first amplifier stage.

With the above assumptions, the signal ion current $i^+ \propto \frac{A}{L^2}$, the background ion current $i_{bkg}^+ \propto A$, bandwidth of the amplifier $\Delta f \propto \frac{1}{L}$, chopping period $T_c \propto L$. Then for a constant area A ,

$$\begin{aligned} \text{signal } S &\propto AL^{-2} \times R_L \\ N_{bkg} &\propto (i_{bkg}^+ \times \Delta f)^{1/2} \times R_L \end{aligned}$$

$$\begin{aligned} &\propto \sqrt{\frac{A}{L}} \times R_L \\ N_{R_L} &\propto \sqrt{\Delta f \times R_L} \end{aligned}$$

$$\propto \sqrt{\frac{R_L}{L}}$$

For $R_L \propto L$, N_{R_L} is a constant.

$$\frac{S}{N_{\text{bkg}}} \propto A^{1/2} L^{-3/2}$$

$$\frac{S}{N_{R_L}} \propto \frac{A}{L}$$

These results do not consider the use of a signal averaging device and suggest a small value of the flight path length L .

If the detector size is varied with L so as to maintain $\frac{A}{L^2}$ constant (corresponding to a fixed solid angle subtended by the detector) one gets

$$S \propto R_L$$

$$N_{\text{bkg}} \propto L^{1/2} R_L$$

$$N_{R_L} \text{ is still constant}$$

$$\frac{S}{N_{\text{bkg}}} \propto \frac{1}{L^{1/2}}$$

$$\frac{S}{N_{R_L}} \propto R_L \propto L$$

The last result seems to favor a large L . However, with increasing L it becomes extremely difficult to design a detector, the output of which (for a given density), is proportional to the entrance aperture. Furthermore, the assumption that $N_{\text{bkg}} \ll N_{R_L}$ becomes increasingly less valid as A is increased proportional to L^2 . Therefore, for all practical purposes the distance L should be kept as small as possible and A should be as large as possible, consistent with the requirements of speed and angular resolution.

The use of signal averaging devices to increase S/N imposes another practical limitation on L . Since typical averaging instruments have minimum channel width (time resolution) of 1 μ sec or greater, L must be sufficiently large so that Δt is large compared to the channel width. On the other hand, small values of L result in increased repetition rate of the signal and, consequently improved signal-to-noise ratio for a given period of time.

Clearly, the design of an optimum beam modulation system involves the consideration of a number of conflicting requirements. Consequently, any solution represents a compromise based on the particular requirements imposed by the beam experiments which are to be performed.

The design calculations for the beam modulation system are presented in Appendix D. The results of these calculations show that satisfactory resolution of molecular beams with speed ratios up to 20 is possible with the present time-of-flight system.

4.3 DESCRIPTION OF THE SYSTEM

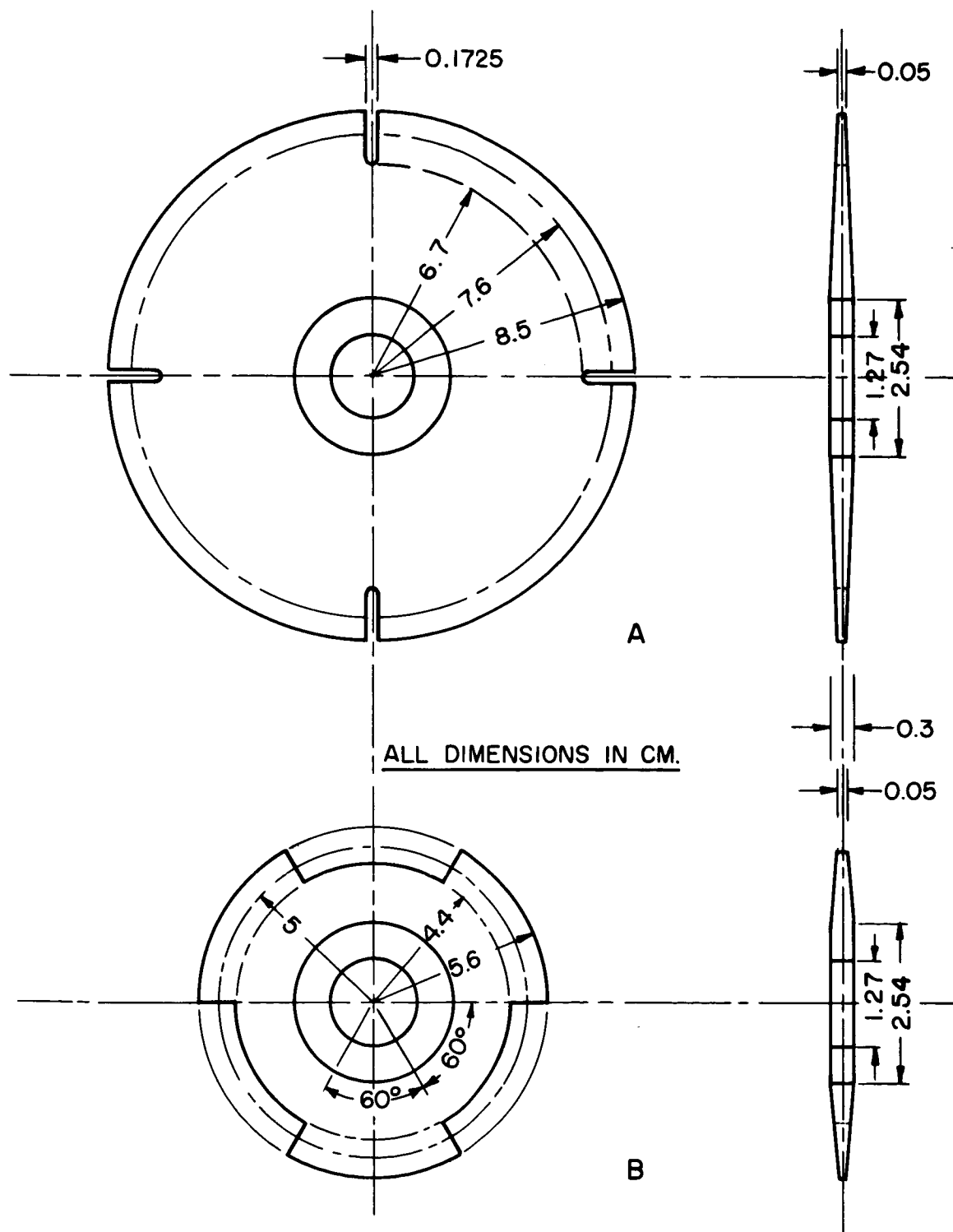
The rotating disc has a nominal diameter of 15.25 cm and thickness varying from 0.5 mm at the edge to 3.25 mm at the hub. It has four narrow slits, $s_r = 15$ mm and $s_t = 1.725$ mm, spaced equally on the periphery. The disc is driven directly by a two phase 30 W synchronous motor placed inside the vacuum chamber. (The maximum rotational speed recommended for continuous operation of the motor is 400 cycles/sec.) A modulating disc is also used to measure the total beam density. In this case, a disc of nominal diameter of 10 cm with three broad slits, each occupying 60° of the periphery, is used at very low rotational speeds (≈ 50 cycles/sec). As a result, a shutter function width $T \gg \Delta t_0$

is produced, and the peak density of the modulated beam approaches very nearly the density of the uninterrupted beam. The discs used for beam speed distribution and total beam density measurements are shown in Figure (4.3.1).

The signal required to trigger the oscilloscope and to trigger the signal integrating device, in such a manner as to insure that the signal waveform entering the integrator occurs at the same relative position each time, is provided by a light source - photo sensor arrangement which provides a signal synchronous with the beam pulse. This signal establishes the zero point of the time of flight. The chopper disc is positioned such that the center of the disc is at the same height as the beam axis and is offset from it in a horizontal plane by a distance equal to nominal radius of the disc. Consequently, as the beam pulse passes through a slit in the disc, a light beam is transmitted through the diametrically opposite slit and is allowed to fall on a photodiode. The photo - signal output of this diode is amplified by a Keithley Model 102B Decade Isolation Amplifier after which it serves as the trigger signal for the integrating device and for the oscilloscope. The photo - signal is displayed simultaneously on the oscilloscope, mixed with the detector signal.

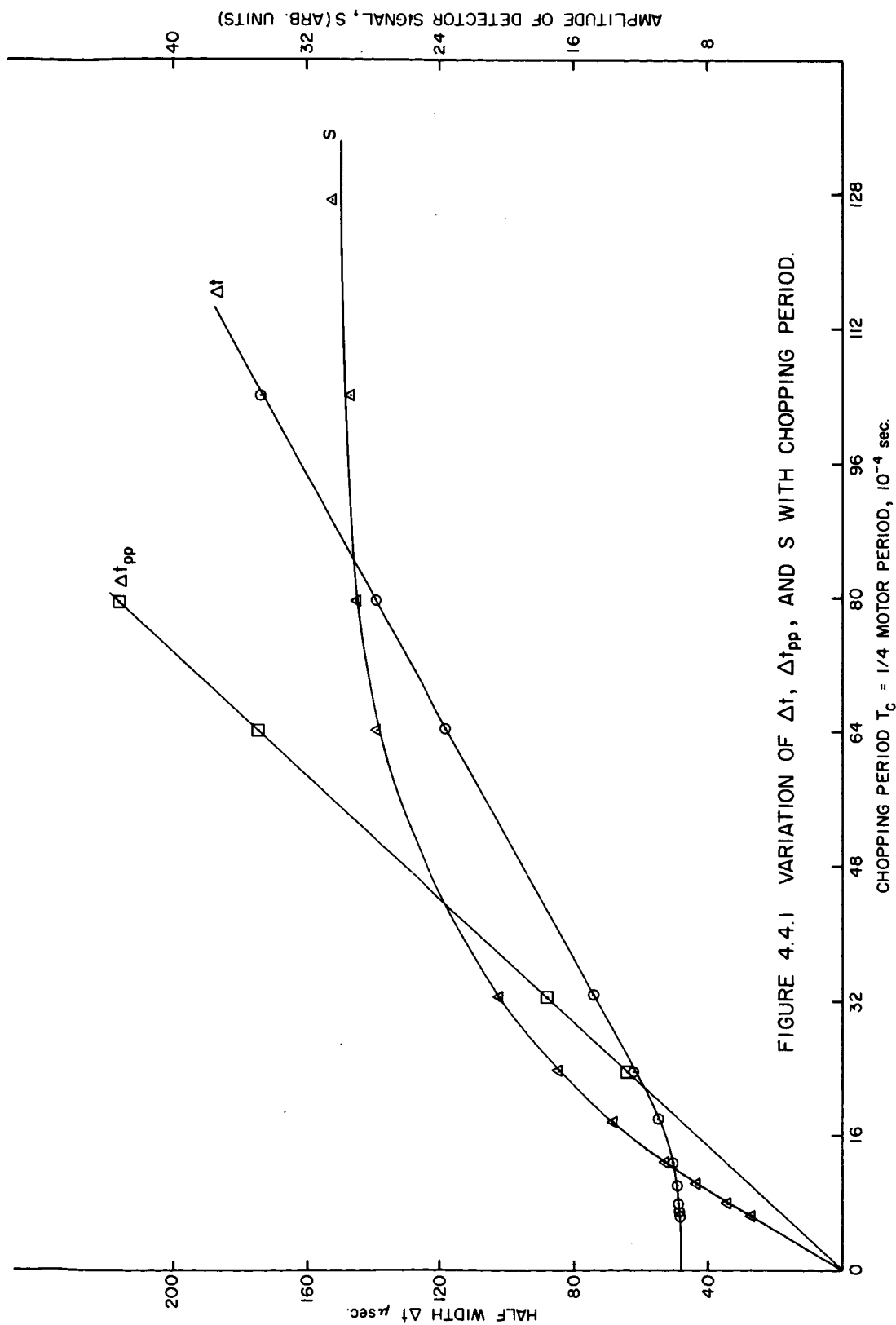
4.4 SYSTEM PERFORMANCE

The observed performance of the beam modulating system is shown in Figure (4.4.1) where peak signal amplitude S , half-width Δt of the detector signal and the half-width Δt_{pp} of the photo-signal are shown for constant beam source pressure and constant detector conditions as a function of the chopper period T_c . In the limiting case of infinite motor speed, the detector signal should be the ideal Maxwellian response; viz.,



A. HIGH RESOLUTION SPEED DISTRIBUTION MEASUREMENTS.
B. TOTAL PARTICLE-DENSITY MEASUREMENTS.

FIG. 4.3.1 CHOPPER DISCS

FIGURE 4.4.1 VARIATION OF Δt , Δt_{pp} , AND S WITH CHOPPING PERIOD.

$S_o(t) = \frac{A''}{t^3} e^{-B \left(\frac{1}{t} - \frac{1}{t_o} \right)^2}$ (see Section 3.6) with a half-width Δt_o corresponding to this function. However, in this limit of infinite motor speed, the detector signal is zero since no beam molecules can pass through the disc. As the motor speed is decreased, the half-width Δt of the detector signal $S(t)$ also increases. However, if the half-width of the shutter function T is small compared to the half-width Δt_o of $S_o(t)$, the half-width Δt of the final signal will increase only slowly with decreasing motor speed. On the other hand, the number of particles passing through the shutter will increase in inverse proportion to the motor speed. Consequently, when the motor speed becomes so small that the shutter function half-width is much larger than Δt_o , the half-width Δt will be directly proportional to T ; i. e., to motor period. (In this case, the beam can be treated as if it were monoenergetic since its velocity spread is relatively small.) The peak detector signal tends to reach an upper limit as the motor speed decreases so that one observes essentially the uninterrupted beam density.

The half-width time of the reference light pulse, Δt_{pp} , increases linearly with T_c and is for large values greater than Δt and, consequently, greater than T . This is explained by the fact that for these experiments the light beam is wider than the molecular beam.

The fractional deviation of the measured half-width Δt from the ideal half-width Δt_o , $\frac{\Delta t - \Delta t_o}{\Delta t_o}$, is plotted as a function of the resolution $R = \Delta t/T$ in Figure (4.4.2). The experimental results of Figure (4.4.1) are shown together with calculated values for nozzle beams with triangu-

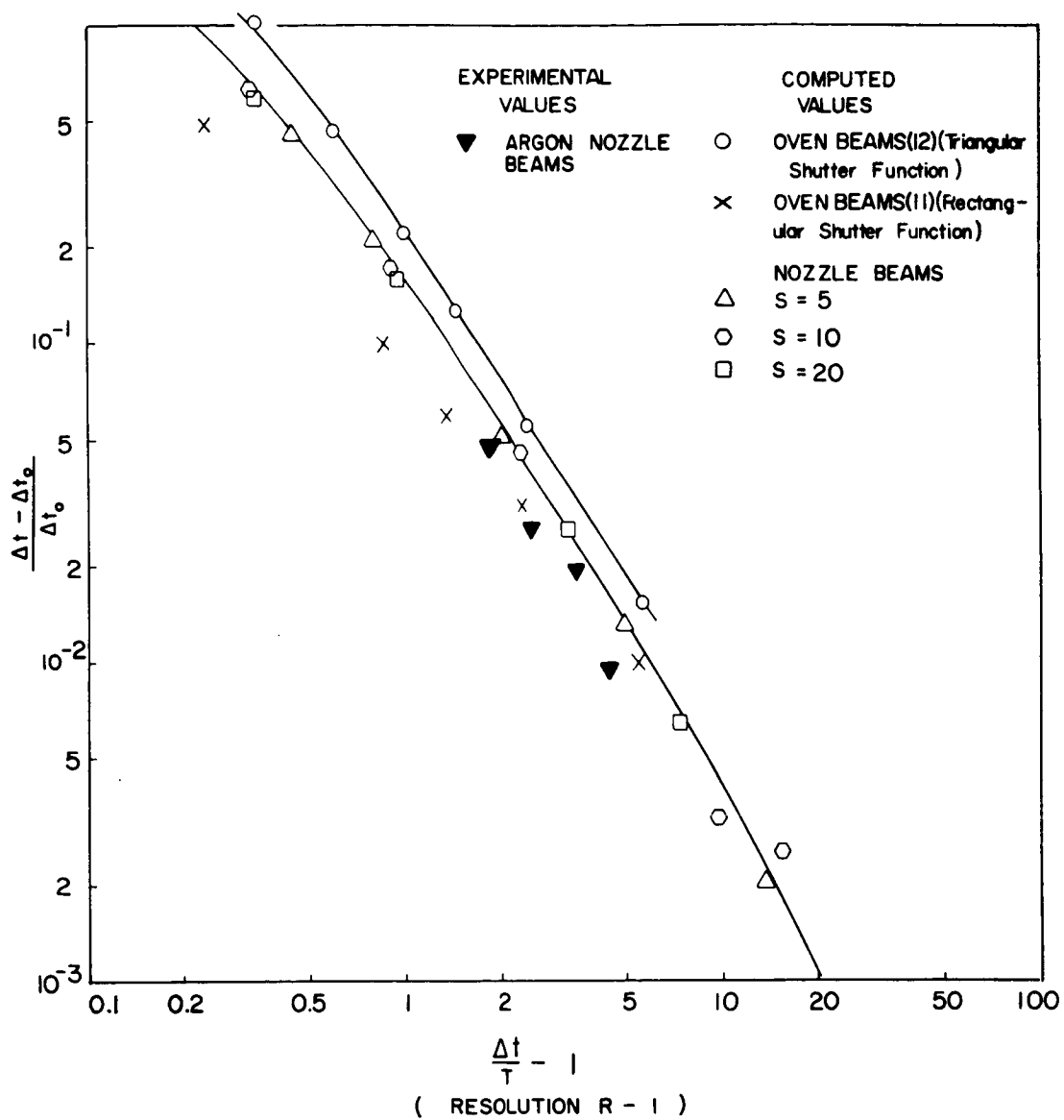


FIG. 4.4.2. RELATIVE CHANGE IN HALF WIDTH
vs RESOLUTION

lar shutter functions, obtained by solving the convolution integral. Also shown are the oven beam results obtained from earlier work by Hagena⁽¹¹⁾ and Paul Scott⁽¹²⁾. (A computer program using Scott's result was set up to evaluate Δt over a larger range of T than available in the referenced paper.) Comparison of the computed results for nozzle and oven beams shown in Figure (4.4.2) indicates that the relative change in half-width is less at a given R , the more symmetric $S_o(t)$ is; comparison at fixed R of the two computed results for oven beams with different shutter functions shows that a rectangular shutter function induces a smaller relative change than the triangular function. For nozzle beams, it might be expected that the resolution will improve for higher beam speed ratios. However, as shown in Figure (4.4.2), increasing the speed ratio from 5 to 20 makes no significant difference; it is practically independent of the speed ratio.

The experimental nozzle beam results plotted in Figure (4.4.2) show somewhat smaller relative change than the computed values. This is not surprising since the theoretical curve is based on a triangular shutter function while the actual beam shutter function (due to the circular beam cross-section) corresponds more to a rectangular shutter function. (See Figure D.1 in Appendix D.)

SECTION V

EXPERIMENTAL RESULTS

5.1 GEOMETRY OF THE BEAM SYSTEM

Nomenclature (See Figure 5.1.1)

X_{s_o}	=	minimum nozzle-skimmer separation distance
d	=	nozzle pull-out distance
X_s	=	$X_{s_o} + d$ = nozzle-skimmer separation distance
X_{co}	=	nozzle-collimator separation distance
X_t	=	distance between nozzle and target
X_{ch}	=	distance between nozzle and chopper disc
X_a	=	distance between nozzle and detector entrance aperture
X_d	=	distance between nozzle and active zone of detector

TABLE 5.1

Geometry	<u>Diameters, mm</u>		
	Nozzle	Skimmer	Collimator
A	0.06	1.0	1.5
B	0.06	2.0	1.5
C	0.06	1.0	2.5

TABLE 5.2

For geometry A

d	=	0 mm
$X_s = X_{s_o}$	=	4.77 mm
X_{co}	=	22.3 mm
X_t	=	85.9 mm
X_{ch}	=	136.7 mm
X_a	=	289.1 mm
X_d	=	390.8 mm

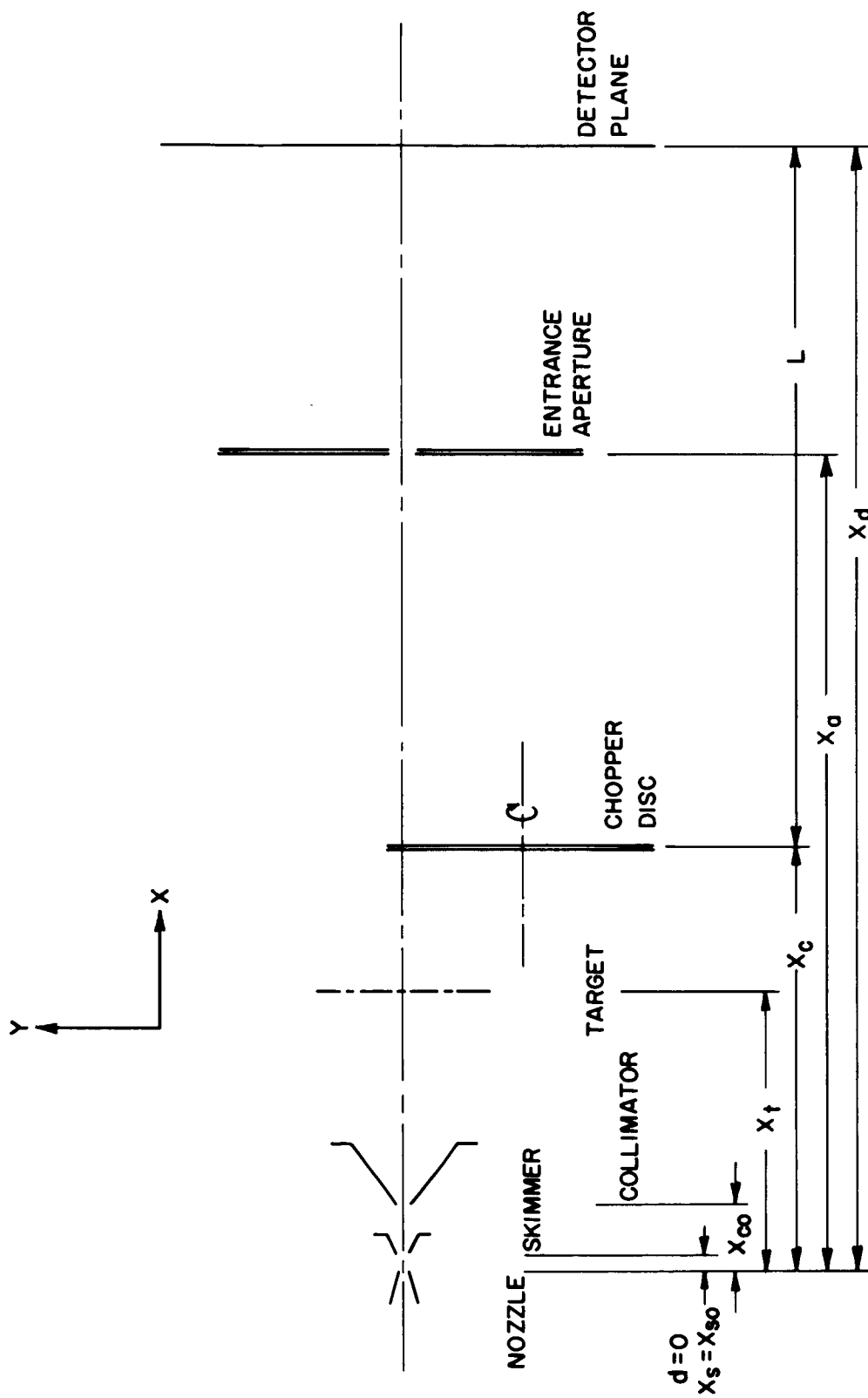
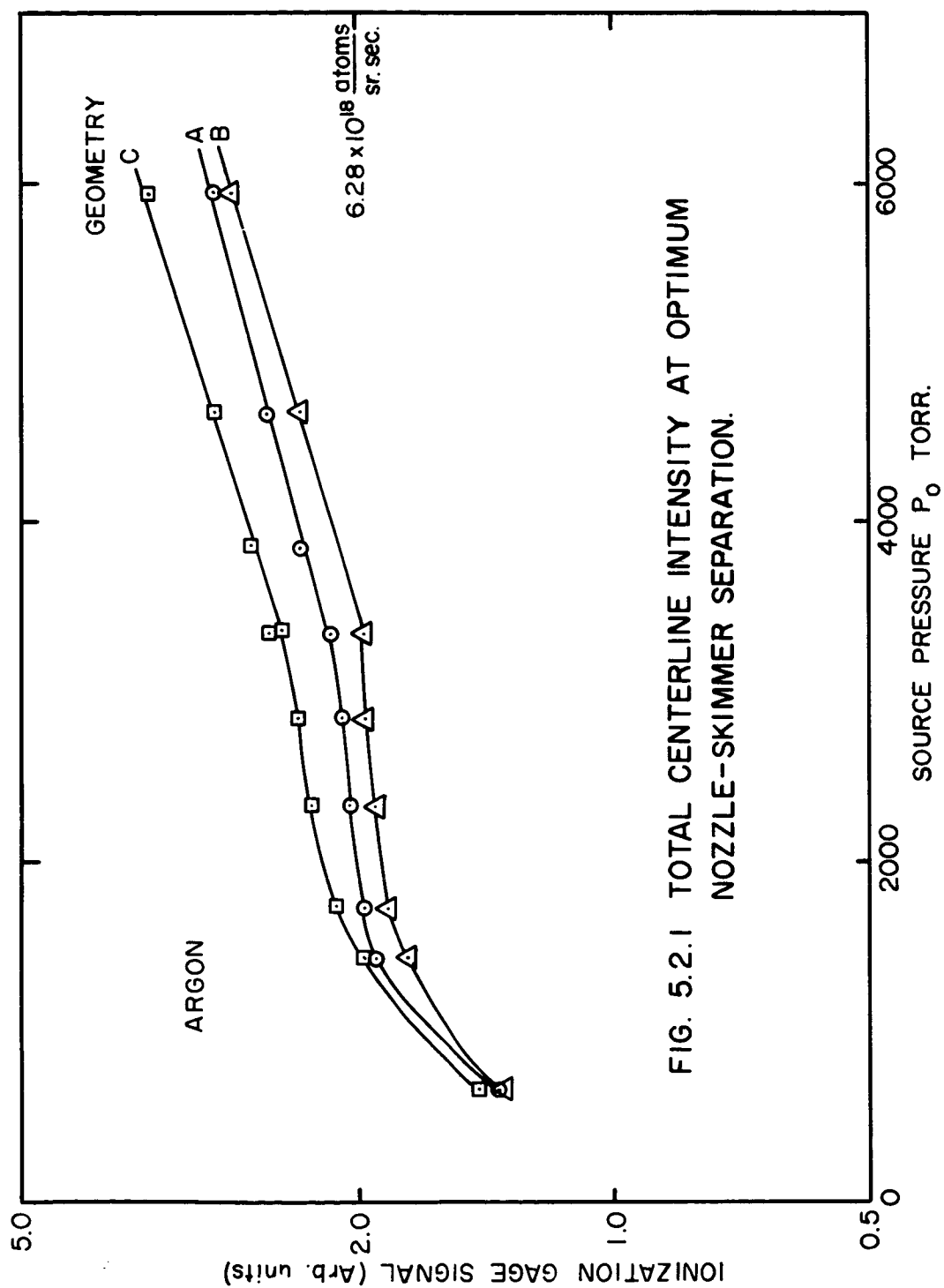


FIG. 5.1.1 BASIC GEOMETRY OF THE MOLECULAR BEAM.

5.2 TOTAL PARTICLE DENSITY MEASUREMENTS

The nozzle beam centerline intensity and beam profiles have been measured for argon, nitrogen and carbon dioxide. In some cases, comparative measurements have been made for different combinations of skimmer and collimator sizes. Initial total intensity measurements for argon and nitrogen were made with a flux-sensitive detector consisting of a G. E. ionization gage located inside chamber C₃. The gage was mounted on the rotary table, and the beam axis was established accurately by measuring a detailed beam profile. Later, total beam density measurements were made using the time-of-flight detector (see Section 4.4), with the motor driven at 50 cps for these measurements. Absolute values of beam particle density were obtained by comparing the detector signal for nozzle beams with that obtained for an ideal effusion beam produced by replacing the skimmer with a 1 mm diameter orifice and using the nozzle discharge chamber as the beam source chamber. Effusive beams with the skimmer as the source aperture were measured before each nozzle beam test as a reference; and, using an experimentally determined correlation between effusion beam density with skimmer and orifice sources, the detector signals for nozzle beams were converted to beam particles/cm³. The absolute beam particle density values obtained with the ionization gage (flux sensitive) detector and those obtained with the time-of-flight (density sensitive) detector agree within 20% for the same beam gas, source pressure, and beam system geometry.

The total particle density measurements on the beam centerline for argon are presented in Figures (5.2.1) and (5.2.2). The nozzle-skimmer



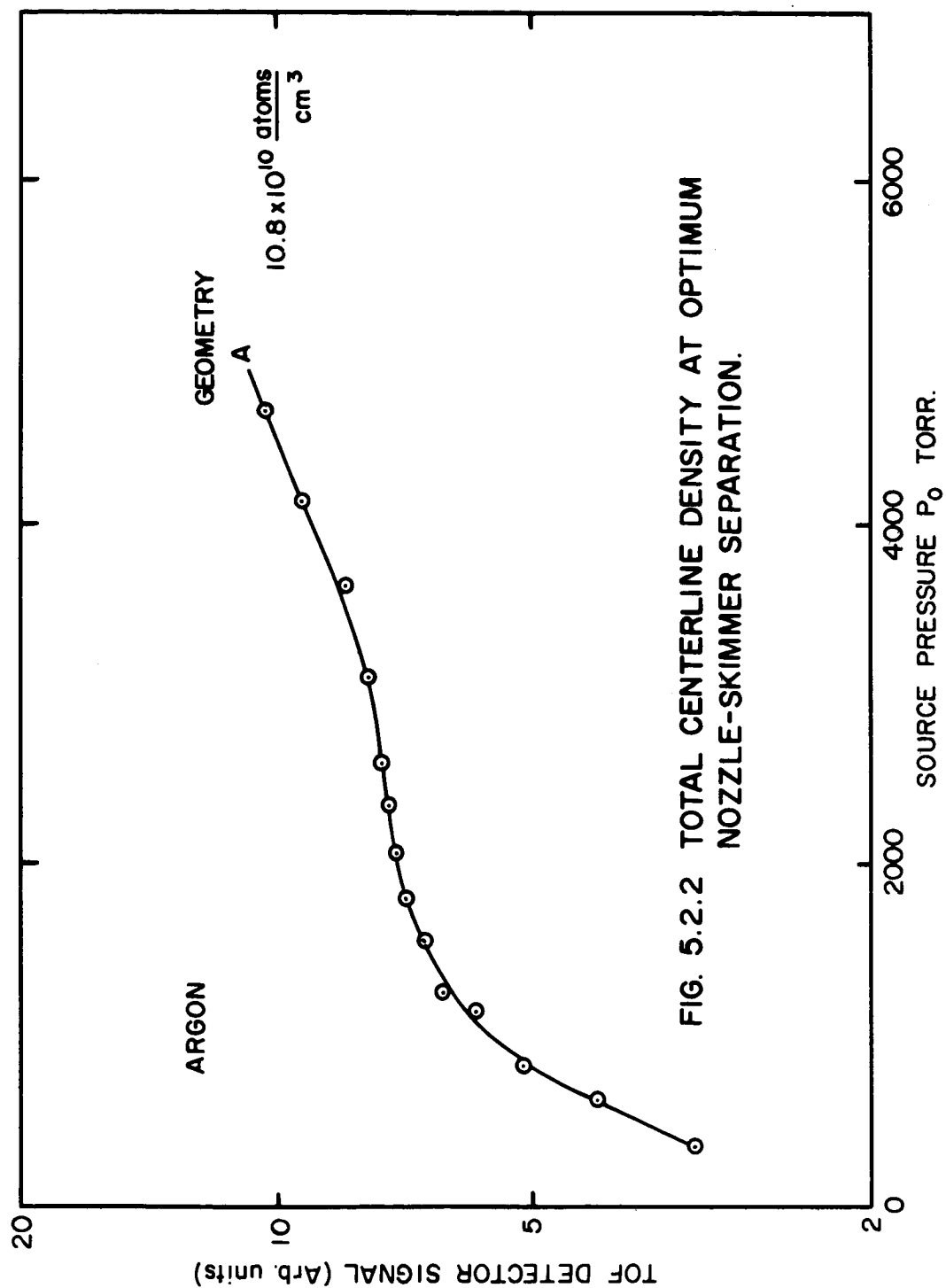


FIG. 5.2.2 TOTAL CENTERLINE DENSITY AT OPTIMUM
NOZZLE-SKIMMER SEPARATION.

separation distance X_s was maintained at its "optimum" distance, defined as that distance corresponding to the maximum detector signal for each source pressure. It is evident that the variation of beam density with source pressure obtained with the time-of-flight detector for geometry A follows the same trend as similar measurements made with the ionization gage detector for the same geometry. (The ionization gage results for geometries B and C indicate similar behavior.) The results of Figure (5.2.1) show that the beam intensity increases rapidly as the source pressure is raised from 0 to about 1400 torr. In the source pressure range from 1400 to 3500 torr, the rate of increase of total beam intensity with increasing source pressure is much smaller than at lower source pressures. At source pressures above 3500 torr, the intensity again increases rapidly with increasing source pressure. This behavior is caused by condensation occurring in the argon beam, a phenomenon which has been observed by previous investigators (4) and (8).

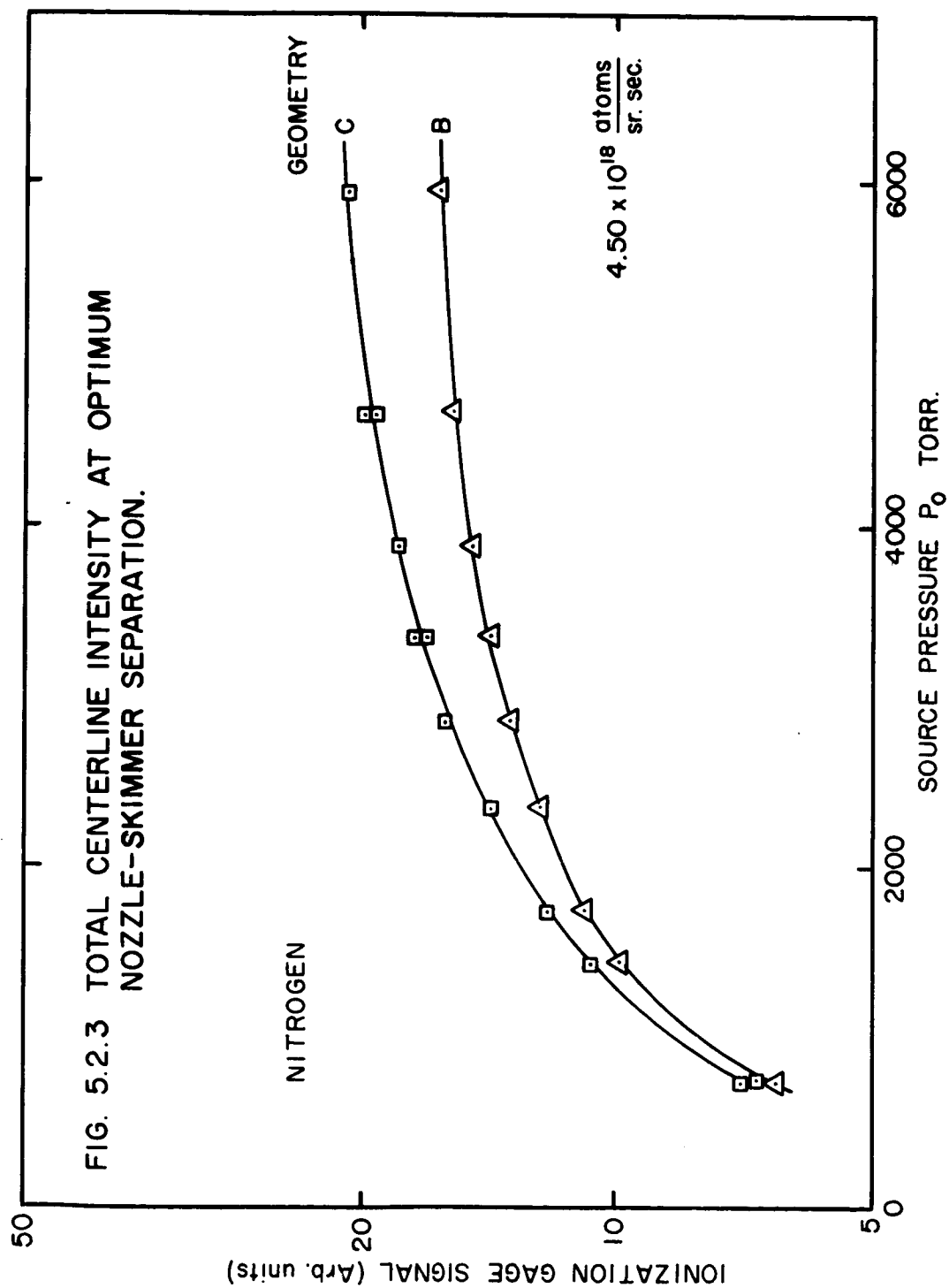
The results shown in Figure (5.2.1) for geometry C (larger (2.5 mm) collimator) do not show the very pronounced flattening and the subsequent sharp rise observed for geometries A and B. However, the abrupt change of slope at a source pressure of about 1500 torr, attributed to condensation, is evident. The use of a larger collimator results in somewhat larger beam intensity. This indicates the presence of collisional processes taking place downstream of the skimmer, which contribute particles to the detector on the beam axis since a larger collimator allows more of these scattered particles to augment the centerline intensity.

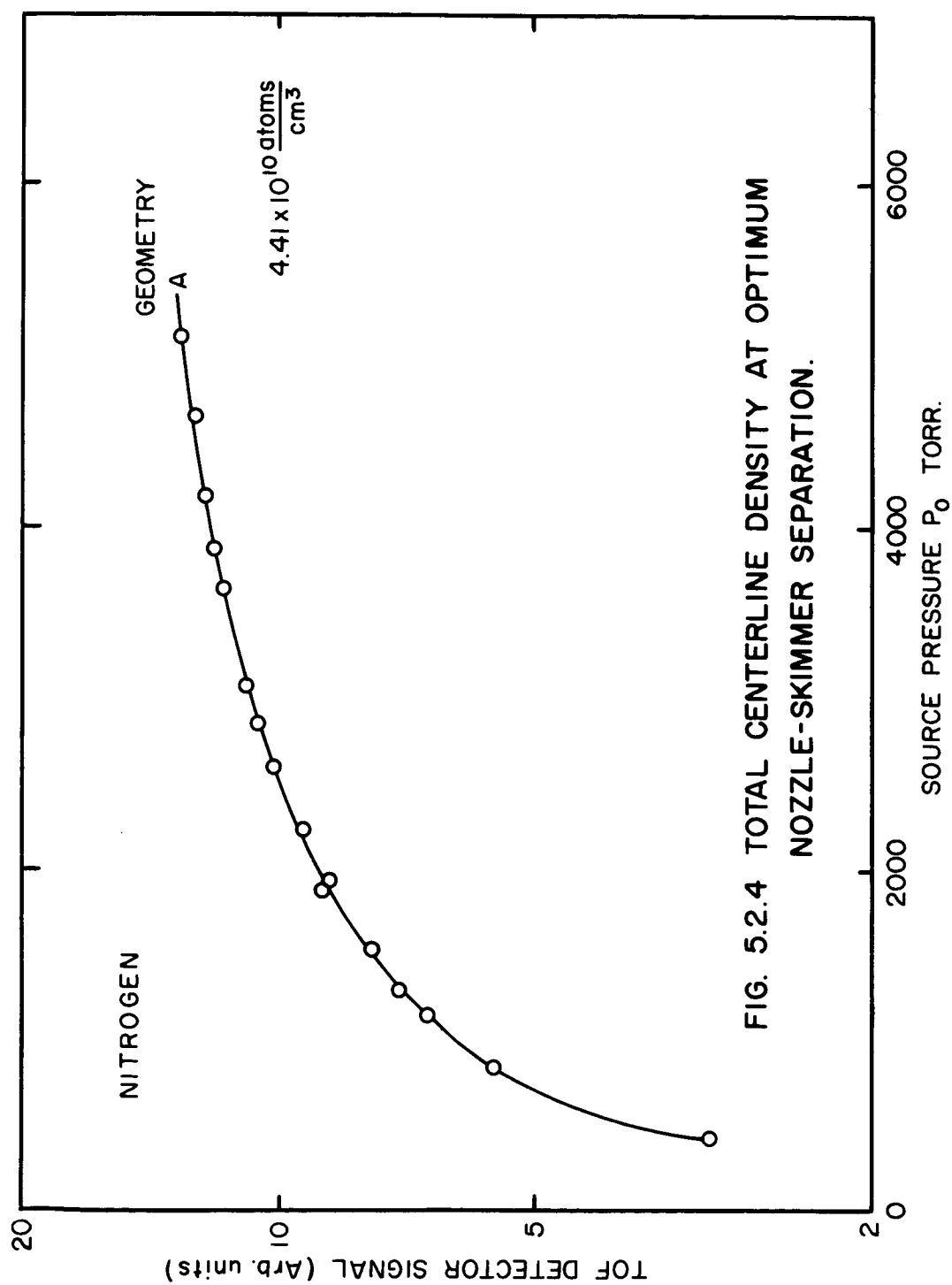
The larger skimmer (compare geometries A and B in Figure (5.2.1))

produces a somewhat smaller total beam intensity. The larger skimmer increases the gas load into the collimation chamber C_2 , which, assuming a constant pumping speed for S_2 , causes a correspondingly higher pressure in the collimation chamber. Consequently, increased beam attenuation due to collisions between beam particles and background gas results. In addition, the larger beam cross-section, resulting from increased skimmer size, increases the probability of collisions within the beam itself. Such collisions result in a decrease in beam intensity since even small angle scattering of beam molecules results in their loss from a highly collimated beam. (The beam is defined by the collimator for geometries A and B, while the skimmer is the beam defining orifice for the configuration C.) Finally, increased skimmer size reduces the skimmer Knudsen number and enhances skimmer interference resulting in broader beams of lower intensity.

Similar total intensity measurements made for nitrogen with both the flux sensitive- and density-sensitive detectors are shown in Figures (5.2.3) and (5.2.4). Since nitrogen does not show condensation effects in this range of source pressure, the centerline intensity increases uniformly with increasing source pressure. (The critical source pressure for condensation in nitrogen is nearly six times larger than the corresponding value for argon.) Nitrogen measurements were made for geometries B and C with the ionization gage and for geometry A with the time-of-flight detector.

Carbon dioxide total intensity measurements were made only with the density detector. It exhibited strong condensation effects similar to that





for argon. Centerline beam density was measured also for several fixed source pressures as a function of the nozzle-skimmer separation distance X_s over a range from about 5 to 30 mm, using the time-of-flight detector. The results for nitrogen at source pressures of 1400 and 2600 torr are presented in Figure (5.2.5). Similar results were obtained for argon and carbon dioxide.

The optimum nozzle-skimmer separation distance characterizes a certain value for the skimmer Knudsen number. For the data presented in Figure (5.2.5), the skimmer Knudsen number at optimum X_s is estimated to be about 2. At distances smaller than the optimum value, this Knudsen number is smaller. Therefore, scattering processes inside the skimmer cone will be enhanced, leading to larger beam attenuation. At nozzle-skimmer separation distances, larger than optimum, although this scattering may become less important, the intensity still falls uniformly due to increased background scattering in the nozzle discharge chamber. The intensity decrease at $X_s > X_{s_{opt}}$ due to scattering processes upstream of the skimmer has been discussed by Hagena and Schüller⁽¹³⁾ and by Fenn and Anderson⁽¹⁴⁾. Figure (5.2.5) shows that at large nozzle-skimmer separation distances, the beam density actually decreases with increasing source pressure. At high source pressures, the mass flux into the nozzle discharge chamber C_1 is proportionately larger, which, for a constant pumping speed of S_1 , increases the pressure in the chamber C_1 . Consequently, increased beam attenuation, due to beam scattering by the background gas in the nozzle discharge chamber, occurs at large source pressures.

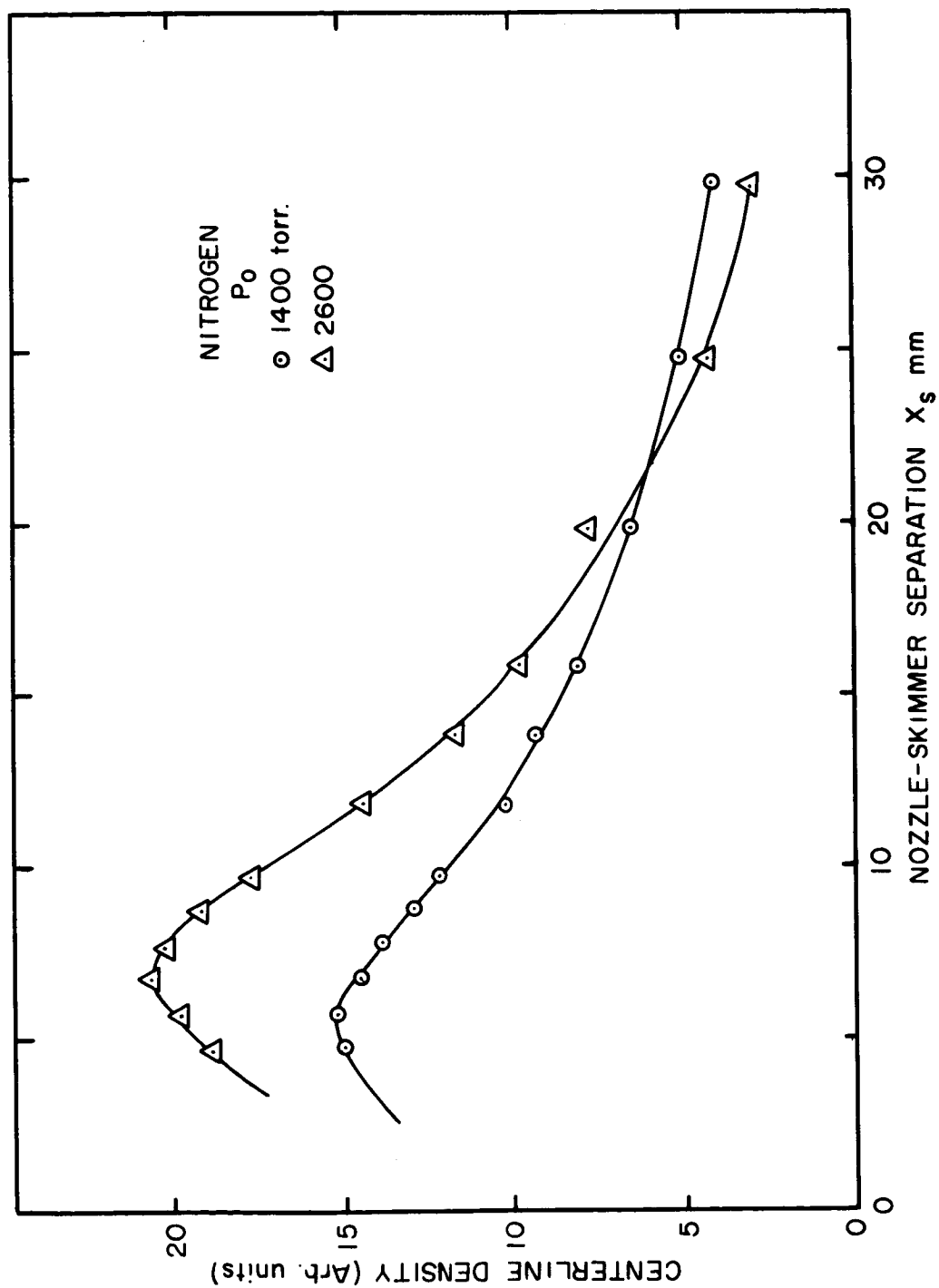


FIG. 5.2.5 CENTERLINE PARTICLE DENSITY vs. NOZZLE-SKIMMER SEPARATION.

Beam Profile Measurements

Direct beam profiles have been measured for argon, nitrogen and carbon dioxide at various source pressures and nozzle-skimmer separation distances. Except for some early ionization gage measurements, all measurements were made with the time-of-flight detector. Again, except for some early measurements, beam geometry A (1 mm skimmer, 1.5 mm collimator) was used for most of the experiments. All data shown refer to geometry A. The diameter of the effective detector ionization zone; i. e., its resolution for all measurements, is 5 mm.

From the system geometry described in Section 5.1, the dimensions of the beam core and half-shadow regions, defined in Figure (5.2.8) are easily calculated and are tabulated below. (Recall that the core here is determined by the collimator size.)

TABLE 5.3

Core and Half-Shadow for Beam Geometry A

	X_s	CORE mm	HALF-SHADOW mm
1	4.77	+ 13.10 - 13.10	+ 27 - 27
2	6.77	+ 12.10 - 12.10	+ 27 - 27
3	7.00	+ 12.00 - 12.00	+ 27 - 27
4	8.77	+ 11.25 - 11.25	+ 27 - 27
5	9.77	+ 10.88 - 10.88	+ 27 - 27
6	14.77	+ 9.32 - 9.32	+ 27 - 27

Figure (5.2.6) shows a typical beam profile plotted, for clarity of exposition, in linear co-ordinates. Figure (5.2.7) shows beam profiles for nitrogen at source pressures of 1400 and 2575 torr, with the nozzle-

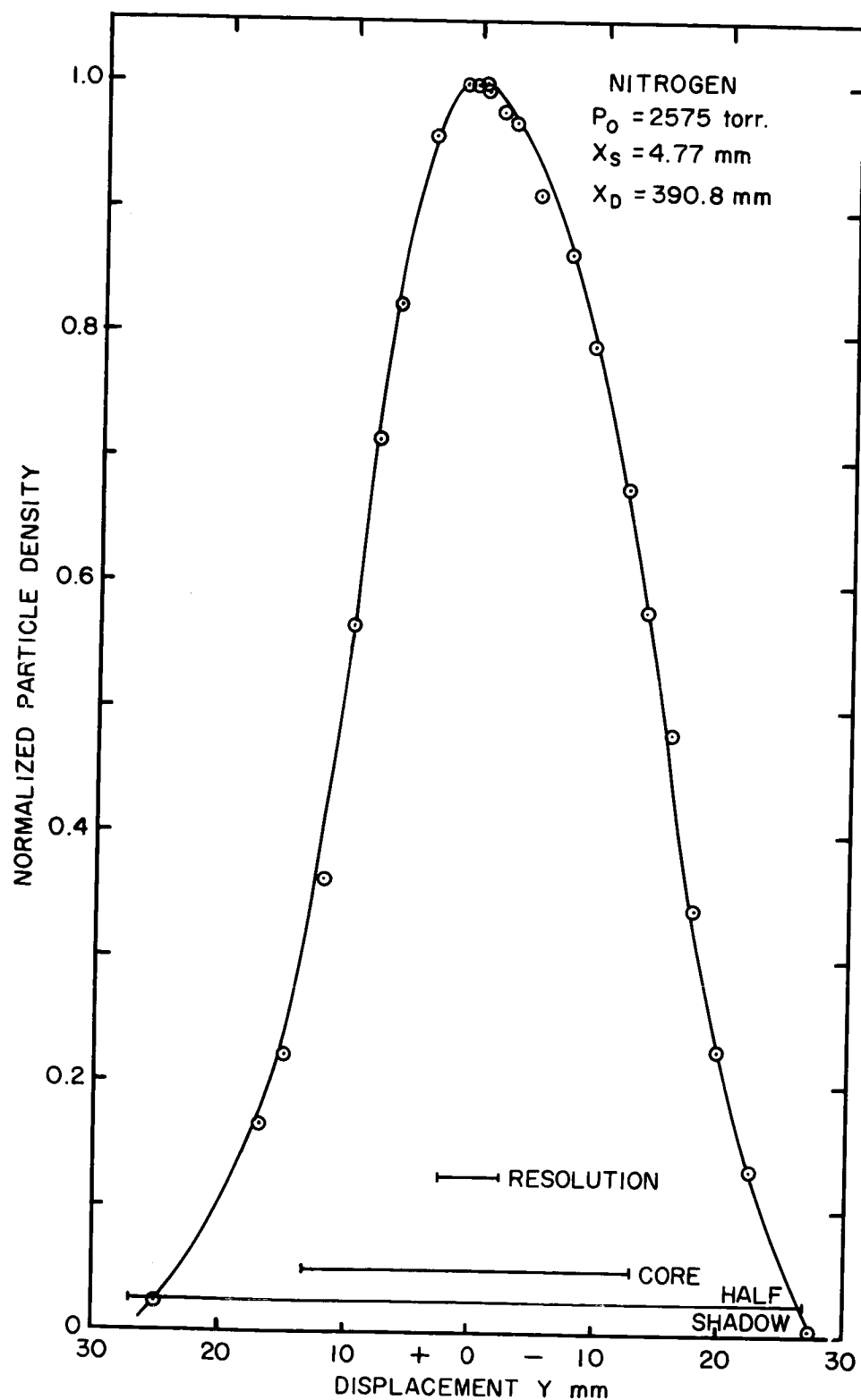


FIG. 5.2.6 TYPICAL BEAM PROFILE.

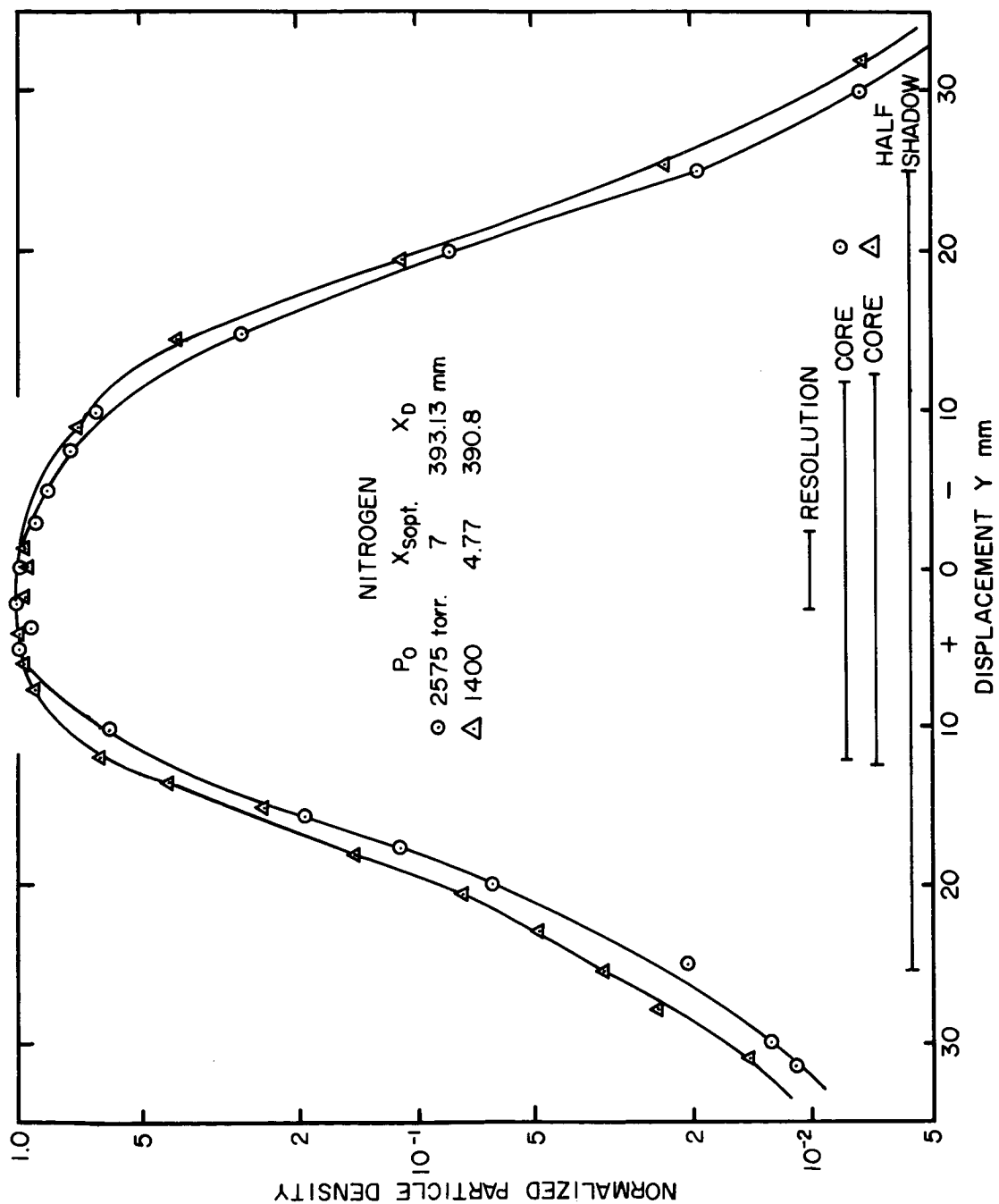


FIG. 5.2.7 BEAM DENSITY PROFILES vs. SOURCE PRESSURE.

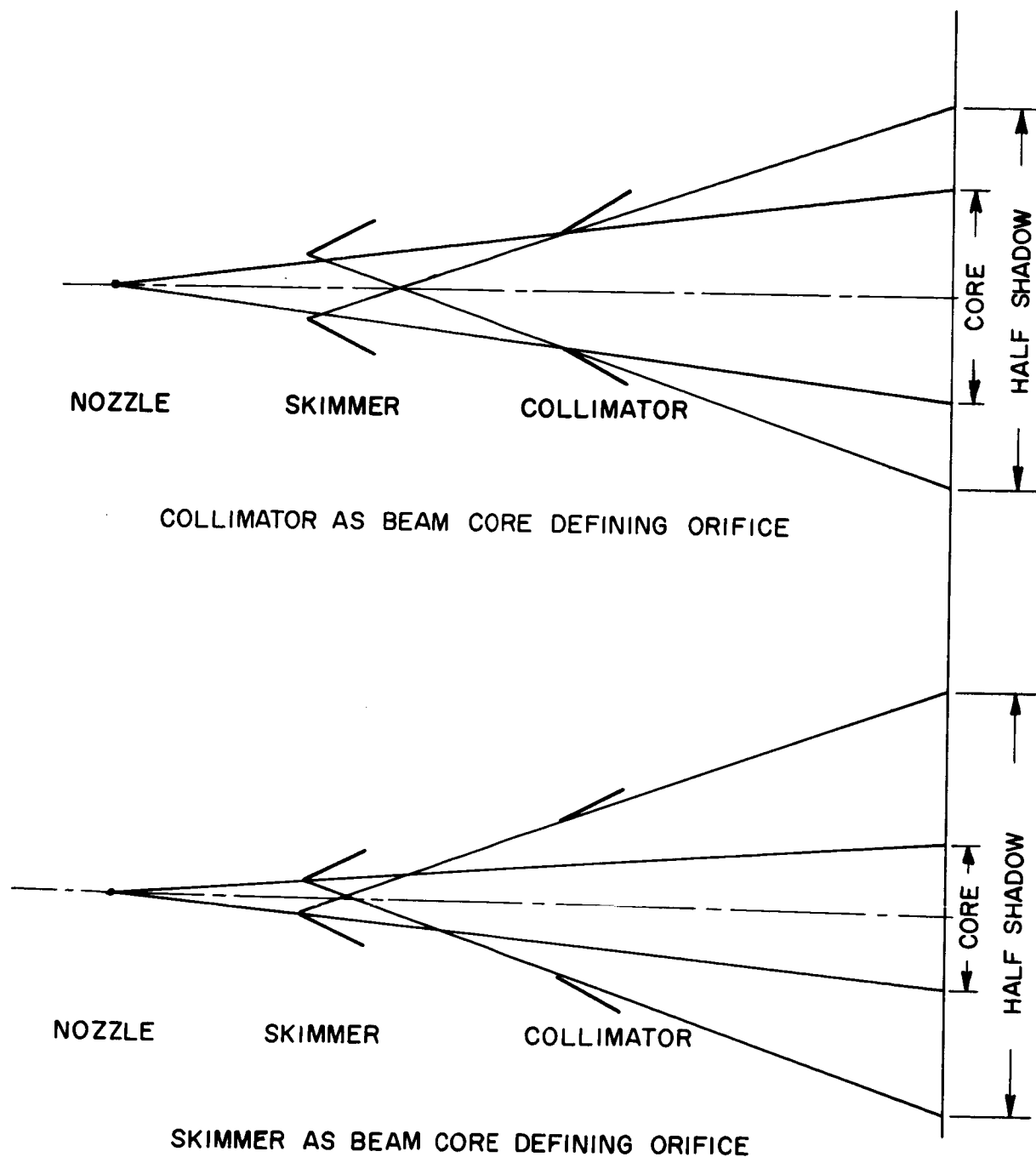


FIG. 5.2.8 DEFINITION OF BEAM CORE AND HALF SHADOW REGIONS.

skimmer separation at its optimum value in each case. To display the details of the profile in the outer portions of the beam, the data are plotted here in semi-log co-ordinates. It can be seen from Figure (5.2.7) that the beam profiles at optimum nozzle-skimmer separation distance differ only slightly from each other. The small decrease in the width of the profile for the higher source pressure should be primarily due to the increase in speed ratio (see Section 5.3). A high speed ratio causes a relative concentration of the particle flux in the core of the beam.

Contrary to expectations, the beam profile shows a slight asymmetry. Considerable effort was made to determine the cause of this asymmetry, and these results are discussed in detail in Section 5.4.

The effect of nozzle-skimmer separation distance on the beam profile is illustrated in Figure (5.2.9). At large nozzle-skimmer separation distances, the size of the beam core decreases slightly due to the geometrical factor. In addition, the particle density in the half-shadow region decreases because of the decreased density at the skimmer entrance and a correspondingly reduced scattering of beam particles into the outer regions of the beam. The profiles for the two larger nozzle-skimmer separation distances are nearly identical at small off-axis displacements. However, the beam density in the outer parts of the beam increases as the nozzle-skimmer separation distance is decreased.

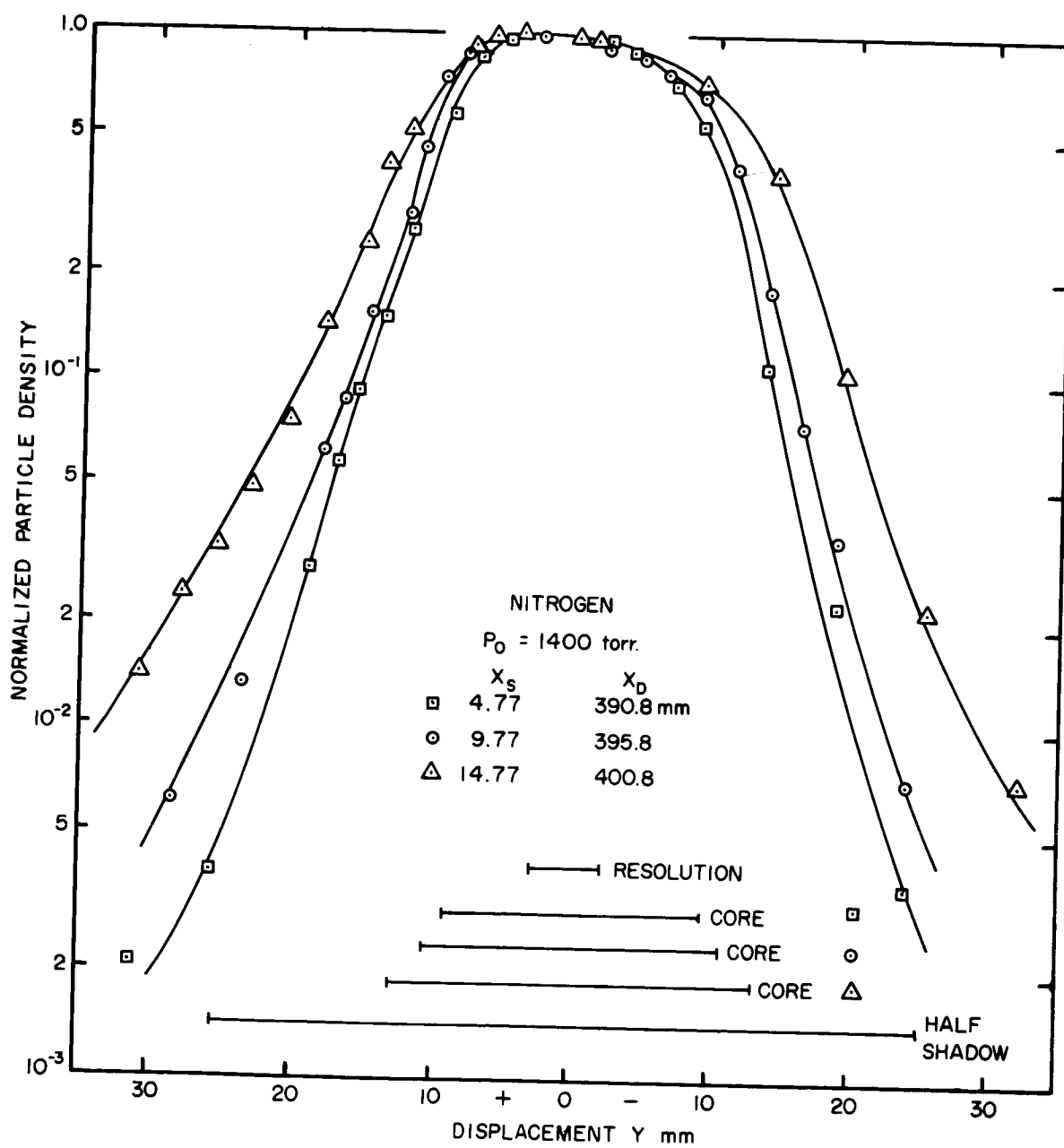


FIG. 5.2.9 BEAM DENSITY PROFILES vs. NOZZLE-SKIMMER SEPARATION.

5.3 SPEED DISTRIBUTION MEASUREMENTS

Speed distribution measurements for beams of argon and nitrogen have been made using the time-of-flight technique described in Section 4.

Influence of Source Pressure. The variation of speed ratio S with nozzle source pressure for argon and nitrogen at the optimum nozzle-skimmer separation distance is shown in Figures (5.3.1) and (5.3.2). The existence of an upper limit for the speed ratio due to partial condensation of argon beams at about 1400 torr is clearly demonstrated and correlates well with the total intensity data shown in Figures (5.2.1) and (5.2.2). For the case of nitrogen on the other hand, the speed ratio increases continuously with increasing source pressure in the range under consideration.

Variation of Speed Ratio with Nozzle-Skimmer Separation Distance. The variation of speed ratio on the beam axis with nozzle-skimmer separation distance is shown in Figures (5.3.3) and (5.3.4) for argon and nitrogen, respectively. The decrease in speed ratio at small nozzle-skimmer separation results from two principal reasons; viz., incomplete expansion and skimmer interaction. For nozzle-skimmer separation distances larger than a critical value, which depends on the source pressure, the speed ratio remains essentially constant, confirming the presence of translational freezing in freely expanding jets reported previously^{(2),(4),(8)}. The effect of condensation in the case of argon beams is seen again in Figure (5.3.3). The maximum speed ratio of 18.4 is obtained for a source pressure of approximately 1350 torr. The decrease in the speed ratio for argon at source pressures greater than 1350 torr is in good agreement

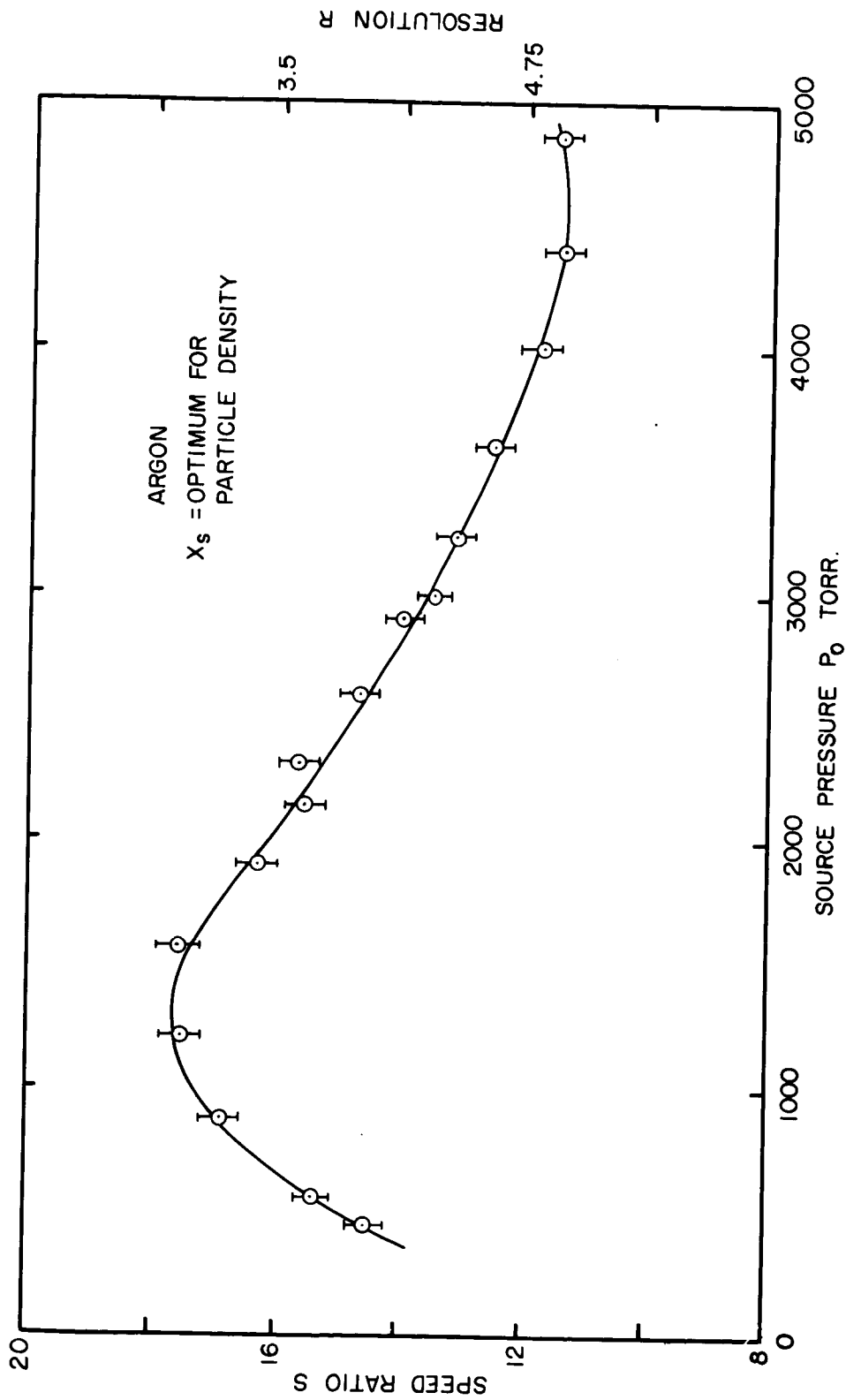


FIG. 5.3.1 SPEED DISTRIBUTION vs. SOURCE PRESSURE P_0 AT OPTIMUM NOZZLE-SKIMMER SEPARATION.

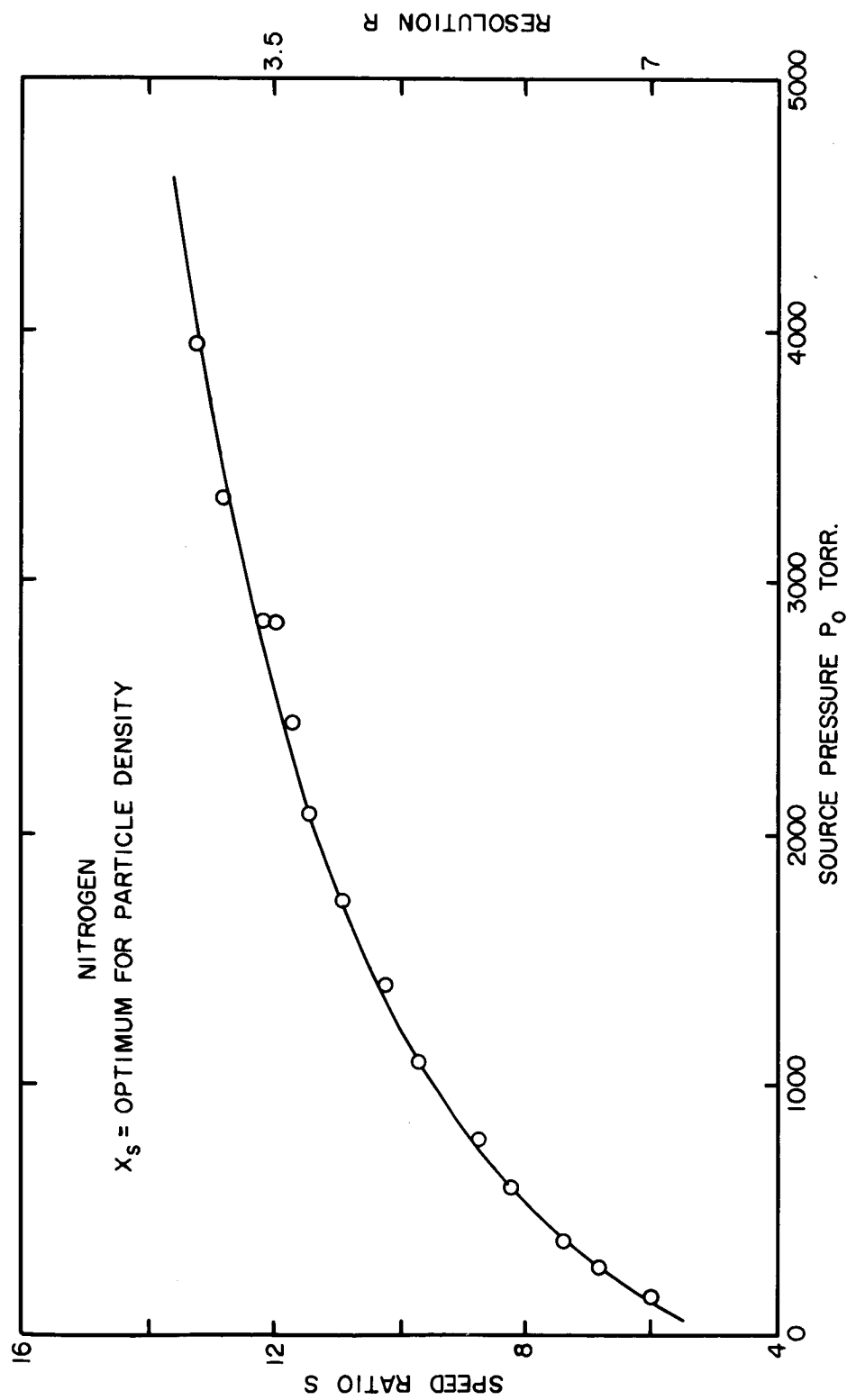


FIG. 5.3.2 SPEED DISTRIBUTION vs. SOURCE PRESSURE P_0 AT OPTIMUM NOZZLE-SKIMMER SEPARATION.

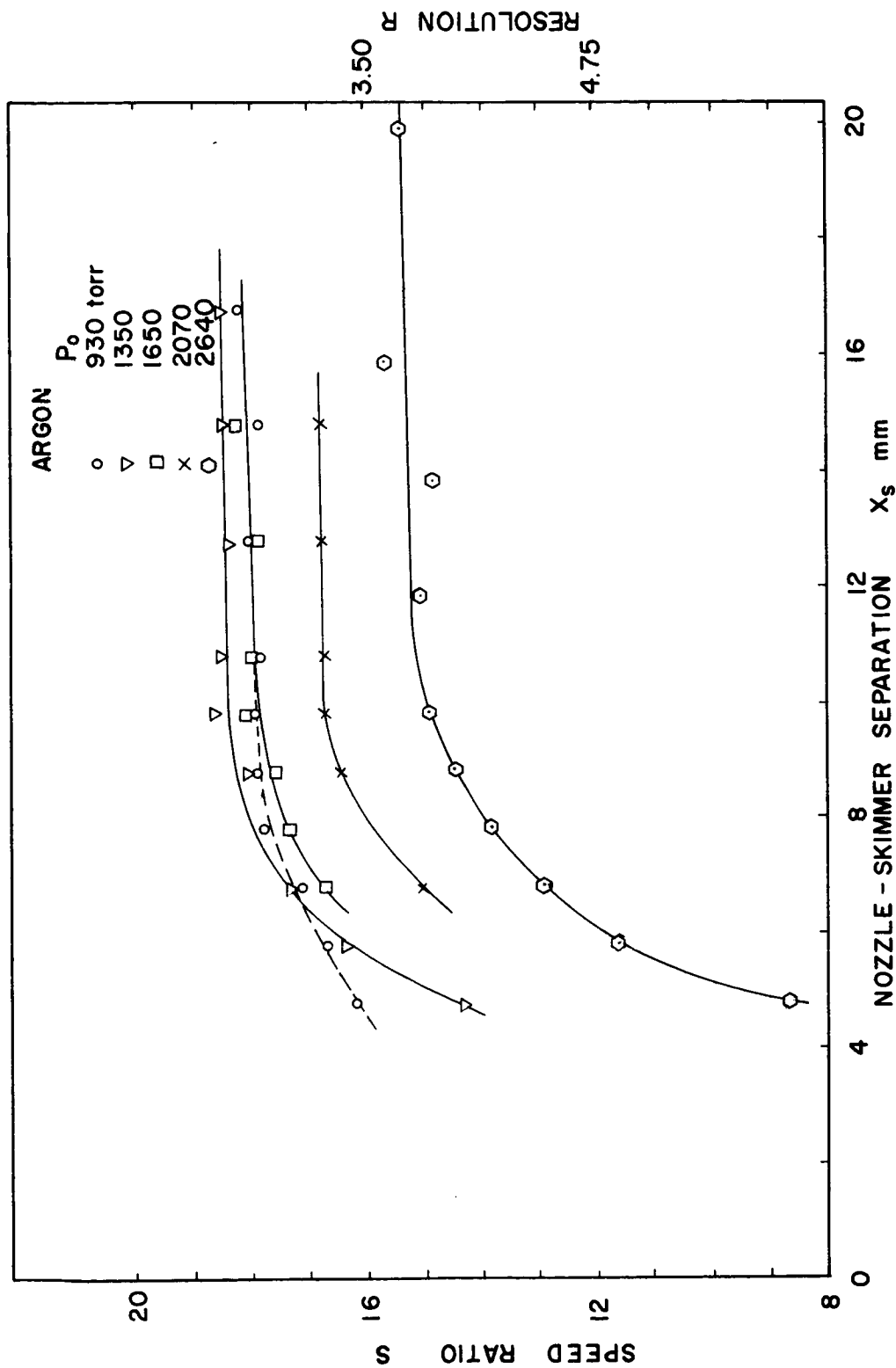


FIG. 5.3.3. VARIATION IN SPEED RATIO WITH NOZZLE-SKIMMER SEPARATION ON AXIS AT DIFFERENT SOURCE PRESSURE

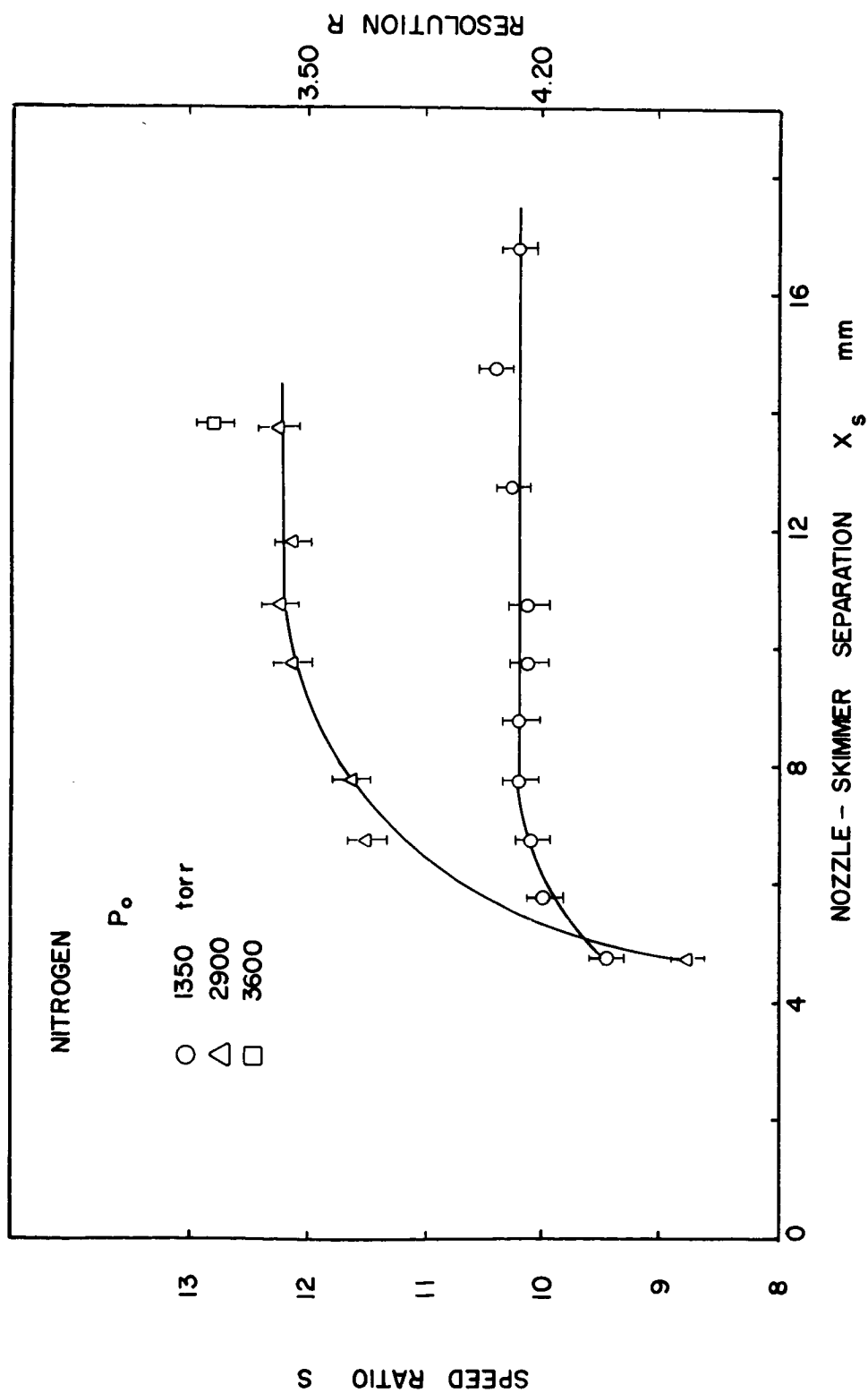


FIG. 5.3.4 VARIATION OF SPEED RATIO WITH NOZZLE - SKIMMER SEPARATION ON AXIS AT DIFFERENT SOURCE PRESSURES.

with the predicted onset of condensation, as mentioned in Section 2.2 (1350 torr vs 1400 torr), which was based on total beam intensity results with different nozzle sizes. In the case of nitrogen, results for source pressures of 1350 and 2900 torr and one point corresponding to 3600 torr are presented in Figure (5.3.4). The terminal speed ratio increases continuously with increasing source pressure. The crossing-over of the curves at $X_s = 5$ mm is due to larger skimmer interaction effects at the higher source pressure for the given geometry.

Off-Axis Speed Distribution Measurements. The high sensitivity of the detector enabled the measurement of off-axis beam speed distributions at angles of more than twice the angle corresponding to the half-shadow points. Reasonably accurate speed-ratio determinations could be made from the time-of-flight distributions, and these results are presented in Figures (5.3.5) and (5.3.6) for nitrogen beams. The only mechanism whereby beam particles can appear in the region beyond the half-shadow limits is that of collisions downstream of the skimmer. Therefore, speed ratio measurements in the region outside the half shadow should shed some light on the nature of these collisional processes.

Figure (5.3.5) shows the variation of off-axis beam speed ratio for nitrogen at a source pressure of 2900 torr and a nozzle-skimmer separation distance less than optimum. The beam speed-ratio decreases (from its centerline value) by a factor of about 1.7 at an angle corresponding to twice the half-shadow angle. The speed ratio is

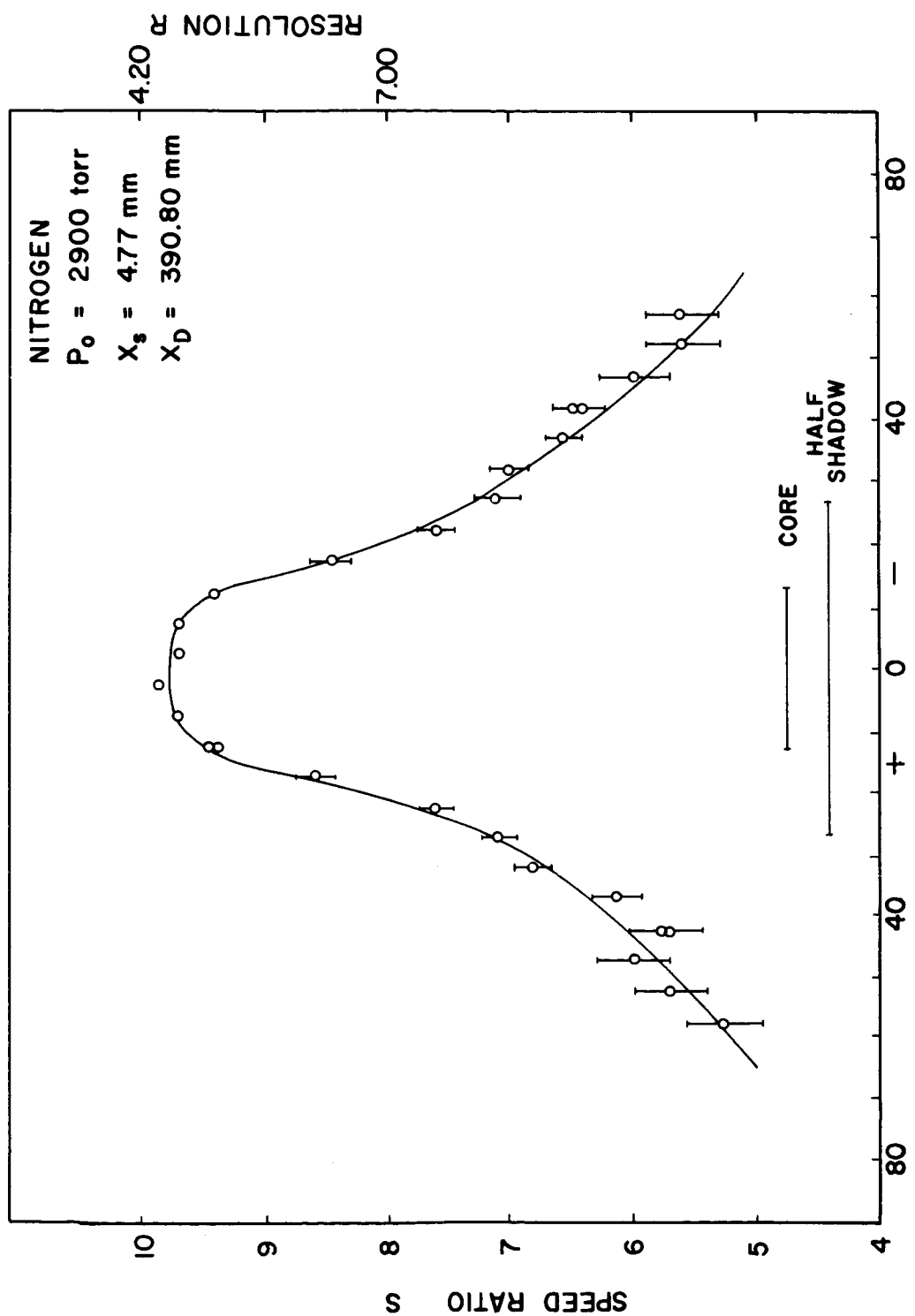


FIG. 5.3.5 VARIATION IN SPEED RATIO WITH OFF-AXIS DISPLACEMENT
 $X_s < X_{sOPT}$

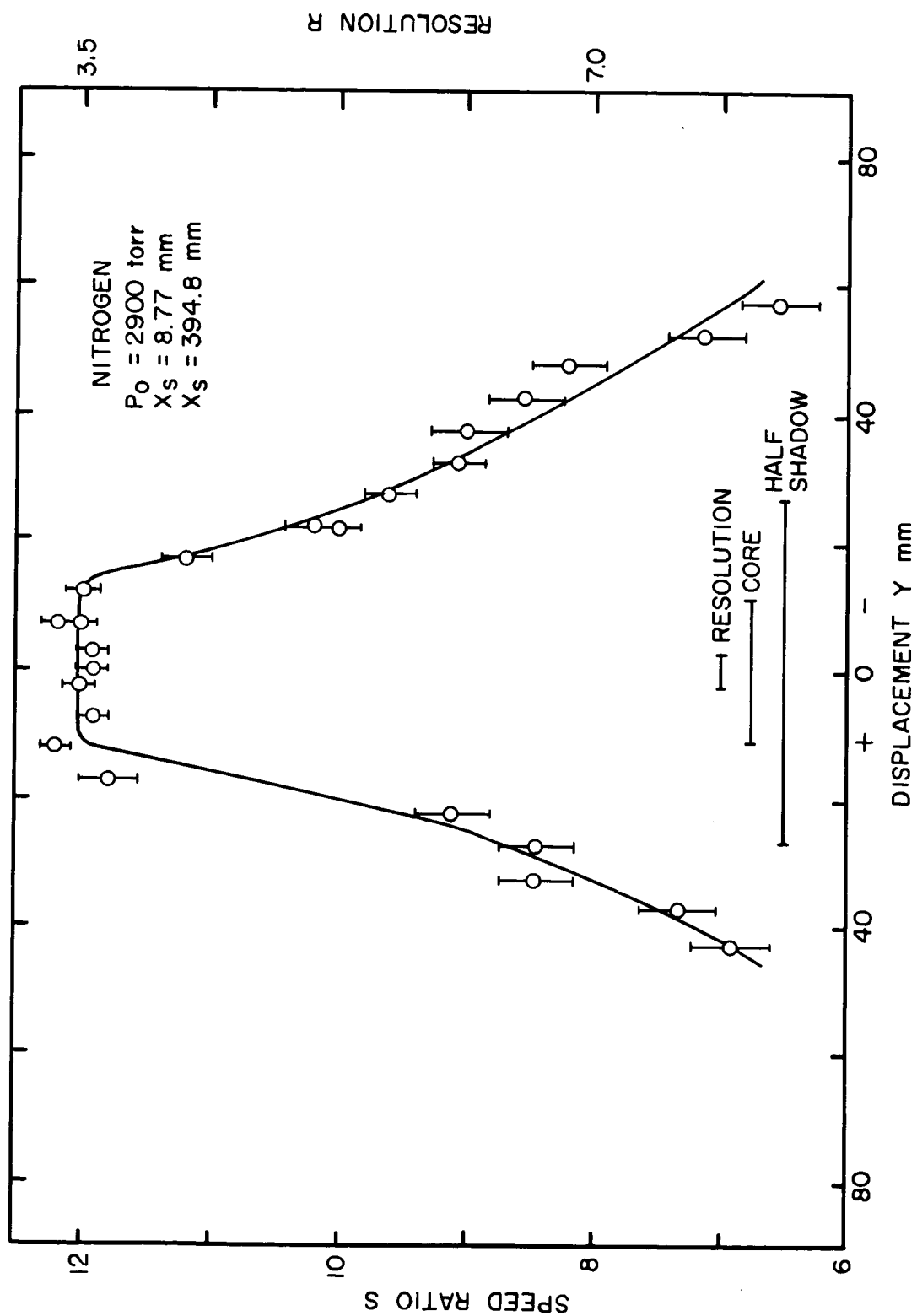


FIG. 5.3.6 VARIATION IN SPEED RATIO WITH OFF-AXIS DISPLACEMENT
 $X_S > X_{S \text{ opt.}}$

constant over a region corresponding to the beam core and decreases monotonically outside the core. Comparison of these results with the beam (intensity) profile data (see Figure 5.2.7) shows that the speed ratio is constant over a larger distance normal to the beam axis than is the beam particle density. It should be noted that the large angular displacements at which beam speed ratios have been obtained correspond to beam intensities of only 0.1% of the centerline value.

The speed ratio of beam particles in the tails; i. e., well off of the beam axis, is high. To reasonable approximation, the beam particles reflected off the skimmer inner wall will have a distribution corresponding to an oven source at the temperature of the skimmer surface; i. e., room temperature. Since the measured speed ratios in the region outside the half shadow are relatively high compared to such an oven beam's speed ratio, this is convincing evidence that the observed molecules do not originate from the skimmer surface. To the contrary, there is strong evidence that the molecules in this region are beam molecules which have been scattered by a small angle, with little change in energy, by collisions with a) molecules reflecting off the skimmer, b) background molecules in the collimation chamber, or c) other beam molecules.

The off-axis speed ratio values for nitrogen at a nozzle-skimmer separation larger than the optimum value is shown in Figure (5.3.6). The beam speed ratio here has larger values, both in the beam core and in the tails, than for the less-than-optimum nozzle-skimmer

separation distance case shown in Figure (5.3.5). Furthermore, the speed ratio is constant over a distance normal to the beam axis which is larger than the predicted dimensions of the beam core. Comparison of these results with those presented in Figure (5.2.9) (beam profile for $X_s = 9.77$ mm), shows that the beam speed ratio is constant over a larger distance normal to the beam axis than is the beam density.

Another series of experiments were performed by locating the time-of-flight detector at a fixed off-axis position, outside the half shadow, and measuring the beam speed distribution as a function of the nozzle-skimmer separation distance. The results of one such experiment are presented in Figure (5.3.7). In general, these results are similar to the results for variation of beam speed ratio with X_s on the beam axis. The number of particles appearing at this off-axis point increases rapidly as the nozzle-skimmer separation distance X_s is decreased. Initially, as X_s is decreased from its largest value of about 12 mm, the change in speed ratio is relatively small. At $X_s = 6$ mm, however, the speed ratio decreases sharply. The maximum speed ratio obtained at this point off of the beam axis is only 7.25 as compared to a value of 12 on the axis.

5.4 ASYMMETRY OF THE BEAM (DENSITY) PROFILE

As mentioned in Section 5.2, the nozzle beam density profile showed a slight asymmetry in both the core and in the half-shadow regions. Various experiments were performed in order to determine

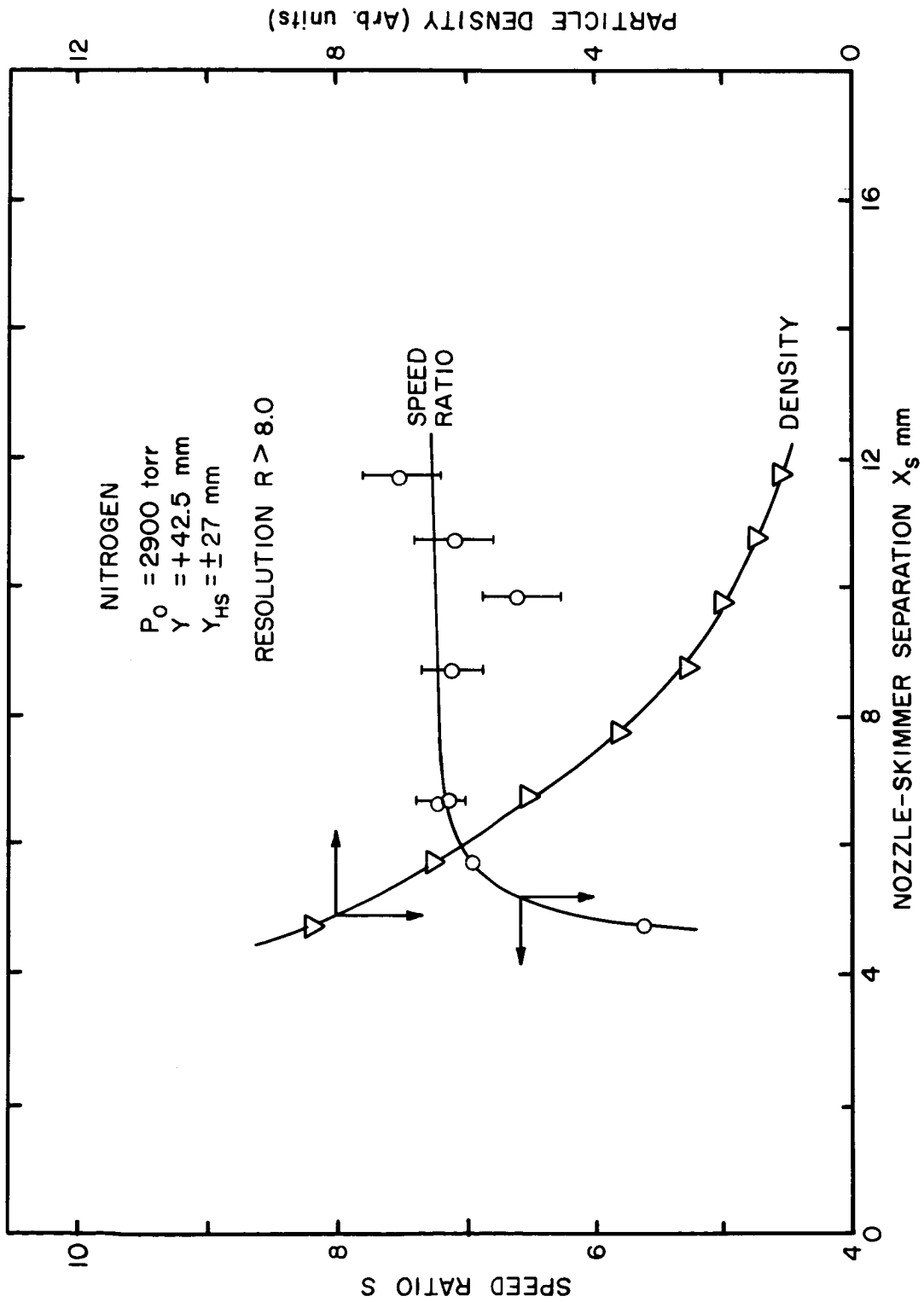


FIG. 5.3.7 VARIATION OF SPEED RATIO AND PARTICLE DENSITY WITH NOZZLE-SKIMMER SEPARATION DISTANCE AT $Y = +42.5 \text{ mm}$.

the cause of this asymmetry. The asymmetry is attributed primarily to one or more of the following factors; viz., nozzle misalignment, asymmetry or obliqueness in nozzle shape, pressure gradients in C_2 , and shape of the detection chamber C_3 .

The first two of these factors will easily lead to asymmetry in the beam profile. Because of the unusual shape of chamber C_2 , resulting in decreased conductance, a considerable pressure gradient can exist in the narrow part of the chamber. Consequently, beam attenuation due to background scattering will be nonuniform and may lead to the asymmetric type of beam profile observed. In order to investigate this point further, the pressure level in C_2 was increased by a factor of 30 by opening valve BV_2 , thus reducing the relative pressure gradient. The improvement in symmetry of the beam profile was very small. The shape of C_3 may be particularly responsible for the difference in intensities in the tails of the profile on each side of the beam axis. Conceivably, at positive displacements (see beam profiles for the meaning of positive displacement), the bulk of the beam can be reflected from the chopper disc, be reflected again from the center piece (the wall which holds the collimating orifice), and pass subsequently through the modulating system thereby increasing the detector signal. For negative displacements, this situation cannot exist. However, a simple calculation based on the solid angle subtended by the detector and the solid angle subtended by the center piece shows that this effect cannot account for more than a very small fraction of the observed asymmetry.

Increasing the nozzle-skimmer separation distance results in a small improvement in symmetry of the beam profile. Consequently, the major cause of the asymmetry is presumed to be nozzle misalignment and/or asymmetry. However, this factor alone is not entirely responsible for the asymmetry since effusive beams using the skimmer as source aperture, produced by bleeding gas through BV_1 into C_1 , also showed similar, though somewhat smaller, asymmetry. The pressure gradients in chamber C_2 , therefore, must also contribute to the observed asymmetry in the beam profiles. In any event, corrections for the slight asymmetry in beam intensity can be made easily in order that the beam system can be used for definitive scattering experiments.

SECTION VI

CONCLUSIONS

The molecular beam system described herein is capable of providing nozzle beams of high speed ratio (18.5 for argon and 13.6 for nitrogen)* and intensity ($7 \times 10^{18} \frac{\text{atoms}}{\text{sterad. sec.}}$ for both argon and nitrogen) which should prove to be useful in surface-scattering experiments, where low beam intensity has been a major limitation up to the present time.

The time-of-flight detector has exhibited excellent performance characteristics. It has a linear response to particle density and to emission current. The time-of-flight detection system provides a convenient method of speed distribution measurement, and its performance has been satisfactory and in reasonable agreement with theoretical predictions of the effects of finite shutter function.

The experimental results confirm the phenomenon of freezing of the translational temperature in freely expanding jets. The limitation on speed ratio and intensity of an argon nozzle beam due to partial condensation has been demonstrated.

Off-axis speed ratio measurements in the tails of the beam profile (beyond the half-shadow region) show that the speed ratio of the particles appearing therein is still approximately half the centerline value and that the relative fraction of molecules in these tails increases rapidly with decreasing skimmer Knudsen number and increasing collimation chamber pressure. The principal source of such molecules is

* Corrected for resolution.

concluded to be the result of small-angle scattering collisions (with accompanying small change in energy) of beam molecules downstream of the skimmer. These scattered molecules may have collided with molecules coming off the inner walls of the skimmer, background molecules in the collimation chamber, or with other beam molecules.

The optimum molecular beam generating conditions for this system have been established, and should prove useful for experiments on gas-surface interactions currently under way.

BIBLIOGRAPHY

BIBLIOGRAPHY

1. Kantrowitz, A and Grey, J. ; "High Intensity Source for the Molecular Beam", Review of Scientific Instruments, Vol. 22, No. 5, p. 328, May 1951.
2. Hagen, Otto F. and Morton, Harold S., Jr. ; "Analysis of Intensity and Speed Distribution of a Molecular Beam from a Nozzle Source", Rarefied Gas Dynamics, Vol. II, Academic Press, p. 1369 (1967).
3. Schüller, Paul G. ; "Effect of Nozzle Diameter on Intensity and Mach Number of Supersonic Molecular Beams". Thesis, T. H. Karlsruhe, 1964.
4. Bier, K, and Hagen, Otto F. ; "Optimum Conditions for Generating Supersonic Molecular Beams", Rarefied Gas Dynamics, Vol. II, Academic Press, p. 260, (1966).
5. Scott, J. E., Jr. and Drewry, J. E. ; "Characteristics of Aerodynamic Molecular Beams", Rarefied Gas Dynamics, Vol. I, Academic Press, p. 516 (1963).
6. Zapata, Ricardo N. ; "Experimental Analysis of Molecular Beams at High Source Pressures". Ph.D. Dissertation, University of Virginia, June 1960.
7. Kerr, R. J. ; "Plasma Density Measurements with A Molecular Beam", Nuclear Fusion, Vol. 3, p. 197 (1963).
8. Hagen, Otto F. and Henkes, W. ; "Investigation of the Thermal Relaxation in Nozzle Flows by Analysis of the Gas Kinetic Velocity Distribution", Zeitschrift für Naturforschung, Vol. 15a, 10, p. 851 (1960).
9. Anderson, J. B. and Fenn, J. B. ; "Velocity Distributions in Molecular Beams from Nozzle Sources", The Physics of Fluids, Vol. 8, No. 5, p. 780, May 1965.
10. Becker, E. W. and Henkes, W. "Velocity Analysis of Laval Beams", Zeitschrift für Physik, Vol. 146, p. 320 (1956).
11. Hagen, Otto F. ; "Calculations for Rectangular Shutter Function", Private Communication (1966),
12. Scott, Paul B., Bauer, Paul H., Wachman, Harold Y., and Trilling, Leon ; "Velocity Distribution Measurements by Sensitive Time-of-Flight Method", Rarefied Gas Dynamics, Vol. II, Academic Press, p. 1353 (1967).

13. Hagena, Otto F. and Schüller, P. G. ; "Intensity and Speed Distribution of Pulsed Supersonic Molecular Beams", Z. Angew. Phys., Vol. 17, No. 7, p. 542 (1964).
14. Fenn, J. B. and Anderson, J. B. ; "Background and Sampling Effects in Free Jet Studies by Molecular Beam Measurements", Rarefied Gas Dynamics, Vol. II, Academic Press, p. 311 (1966).
15. Scott, J. E., Jr. and Phipps, John A. ; "Translational Freezing in Freely Expanding Jets", Rarefied Gas Dynamics, Vol. II, Academic Press, p. 1337 (1967).

APPENDICES

APPENDIX A

DESIGN OF THE BEAM DEFINING ELEMENTS

One of the important classes of experiments intended to be performed with this molecular beam system are surface scattering studies with various targets, at different temperatures and with nozzle sources at different temperatures. The requirements for these experiments are contradictory to those required for the other class of experiments; viz., investigation of the transition flow regime in the freely expanding jets. As an example the scattering experiments will require a very small nozzle whereas the other experiments will require rather large nozzle sizes. The design of the system, however, enables operation at either of these two extreme limits.

Nozzle Design. The advantages of using a simple converging nozzle has been discussed in the text and other references^{(2) (5)}. The optimum nozzle size depends on the particular beam gas. However, for argon, nitrogen and carbon dioxide, it has been found by experiment that the best nozzle size varies from 0.05 to 0.15 mm. diameter. The nozzle obtained from the machine shop had a diameter of 0.06 mm. It has been found to be quite suitable and has been used in all of the experiments reported herein. On the basis of the experimental results of Bier and Hagena⁽⁴⁾, the limiting condition for the generation of non-condensed molecular beams at room temperature is that the product of source pressure and nozzle diameter ($P_o \times D_n$) be less than 60, 85, 500 torr mm. for CO_2 , argon, and nitrogen, respectively. For a nozzle diameter of 0.06 mm,

the limiting source pressures P_o are as follows:

CO ₂	1000 torr
Argon	1400 torr
Nitrogen	8000 torr

Skimmer and Collimator. The design of the skimmer and collimator are governed primarily by the geometry of the system. As an example, a check on the design of the system for a beam cross-section at the target of 5 mm. diameter and an intensity of the order of 5×10^{18} atoms per steradian-sec is outlined below:

Distance of target from the nozzle $X_t = 87.9$ mm.

$$\begin{aligned} \text{Desired beam area at target } A_t &= \frac{\pi}{4} \times 5^2 \\ &= 19.63 \text{ mm.}^2 \end{aligned}$$

$$\begin{aligned} \text{Solid angle subtended by target at the nozzle } d\Omega_t &= \frac{19.63}{(87.9)^2} \\ &= 2.54 \times 10^{-3} \text{ sterad.} \end{aligned}$$

The size of the skimmer must be larger than that corresponding to this solid angle, by at least twice the characteristic skimmer radius. The characteristic skimmer radius r_s^* for a monatomic gas defined as

$$\begin{aligned} \frac{r_s^*}{D_n} &= 0.67 \cdot \left(\frac{X_s}{D_n} \right)^{1/3} \\ r_s^* &= 0.67 \cdot 0.06 \cdot \left(\frac{8.00}{0.06} \right)^{1/3} \\ &= 0.205 \text{ mm.} \end{aligned}$$

(X_s can be varied from 4.77 to nearly 50 mm. At normal operating conditions, however, it will range from 5 to 10 mm. An average value is being used in the calculation above.) At a skimmer separation of 8.00 mm.,

the required skimmer diameter, based on solid angle considerations, is

$$\frac{\pi}{4} D_s'^2 = 2.54 \cdot 10^{-3} \cdot 64$$

$$D_s' = 0.454 \text{ mm.}$$

Hence, a recommended skimmer size will be of the order of

$$\begin{aligned} D_s &= 0.454 + 0.410 \\ &= 0.864 \text{ mm.} \end{aligned}$$

For a diatomic gas such as nitrogen, r_s^* is larger because of the lower speed ratio S_s . Hence, a larger skimmer size is desirable. Skimmers with diameters ranging from 0.7 mm. to 2.0 mm. have been fabricated for use with this beam system. A 1 mm. skimmer was used for most of the experiments. The other details of skimmer design are discussed in Section 2.2.

Under normal operating conditions, the collimator is 25.55 mm. from the nozzle. For a solid angle of $2.54 \cdot 10^{-3}$ sterad.

$$\frac{\pi}{4} D_c^2 = 2.54 \cdot 10^{-3} \cdot (25.55)^2$$

$$D_c = 1.487$$

$$\approx 1.50 \text{ mm.}$$

A collimator of 1.50 mm. diameter has been used for most of the experiments, and it forms the beam defining orifice. Two additional collimators with diameters of 1.35 mm. and 2.5 mm. are available for use in the beam system. Other considerations in collimator design are discussed in Section 2.2.

Pumping System. Consider a source pressure of 1400 torr with the source gas at room temperature (298°K). The mass flow through the nozzle is given by

$$\begin{aligned}\dot{m}_n &= 14.3 \cdot D_n^2 \cdot P_o (\text{cm}^2 \cdot \text{torr})^{-1} \frac{\text{torr lit}}{\text{sec}} \\ &= 14.3 \cdot .006^2 \cdot 1400 = 72 \cdot 10^{-2} \frac{\text{torr lit}}{\text{sec}}\end{aligned}$$

The Stokes booster pump has a specified maximum pumping speed of 4500 lit/sec at 12 kw (it is being operated currently at 6 kw, and the actual pumping speed may be higher).

Hence, the normal pressure in chamber C_1 is $1.6 \cdot 10^{-4}$ torr.

An estimate of the flux into the collimation chamber C_2 can be made as follows:

$$\begin{aligned}\text{The solid angle subtended by 1 mm. dia. skimmer} &= \frac{\frac{\pi}{4} \cdot 1^2}{8^2} \\ &= 0.0123 \text{ sterad.}\end{aligned}$$

The isentropic density on the axis is given by

$$\begin{aligned}n(X) &= 1.13 \cdot 10^{-5} \cdot \frac{\dot{m}_n}{X^2} \frac{\text{atoms}}{\text{cm}^3} \\ &= 0.161 \cdot n_o \cdot \left(\frac{X}{D_n}\right)^{-2} \\ \therefore n(X_s) &= 0.161 \cdot 3.24 \cdot 10^{16} \cdot 1400 \cdot \left(\frac{.06}{8}\right)^2 \\ &= 4.1 \cdot 10^{14} \frac{\text{atoms}}{\text{cm}^3}\end{aligned}$$

Since terminal speed for argon is $5.50 \cdot 10^4$ cm/sec, the beam intensity is $2.26 \cdot 10^{19} \frac{\text{atoms}}{\text{cm}^2 \text{ sec}}$.

For a skimmer of 1 mm. diameter, the flux into the collimator chamber

$$= 2.26 \cdot 10^{19} \cdot \frac{\pi}{4} \cdot (.1)^2$$

$$= 1.775 \cdot 10^{17} \text{ atoms/sec}$$

$$= 5.52 \cdot 10^{-3} \text{ torr lit/sec}$$

Hence, for a normal operational pressure in C_2 of 10^{-5} torr, a pumping speed of 552 lit/sec is required. The nominal pumping speed of S_2 is 4200 lit/sec. (The extra pumping capacity will be useful for experiments with larger skimmers.) However, the primary reason for the larger pump was to compensate for the rather low conductance of C_2 . The geometry of this section was determined by the requirements of the shape of the scattering, or detection, chamber. Due to the relatively narrow cross-section of the region through which the beam passes, it is to be expected that a considerably higher pressure will occur in this region than that obtained from beam flux-pumping speed considerations. The pump in use currently is found to have a satisfactory performance in that, even an increase in the pressure at the pump inlet by a factor of 5 (by opening bleed valve BV_2) does not result in appreciable attenuation of the beam.

Total intensity measurements with argon indicated a maximum beam intensity of $7 \cdot 10^{18} \frac{\text{atoms}}{\text{sterad. sec}}$. The collimator has a diameter of 1.5 mm. which corresponds to a solid angle

$$\begin{aligned} d\Omega_{co} &= \frac{\frac{\pi}{4} \cdot (1.5)^2}{(25.55)^2} \\ &= 2.70 \cdot 10^{-3} \text{ sterad.} \end{aligned}$$

$$\begin{aligned} \text{Hence, the beam flux into } C_3 &= 5.85 \cdot 10^{18} \cdot 2.70 \cdot 10^{-3} \\ &= 1.58 \cdot 10^{16} \frac{\text{atoms}}{\text{sec}} \\ &= 4.92 \cdot 10^{-4} \frac{\text{torr lit}}{\text{sec}} \end{aligned}$$

For a background pressure of 10^{-7} torr in C_3 , a pumping speed of 4920 lit/sec is required. The 16" diffusion pump S_3 has a rated maximum pumping speed of 10,000 lit/sec. Therefore, under normal operating conditions, the system performance should be quite satisfactory.

APPENDIX B

DESIGN CALCULATIONS FOR THE TIME-OF-FLIGHT DETECTOR

Consider the following parameters of the electron beam:

U_{el}	Voltage corresponding to the total momentum of the electrons (i. e. , the accelerating voltage)
U_{\perp}	Voltage corresponding to the momentum of the electron normal to the magnetic field
H	Strength of the magnetic field
U_{ion}	Ion extraction voltage
E_{ion}	Electric field strength corresponding to U_{ion}
E_{el}	Electric field strength corresponding to U_{el}
r	Radius of curvature in a magnetic field
t_r	Time for one revolution in a magnetic field
t_t	Time to travel a distance l
v	Electron velocity = l/t_t
v_D	Drift velocity in crossed magnetic and electrical fields H and E_{ion}
v_{\perp}	Transverse electron velocity due to U_{\perp}

Then

$$\begin{aligned}
 v &= \left(\frac{2qU_{el}}{m} \right)^{1/2} \\
 &= 5.94 \cdot 10^7 (U_{el}/\text{volt})^{1/2} \text{ cm/sec} \\
 r &= \frac{mv_{\perp}}{qH} \\
 &= 3.38 (U_{\perp}/\text{volt})^{1/2} (\text{Gauss}/H) \text{ cm} \\
 f &= \frac{qH}{2\pi m}
 \end{aligned}$$

$$\begin{aligned}
 t_r &= \frac{1}{f} \\
 &= 3.562 \cdot 10^{-7} \text{ (Gauss/H) sec} \\
 v_D &= \frac{E_{ion}}{H} \\
 &= 10^8 (E_{ion} \text{ cm/volt}) \text{ (Gauss/H) cm/sec}
 \end{aligned}$$

For the typical experimental parameters of

$$H = 350 \text{ Gauss}$$

$$U_{el} = 200 \text{ volts}$$

$$U_{\perp} = 50 \text{ volts (this is rather high and represents the upper$$

limit for this parameter)

$$l = 1.6 \text{ cm}$$

$$E_{ion} = 200 \text{ volts/cm corresponding to a } U_{ion} \text{ of 270 volts, one}$$

gets $r = 0.0682 \text{ cm}$

$$t_r = 1.01 \cdot 10^{-9} \text{ sec}$$

$$t_t = 1.89 \cdot 10^{-9} \text{ sec}$$

$$v = 8.4 \cdot 10^8 \text{ cm/sec}$$

$$v_D = 5.72 \cdot 10^7 \text{ cm/sec}$$

The drift length $= (5.72 \cdot 10^7) \cdot (1.89 \cdot 10^{-9}) = 1.08 \text{ mm}$ over a travel path of 16 mm.

Thus, for a properly aligned cathode, nearly all the electrons should pass through the slits ($2 \times 16 \text{ mm}^2$) because normal values of U_{\perp} will be less than 50 volts and consequently, r will be even smaller than the above value.

As $v \gg v_D$, the path of the electrons deviates only slightly from a straight line. As $t_r \approx t_t$, the electron gyration will not appreciably increase the pathlength. An increase in pathlength of no more than 10% will occur for the above conditions.

APPENDIX C

THEORETICAL CONSIDERATIONS REGARDING A PULSED NOZZLE BEAM: EFFECT OF FINITE SHUTTER FUNCTION

An analysis of the effect of the shutter function on the wave-form to be expected from the detector is described below in order to provide more accurate and quantitative information on the relationship between the shutter function and the detector output. The results may also be helpful in providing a check on the performance of the electronic circuitry used for signal amplification and analysis. Similar analyses have been reported by Becker and Henkes⁽¹⁰⁾ for the case of a square pulse shutter function and an ideal flux distribution function for nozzle beams, and by Scott⁽¹²⁾ for the case of a triangular shutter function and its effect on a molecular beam with a Maxwellian velocity distribution. The object of the present analysis is to consider the effect of triangular shutter functions on nozzle beam speed distributions for density of the form

$$f(v) = A' v \exp \left[-\beta (\vec{v} - \vec{v}_0)^2 \right] \quad (C - 01)$$

recommended by Hagena and Morton⁽²⁾ for including the effects of flow divergence upstream of the skimmer. Transformation to time coordinates (see Section 3.6) gives

$$S_0(t) = \frac{A''}{t^3} \exp \left[-B \left(\frac{1}{t} - \frac{1}{t_0} \right)^2 \right] \quad (C - 02)$$

$$B = \beta L^2, \quad t_0 = \frac{L}{V_0}$$

which is the detector response for an infinitely narrow shutter function.

For an arbitrary shutter function, the detector response can be evaluated by considering the arbitrary function to be made up of a large number of infinitely narrow pulses, each of which has the individual response represented by Equation C. 02. The final response is simply the superposition of these individual response functions. This process is mathematically formulated in terms of the convolution integral. If $S_0(t)$ is the output (i. e., corresponding to Equation C. 02) for a delta shutter function (infinitely narrow) and $g(t)$ represents the actual shutter function, then

$$S(t) = \int_0^{\infty} S_0(t - \tau) g(\tau) d\tau \quad (C-03)$$

Consider a triangular shutter function with a half-width T . Let the height of the shutter function be G_0 . Then,

$$g(t) = G_0 \frac{t}{T} \quad 0 \leq t \leq T \quad (C-04a)$$

$$= G_0 \left(2 - \frac{t}{T}\right) \quad T \leq t \leq 2T \quad (C-04b)$$

$$= 0 \quad t > 2T \quad (C-04c)$$

Using C-04 c in Equation C-03,

$$S(t) = \int_0^{2T} S_0(t - \tau) g(\tau) d\tau \quad (C-05)$$

For convenience, let

$$t - \tau = \tau'$$

$$-d\tau = d\tau'$$

$$S(t) = \int_{t-2T}^t S_0(\tau) g(t-\tau) d\tau \quad (C-06)$$

Substitution for S_0 and g gives

$$\begin{aligned} S(t) = & A'' G_0 \int_{t-T}^t \frac{t-\tau}{T} \cdot \frac{1}{\tau^3} \exp\left[-B\left(\frac{1}{\tau} - \frac{1}{t_0}\right)^2\right] d\tau \\ & + \int_{t-2T}^t \left(2 - \frac{t-\tau}{T}\right) \frac{1}{\tau^3} \exp\left[-B\left(\frac{1}{\tau} - \frac{1}{t_0}\right)^2\right] d\tau \end{aligned}$$

Let

$$\sqrt{B} \left(\frac{1}{\tau} - \frac{1}{t_0} \right) = x$$

$$\sqrt{B} \left(-\frac{d\tau}{\tau^2} \right) = dx$$

Then,

$$\begin{aligned} \frac{S(t)}{A'' G_0} = & -\frac{1}{\sqrt{B}} \left[\int_{t-T}^t dx \left\{ \frac{t}{T} \cdot \frac{1}{\tau} \exp(-x^2) \right. \right. \\ & \left. \left. - \frac{1}{T} \exp(-x^2) \right\} + \int_{t-2T}^{t-T} dx \left\{ \left(2 - \frac{t}{T}\right) \frac{1}{\tau} \exp(-x^2) \right. \right. \end{aligned}$$

and further

$$\begin{aligned}
 & + \frac{1}{T} \exp(-x^2) \} \Big] \\
 \frac{S(t)}{A'' G_0} = & + \frac{1}{\sqrt{B}} \left[\int_{\sqrt{B}(\frac{1}{t} - \frac{1}{t_0})}^{\sqrt{B}(\frac{1}{t-T} - \frac{1}{t_0})} dx \left\{ \frac{t}{T} \left(\frac{x}{\sqrt{B}} + \frac{1}{t_0} \right) \exp(-x^2) \right. \right. \\
 & \left. \left. - \frac{1}{T} \exp(-x^2) \right\} + \int_{\sqrt{B}(\frac{1}{t-T} - \frac{1}{t_0})}^{\sqrt{B}(\frac{1}{t-2T} - \frac{1}{t_0})} dx \left\{ \left(2 - \frac{t}{T} \right) \left(\frac{x}{\sqrt{B}} + \frac{1}{t_0} \right) \exp(-x^2) \right. \right. \\
 & \left. \left. + \frac{1}{T} \exp(-x^2) \right\} \right] \quad (C-07)
 \end{aligned}$$

After simplification, one obtains

$$\begin{aligned}
 \frac{S(t)}{\frac{1}{2} A'' G_0} = & \sqrt{\frac{\pi}{B}} \left[\left(\frac{1}{T} - \frac{t}{T t_0} \right) \left\{ \operatorname{erf} \sqrt{B} \left(\frac{1}{t} - \frac{1}{t_0} \right) - \operatorname{erf} \sqrt{B} \left(\frac{1}{t-T} - \frac{1}{t_0} \right) \right\} \right. \\
 & + \left(\frac{1}{T} + \frac{2}{t_0} - \frac{t}{T t_0} \right) \left\{ \operatorname{erf} \sqrt{B} \left(\frac{1}{t-2T} - \frac{1}{t_0} \right) \right. \\
 & \left. \left. - \operatorname{erf} \sqrt{B} \left(\frac{1}{t-T} - \frac{1}{t_0} \right) \right\} \right] + \frac{1}{B^2} \left[\frac{t}{T} \left\{ \exp \left[- \left(\sqrt{B} \left(\frac{1}{t} - \frac{1}{t_0} \right) \right)^2 \right] \right. \right. \\
 & \left. \left. - \exp \left[- \left(\sqrt{B} \left(\frac{1}{t-T} - \frac{1}{t_0} \right) \right)^2 \right] \right\} + \left(2 - \frac{t}{T} \right) \left\{ \exp \left[- \left(\sqrt{B} \left(\frac{1}{t-T} - \frac{1}{t_0} \right) \right)^2 \right] \right. \right. \right. \\
 & \left. \left. - \exp \left[- \left(\sqrt{B} \left(\frac{1}{t-2T} - \frac{1}{t_0} \right) \right)^2 \right] \right\} \right] \quad (C-08)
 \end{aligned}$$

Normalizing all times by $t_0 = \frac{L}{\text{streaming velocity}}$, and normalizing the signal intensity by $1/2 A''G_0$ and using the nomenclature

$$P = \frac{t}{t_0} \qquad Q = \frac{T}{t_0}$$

$$AOQ = \sqrt{B} \left(\frac{1}{P} - 1 \right)$$

$$AIQ = \sqrt{B} \left(\frac{1}{P-Q} - 1 \right)$$

$$A2Q = \sqrt{B} \left(\frac{1}{P-2Q} - 1 \right)$$

$$\begin{aligned} S'(P) = \sqrt{\frac{\pi}{B}} & \left[\left(\frac{1}{Q} - \frac{P}{Q} \right) (\text{erf } AOQ - \text{erf } AIQ) \right. \\ & \left. + \left(\frac{1}{Q} + 2 - \frac{P}{Q} \right) (\text{erf } A2Q - \text{erf } AIQ) \right] \\ & + \frac{1}{B^2} \left[\frac{P}{Q} \{ \exp(-AOQ^2) - \exp(-AIQ^2) \} \right. \\ & \left. + \left(2 - \frac{P}{Q} \right) \{ \exp(-AIQ^2) - \exp(-A2Q^2) \} \right] \end{aligned}$$

(C-09)

which represents the expected detector signal for a triangular shutter function of half-width Q . A computer program on the Burroughs B-5500 Machine was used to evaluate the above function for various combinations of shutter function half-width (Q) and beam speed ratio (related to the constant B).

Since $B = \beta L^2$ where

$$\beta = \frac{m}{2kT_e}$$

and, by definition $S = \frac{v_o}{\sqrt{\frac{2kT_e}{m}}}$

$$= v_o \sqrt{\beta}$$

$$= \frac{v_o}{L} \sqrt{B}$$

then, $S \cdot t_o = \sqrt{B}$

For $t_o = 1$ (i. e., normalization), $B = S^2$

Calculations have been performed for speed ratios of 5, 10, and 20 with shutter function half-widths ranging from 0.005 to 0.60 of t_o . In order to compare the nozzle beam results with the corresponding results for effusion beams, a similar computer program was written using the results obtained by Scott⁽¹²⁾ to obtain more detailed information over a larger range of values of shutter functions. Normalizing times with βL , shutter function half-widths from 0.05 to 16.0 were used.

APPENDIX D

DESIGN CALCULATIONS FOR THE BEAM MODULATION SYSTEM

The design of the beam modulation system is based on the considerations presented in Section 4. On the basis of the design of the time-of-flight detector, it is estimated that the "active zone" of the detector extends over a distance δL of 1 mm.

A flight path $L = 25.4$ cm was chosen to provide $\frac{\delta L}{L}$ of $4 \cdot 10^{-3}$ which is sufficiently small to give good axial resolution. Good spatial resolution required the use of an entrance aperture in front of the detector providing an effective detector aperture of 5 mm. diameter. By simple geometrical considerations, this corresponds to a beam size at the chopper slit of 1.765 mm diameter. (if the beam cross-section had been rectangular, a slit width equal to the beam width will provide a triangular shutter function. However, for a circular beam, the shutter function will have a different shape as shown in Figure D.1 even though this function has the same half-width.)

The chopper disc obtained from the shop had a slit width of 1.725 mm which was sufficiently close to the desired figure.

The physical size of the rotating table and the motor characteristics suggested a 7.6 cm nominal dia. disc to be suitable. For the beam total density measurements a lighter disc of 5 cm. nominal dia. was used. The discs are shown in Figure (4.3.1).

The maximum motor speed was limited to 300 cps, in the interests of motor lifetime, which was sufficient for most requirements.

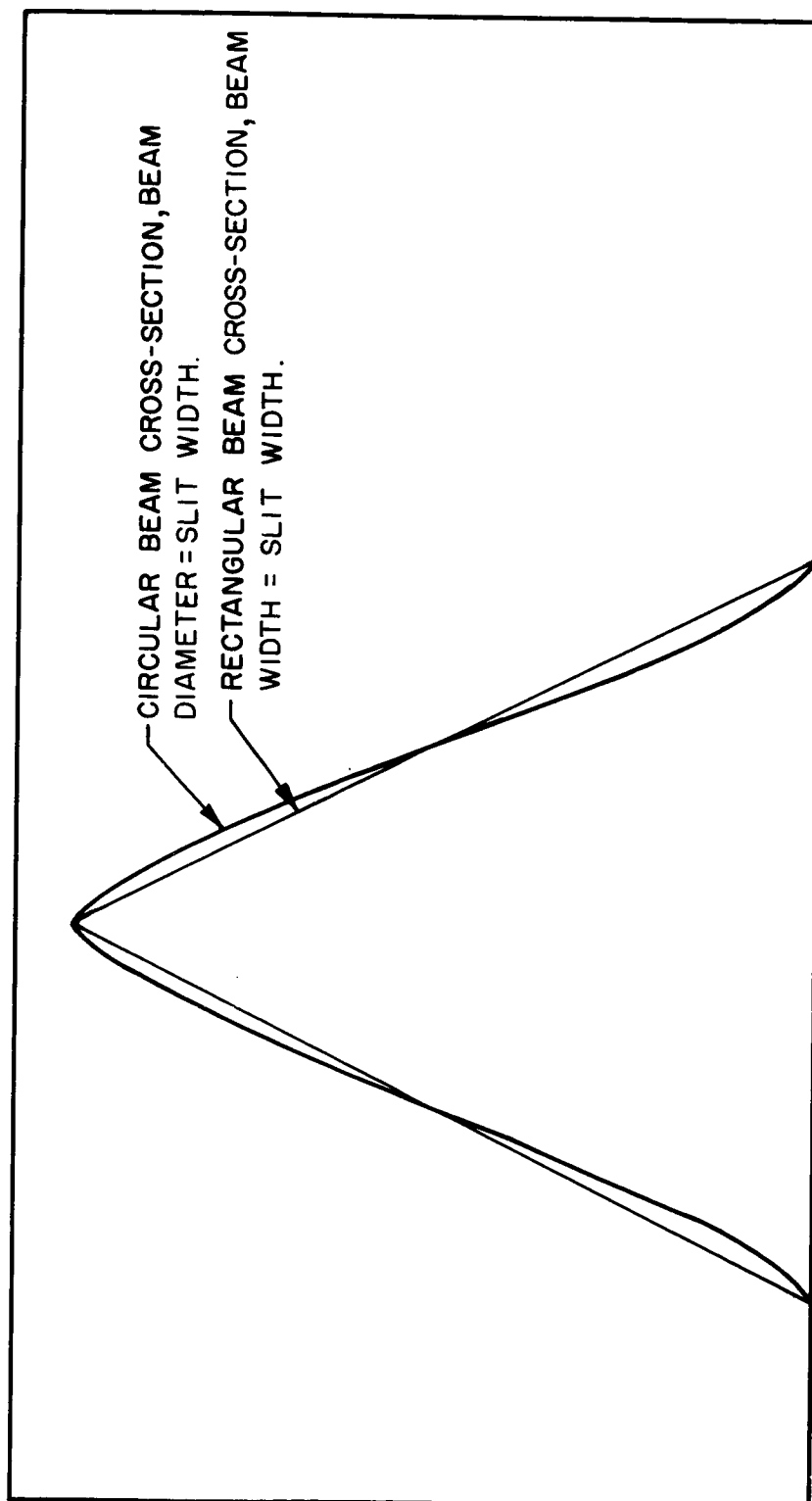


FIG. D.1 EFFECT OF CIRCULAR BEAM CROSS-SECTION ON SHUTTER FUNCTION.

The resolution $\frac{\Delta t}{T}$ that can be obtained with this motor speed for a speed ratio of 20 can be calculated as follows:

In the limit of high speed ratios ($a \rightarrow 1$) the expression for S developed in Section 3.6; i. e.

$$S = \frac{h(a)}{\sqrt{g(a)}}$$

becomes

$$\begin{aligned} S &\approx \frac{\sqrt{\ln 2}}{a - 1} \\ &\approx 1.67 \times \frac{t_m}{\Delta t} \end{aligned} \quad (D-01)$$

This gives, for $S = 20$ and room temperature argon beams

$$\frac{t_m}{\Delta t} \approx 12 \quad (D-02)$$

$$\begin{aligned} \text{Now } t_m &= \frac{L}{u} = \frac{25.4 \text{ cm}}{5.5 \cdot 10^4 \text{ cm/sec}} \\ &= 462 \cdot 10^{-6} \text{ sec} \end{aligned} \quad (D-03)$$

$$\Delta t \approx 38.5 \cdot 10^{-6} \text{ sec} \quad (D-04)$$

The half-width T of the shutter function, for $s_t = 1_t$ and for the motor speed of 300 cycles/sec is

$$\begin{aligned} T &= \frac{1.725 \text{ mm} \cdot \text{sec}}{2\pi \cdot 300 \cdot 76.25 \text{ mm}} \\ &= 12 \cdot 10^{-6} \text{ sec.} \end{aligned} \quad (D-05)$$

Combining Equation (04) and Equation (05), we get

$$R = \frac{\Delta t}{T} = \frac{38.5}{12}$$

$$\approx 3.2$$

Referring to Figure (4.4.2), a resolution of 3.2 corresponds to a measured Δt which is not more than 5% greater than the ideal value

Δt_0 and a corresponding correction can be applied to the measured Δt .

Thus the system is capable of satisfactorily resolving beams of speed ratio up to 20, (or Mach number of 22).

The chopper disc in use for high resolution measurements has four slits. This allows for a resolution of

$$\begin{aligned} R &= \frac{\Delta t}{T} = \frac{\Delta t}{T_c} \cdot \frac{T_c}{T} = \frac{\Delta t}{T_c} \cdot \frac{2 \pi r}{4 s_t} \\ &= \frac{\Delta t}{T_c} \cdot 70 \end{aligned}$$

which, if the overlap condition $T_c = 5 \cdot \Delta t$ can be satisfied, becomes

$R = \frac{70}{5} = 14$. The motor speed (300 c/s), however, limits T_c to $(T_c)_{\min}$.

$= 833 \mu \text{sec}$. and the maximum resolution can be utilized only for beams

with $\Delta t \geq \frac{1}{5} (T_c)_{\min} = 166 \mu \text{sec}$. For argon at room temperature,

this corresponds to $S \leq 5$.

APPENDIX E

RECOMMENDED OPERATING PROCEDURES

The normal schedule of events for a typical experimental run will, in general, be as follows. The details will, of course, vary with the nature of the experiment.

START-UP PROCEDURE

System opened (if necessary) after previous run. Complete necessary changes; i. e., install new skimmer and/or collimator. Install selected nozzle. Check alignment of orifices. Install suitable chopper disc. Check detector and chopper circuitry. Close the system.

00.00 hrs. Check and close bleed valves BV_1 , BV_2 , BV_3 . Check that interconnecting main valves MV_{32} , MV_{21} and feed through valves $FTV_{1, 2, 3}$ are open. Open gage line valves. Start cooling water to pumps. Check temperature control override off.

Open valve MV_{10} .

Start mechanical pump M_o .

00.15 Watch P_{10} . When below 0.2 torr start diffusion pumps S_1 , S_2 , S_3 in above order at 5 minute intervals.

01.00 All chamber pressures now below 10^{-3} torr. Switch on ionization pressure gage when $P_3 < 10^{-5}$ torr.

Switch on Time-of-Flight Detector at low emission

- current. Start chopper disc rotation at slow speed. Verify that all electronic circuitry is operational.
- 06.00 Detection chamber pressure now less than 2×10^{-7} torr. Proceed with preliminary checks and calibration. Start detector and chopper equipment. Allow it to stabilize at desired values to be used for the experiment. Connect desired gas bottle to the nozzle supply line. Raise source pressure to desired level and allow it to stabilize.
- 08.00 Begin experiment.

SHUT-DOWN PROCEDURE

- When it becomes necessary to reopen the system in order to make changes in the experimental parameters the following procedure is recommended.
- 00.00 Shut down all electronic accessories. Shut down high pressure gas supply bottle. Switch off ionization gage. Switch off all three diffusion pumps but leave cooling water on.
- 03.00 Switch off mechanical pump. Shut down cooling water supply. Open bleed valves.
- The system is now ready to be opened. The cover-plate is lifted on the two permanently mounted jacks and then rolled to one side on teflon rollers moving on wooden guide rails.